The University of Nottingham

UNITED KINGDOM · CHINA · MALAYSIA

Welch, Nathan (2015) Non-equilibrium dynamics of Bose-Einstein condensates. PhD thesis, University of Nottingham.

Non-Equilibrium Dynamics of Bose-Einstein Condensates

The University of Nottingham

Nathan Welch

Thesis submitted to the University of Nottingham for the degree of Doctor of Philosophy, January 2015.

Abstract

In the following work we investigate the dynamics of Bose-Einstein condensates (BECs) under the influence of time-dependent potentials. The response of such a sensitive system to external perturbations is a matter of increasing interest. This is because of the enormous growth in understanding the physics and emerging applications of BECs in many areas of physics such as sensing, microscopy and quantum information.

We start with a brief explanation of the thermodynamics behind the phenomenon of Bose-Einstein condensation and how condensation is achieved experimentally. After this we outline an efficient method of numerically simulating a harmonically trapped, zero temperature BEC with repulsive self-interactions.

In chapter 3 we describe the effects of applying resonant, travelling, optical lattices to a harmonically trapped BEC. We show that the resulting dynamics are well described by classical non-KAM chaos, which allows a great deal of control over the excitation of the BEC, even in the presence of inter-atomic collisions. Chapter 4 explores this regime of non-linear dynamics in a quantum picture and shows that this enables the controlled excitation of atoms into single quantum-mechanical modes of a harmonic trap. This technique is then broadened to allow atoms to be excited into arbitrary superpositions of states using a genetic algorithm with additional numerical optimisation. Next, we use this method to excite a groundstate, non-interacting gas into a series of different cat states. To the author's knowledge, this is the first example of a technique that allows the controlled generation of a varying cat states with large numbers of on-interacting atoms.

In the following chapter, we move on to describe the various mechanisms that allow atoms to leave a trap when placed close to a surface. This involves including the effects of three-body collisions and quantum tunnelling due to the strong Casimir-Polder attraction between surface dipoles and the

trapped atoms. We calculate the lifetimes for traps of various geometries above a range of surfaces and show that experimentally useful lifetimes can be achieved even at nanometre scale atom-surface separations.

Drawing on this knowledge, we analyse the results of a recent experiment in which a BEC is coupled to a resonantly driven cantilever via the Casimir-Polder interaction. Due to the resonant driving condition, we show that the anomalous effects observed in the experiments cannot be explained by a simple increase in the atom-surface interaction due to contamination of the surface. Instead, we show that uncertainties in the atom-surface separation must also play a role in the BEC dynamics.

We also investigate the possibility of coupling a condensate to a cantilever oscillating under thermal excitation. We show that for the configuration used in the previous experiments, the coupling is greatly limited due to atom losses. We propose an alternative experimental arrangement that allows a much smaller atom-surface separation and greatly increased coupling with minimal atom losses. We show that this arrangement could allow the cooling of the cantilever using a condensate.

After investigating zero temperature condensates, chapter 7 outlines various methods of describing a finite temperature gas of atoms that includes a condensate in the presence of a thermal cloud. Using three different models of equilibrium clouds, we show that, by including all the collisions between the thermal cloud and the condensate, novel behaviour emerges. This appears primarily as a sizeable shift of not only the critical temperature but also the chemical potential required for the onset of Bose-Einstein condensation. We derive an approximate analytical description of the system at the onset of condensation.

Finally, we study a recent experiment in which condensates are created in a cross-over 1D-3D geometry over a range of temperatures. The lack of an analytical description requires the use of a finite temperature numerical model, which is used to accurately recreate the various experimentally measured density distributions. Lastly, we investigate the Landau damping of a centre of mass excitation in the condensate that is greatly affected by the geometry of the system. We find good agreement between the results found experimentally and via our simulations.

Publications

The following is a list of publications currently being written based on or including the content of this thesis:

The Effects of Stochastic Webs on the Dynamics of BECs in a Moving Optical Lattice
N. Welch, M. Greenaway and T.M. Fromhold.

Controllable State Excitation via an Optical Lattice
N. Welch, M. Greenaway and T.M. Fromhold.

Graphene-based atom chips for trapping and controlling ultracold atoms
C. Koller, T.M. Fromhold, P. Kruger, F. Intravaia and N. Welch.

Graphene-based atom chips for trapping and controlling ultracold atoms
C. Koller, T.M. Fromhold, P. Kruger, F. Intravaia and N. Welch.

Accurate Calculation of the The Thermodynamic Quantities of a BEC
B. Yuen, N. Welch, E. Hinds and T.M. Fromhold.

The Effects of Large Interactions in a Finite Temperature Bosonic Gas
R. Howl, N. Welch, N. Cooper, S. Piano, A. Paris-Mandoki, J. Nute, J. Wu, T.M. Fromhold and L. Hackermueller.

The following patent is also in preparation:

Graphene-based chips for trapping and controlling ultracold atoms
T.M. Fromhold, A. Gadge, F. Intravaia, B. Kaczmarek, C. Koller, P. Krüger and N. Welch

Acknowledgements

Many people have aided me in completing the last four years. Notably, the ever changing inhabitants of C19, whose knowledge is only surpassed by their helpfulness. Secondly, my supervisor, Mark Fromhold, to whom I shall be forever grateful for the amount he has taught me and the number of opportunities he has placed in front of me. Many thanks also go to the numerous people I have met and talked with over the last four years. Whether at Nottingham, St. Andrews, Newcastle (especially Nick Proukakis, Stuart Cockburn and Michael Garrett), Birmingham, London (Ben Yuen and Ed Hinds) or even halfway up a mountain in Les Houches, the amount you can learn when you're surrounded by such intelligent people is staggering.

Finally, I must thank my friends, family and primarily Tamsin. It's impossible, even for a pessimist like me, to not feel positive when someone shows you such unerring belief.

Contents

Chapter 1

Introduction to Bose-Einstein Condensates

1.1 Bose Einstein Condensation

With the birth of quantum mechanics came the realisation that all known particles could be classified as bosons or fermions. Fermions, named after Enrico Fermi, were shown to obey the Pauli exclusion principle, in which no two particles can exist in the same quantum state. This leads to (or is caused by, depending on your philosophical position) each atom being theoretically distinguishable from any other atom [1–3]. Conversely, bosons, named after Satyendra Nath Bose, have no such restriction. Therefore any number of atoms can occupy the same quantum state. Consequently, they act entirely identically to each other and are therefore indistinguishable [4].

Whether particles are indistinguishable or not plays a large role in their statistical distribution, primarily in terms of how energy is distributed amongst a thermal bath of each type of particle, namely whether atoms follow Fermi-Dirac statistics or Bose-Einstein statistics.

In 1924, Satyendra Nath Bose and Albert Einstein showed that when lowering the temperature of a fixed number of bosonic atoms, the ground-state of the system would become occupied by an increasing number of these indistinguishable particles. This set of atoms, referred to as a Bose-Einstein condensate (BEC), would then be described by a single wavefunction and allow quantum-mechanical effects to be observed on a macroscopic scale [5]. The reason for this condensation can be shown relatively simply from the

Bose-Einstein distribution:

$$f(\epsilon) = \frac{1}{e^{\frac{\epsilon - \mu}{k_B T}} - 1}, \qquad (1.1)$$

where $f(\epsilon)$ is the probability of finding a particle of energy ϵ in a distribution of atoms at temperature T and k_B is Boltzmann's constant. The chemical potential, μ, is required to give a conserved number of particles, and thus equals zero for systems of photons or phonons, which can be created and destroyed, but is typically negative when describing any classical set of atoms. If we take the density of states, or the number of possible ways an atom can have a given energy ϵ, to be equal to 1, then the total number of atoms is simply the integral of $f(\epsilon)$ over all energies, 0 to infinity.

However, it can be shown that in order to produce a sizeable number of atoms at very low temperatures, the chemical potential must be positive. Therefore, from equation (1.1), the probability of finding an atom with an energy in the range 0 to μ is negative, a physical impossibility. The reason for this is the lack of an energetic groundstate in the derivation of the Bose-Einstein distribution [4], which we call the BEC. Therefore the condensate is only one state in a thermal distribution, which will become increasingly populated with decreasing temperature. However, only at $T = 0$ will a collection of bosons ever be a pure condensate. Experimentally, though, a cloud of atoms is deemed a BEC when the majority of atoms are in the condensate mode and the remaining thermally-distributed atoms play little part in the evolution or dynamics of the condensate.

It was over 70 years after this theoretical prediction before a BEC was observed in a gas of rubidium atoms by the group of Cornell and Wieman in Colorado [6], followed shortly by the creation of a sodium BEC at MIT [7].

1.2   Experimental Realisation

The difficulty in the experimental realisation of a Bose-Einstein condensate is the requirement to produce a cloud of atoms at a temperature low enough (typically billionths of a degree above absolute zero) in numbers high enough that the chemical potential undergoes an inversion from negative to positive. The difficulty lies in holding and cooling atoms in a manner which largely uncouples them from the room-temperature, classical world in which they are created, this rules out standard cooling techniques such as refrigeration.

1.2.1 Atom Trapping

Simply put, atoms are "trapped" when they are confined by a spatially varying potential minimum, whose depth is much greater than the energy of each atom. For the purposes of BEC creation, this is carried out in one of two ways.

Firstly, atoms can be trapped using a magnetic field, B, which alters the internal energetic levels of an atom:

$$E_{m_F} = g_F m_F \mu_B B, \tag{1.2}$$

where g_F is the Landé g-factor, μ_B is the Bohr magneton and m_F is the sub-level of the quantum state F [8, 9]. If the sub-level, m_F is positive the atom is repelled by strong magnetic fields and is deemed "low-field seeking", therefore the atom will be attracted to magnetic field minima (high-field seeking atoms cannot be trapped as Maxwell's laws do not allow magnetic field maxima). However, an atom moving in these spatially varying magnetic fields will see an effective time-dependent magnetic field, which can induce level transitions in the atoms (i.e. m_F becomes 0 or negative) and so the atom will no longer be trapped. This effect is minimised when B is large and so spatially varying magnetic fields with zero minima are often complemented with spatially constant magnetic fields to stop these losses (see previous references).

The second method for trapping atoms is by using laser fields to create "optical" traps. These use the electric field of the laser light to create a dipole moment in the atoms, the energy of which goes as [10]:

$$E_{dip} \sim -\frac{I(\mathbf{r})}{\delta}, \tag{1.3}$$

where I is the spatially varying intensity of the laser field and δ is the detuning from a given internal atomic energy level. Therefore the magnitude of the optical field and the size of the detuning both control the size of potential created by the laser. Additionally, the detuning can be positive (red detuned) and the atoms will be drawn to areas of high laser intensity or negative (blue detuned) and the atoms are drawn to low intensity areas. Optical potentials have many uses as they can be created in almost arbitrary shapes [11], as well used to create time varying potentials which will be exploited later in this thesis.

1.2.2 Cooling to Condensation Temperatures

Lasers are sources of highly coherent photons, first predicted by Einstein in 1917 [12]. However, it wasn't until 1975 that their use as a device for atomic cooling was proposed [13]. The first stage of cooling is called the *Zeeman slower*, which involves aiming a laser beam at the initial cloud of hot atoms, resonant with an internal state of the atom in order to drive them into an excited state.

This cools the atoms due to radiation pressure decreasing their momentum, and therefore kinetic energy, in one dimension. During the absorption of the photon, the atoms must decelerate in order to conserve the total momentum of the system. Of course, the atoms will relax from this excited state by emitting a photon. However, this emission is carried out in random directions and therefore, after numerous absorption and emission processes, the momentum change due to emission will average out to zero. Consequently, if an atom is travelling towards a photon source it will be slowed by however many photons it absorbs and remits. A total of 6 laser beams (2 counter-propagating beams in all 3 cartesian directions) is required in order to cool the cloud of atoms.

As the atoms are travelling at different speeds they experience a different wavelength of light from each beam, which causes the previously resonant beam to become detuned from the internal excitation. In order to cancel out this effect, carefully created inhomogeneous magnetic fields are applied to the atom clouds. The Zeeman effect, which is caused by the magnetic fields shifting the energies of the internal states of an atom, then cancels out the Doppler shift and allows the resonant absorption and emission process to occur. Therefore, due to the Doppler effect, the absorbtion of a Doppler shifted photon and emission of a larger wavelength photon causes the atom to undergo a cooling process as opposed to just an energy conserving change of momentum.

The limit of this cooling is a single photon recoil, which allows the atoms to be cooled to just a few micro-Kelvin. Note that these two stages only involve atom-photon interactions, which allows the atoms to be uncoupled from an incohernet classical environment and interact with only the highly controlled coherent laser. So far, atom-atom interactions have not been required and so the atoms can be cooled even in relatively low densities. This is crucial as it allows the atoms to cool and remain in a gaseous state without becoming liquids or solids that would not allow efficient cooling and would

freeze atoms into non-condensed states.

However, once the laser cooling has reached the single photon momentum limit, interatomic collisions are then required in order to reach nano-Kelvin condensation temperatures. The Bose-Einstein distribution given in equation (1.1) requires that the atoms are in thermal equilibrium. The easiest method to reach this is to allow the atoms to collide and share energy with one another. Evaporative cooling makes use of this by lowering the trapping potential (by either decreasing the power of trapping beams in the case of an optical trap, or applying an RF field to cause anti-trapping in a magnetic field [6]) so that high energy atoms can be ejected from the trap. This causes the high energy "tail" of the Bose-Einstein distribution to be lost and the atoms then collide with one another and re-equilibrate into a gas of lower temperature. If the atoms are in a smoothly varying trap such as a harmonic potential, the density of the cloud will increase as it becomes colder because fewer atoms have the energies required to travel up the sides of the potential. This is useful as the higher density increases the rate of atomic collisions and so enhances the speed at which the atoms reach equilibrium. In a finite trap this will increase the speed at which the thermal tail of the distribution is repopulated and so high energy atoms will be lost at an increasing rate. This so called "runaway" cooling allows the atoms to finally reach the nano-Kelvin temperatures required for the onset of Bose-Einstein condensation.

Chapter 2

Numerical Methods

2.1 Coherent and Incoherent Regions of a Finite Temperature Gas

In order to make our treatment of a finite temperature BEC tractable we shall initially only consider largely occupied, coherent, states rather than a whole thermal distribution. This is because we are interested in investigating the driven dynamics that are caused by whichever stimulus (typically, a time-dependent potential) is currently being applied. This means that we can treat any higher energy, thermal parts of the trapped gas as a small perturbation that can be ignored on short timescales. If we were considering long timescales and thermalisation within a BEC this would not be sufficient [14,15].

Figure (2.1) is a representation of the three regions in a finite temperature BEC in a harmonic trap. The most heavily occupied states at the bottom of the trap (striped region) are described as the coherent region and comprise atoms with energies less than ϵ_{cut}, these can be accurately described by a macroscopically occupied mean-field wavefunction.

Exactly what is considered coherent and incoherent isn't dealt with explicitly in our formalism. The primary requirement is that no misleading results occur if we assume that atoms in what we have deemed the coherent region can be treated as well described by a single mean-field wavefunction. This requires them to be have large spatial and temporal coherence resulting in highly correlated behaviour (i.e. the evolution of any single atom must be similar to every other atom) with larger energy particles treated as excita-
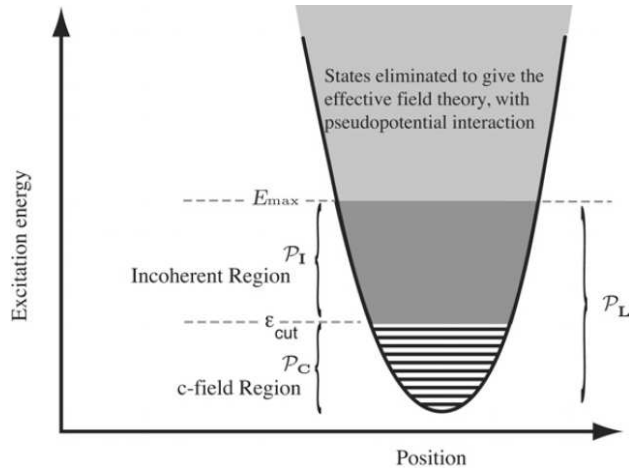
Figure 2.1: Energy-position schematic of a harmonically trapped, thermal gas of atoms, taken from [16]. The low energy, coherent region (striped) requires a mean-field semi-classical description. The higher energy, incoherent region (dark grey) strictly requires a quantum kinetic method, though we shall be treating atoms in this region as always close to equilibrium.

tions in an otherwise coherent field. Conversely, the incoherent region cannot be assumed to be well described by a single wavefunction as the highly excited particles show little correlation and must treated as individual particles. Whilst exactly what is deemed coherent and incoherent has no simple definition, it is an active area of continuing discussion, see e.g. [17,18].

Additionally, as we are treating the coherent field semi-classically, we can ignore 1/2 quantum fluctuations so long as:

$$N_c \gg \frac{M}{2}, \tag{2.1}$$

where N_c and M are the number of atoms and modes in the coherent region in the region, as described later. The effect of ignoring these fluctuations also manifests itself as a lack of (Bose-enhanced) spontaneous scattering events required to accurately model the thermalisation of a BEC, as un-occupied modes will remain empty [16].

In chapter 8 we shall introduce the incoherent region, shown in figure (2.1) as the dark grey area, which contains atoms with energies $\epsilon_{cut} < E_{atoms} < E_{max}$. These will include all the thermal scattering processes required allowing long-time thermalisation effects to be modelled [16]. Atoms with higher

energies (shown by the light grey area in figure (2.1)) will be entirely omitted as these will simultaneously require a much more complex treatment and have little effect on the system.

When including the incoherent regime we have a stricter requirement on the coherent region as the differentiation between a macroscopically occupied mode and a thermal mode become more important. In particular, we have to ensure that:

$$\langle N_{cut} \rangle > 1, \tag{2.2}$$

where $\langle N_{cut} \rangle$ is number of atoms in the highest coherent mode (averaged over all degenerate states and time). This will then allow the incoherent, thermal atoms to be well described by the Bose-Einstein distribution function, as explained in chapter 8.

2.2 The GPE

In order to include the complex dynamics of a real system of atoms a key component in the form of inter-atomic collisions has to be included. In the limit of small densities and low temperatures this can be carried out with the Gross-Pitaevskii equation (GPE) [19, 20]:

$$i\hbar \frac{\partial \psi}{\partial t} = \left[-\frac{\hbar^2}{2m} \nabla^2 + \frac{m}{2} \boldsymbol{\omega}^2 . \mathbf{x}^2 + g|\psi|^2 \right] \psi, \tag{2.3}$$

where $\psi = f(\mathbf{x}, t)$ is a time varying, 3D mean field wavefunction for atoms of mass m in a harmonic trap described by:

$$\frac{m}{2} \boldsymbol{\omega}^2 . \mathbf{x}^2 = \frac{m}{2} \left(\omega_x^2 x^2 + \omega_y^2 y^2 + \omega_z^2 z^2 \right), \tag{2.4}$$

where $\omega_{x,y,z}$ are the trapping frequencies in the x, y and z directions, respectively. Whilst we have assumed a 3D harmonic trap in the above equation, this is not a requirement of the GPE. In principle the trapping potential could be of any form so long as the resulting mean-field wavefunction could still show long range coherence (i.e. there are no large potential barriers that cause the wavefunction to effectively fragment into multiple independent regions). Therefore, more experimentally realistic potentials could be used, i.e. inverted Gaussian shape traps for attractive optical potentials or typical anharmonicities due to the finite wire sizes of magnetic traps etc.

The third term on the RHS of equation (2.3) includes the effect of the inter-atomic collisions via the local density, $|\psi|^2$, multiplied by an interaction co-efficient given by:

$$g = \frac{4\pi a_s \hbar^2}{m},\qquad(2.5)$$

where a_s is the s-wave scattering length of the atoms and $\hbar$ is the reduced Planck's constant.

This additional perturbation is valid if both the density is low enough and collisions are low energy enough that only the simplest elastic collisions take place between atoms. This is because the low energy atoms only have relatively large wavelengths on the scale of the inter-particle separations, which "coarse-grains" the spatial interaction between the atoms resulting in them experiencing each other as single hard spheres with an approximate radius of a_s and so only undergo s-wave scattering. This means any finer spatial variation of the interacting particles, such as the repulsion of higher energy electron orbitals, can effectively be emitted. Consequently, we can to ignore any change in angular momentum due to collisions or momentary bound states that can be created by collisional interactions [21].

The GPE equation can be numerically evolved using a variety of means and has shown remarkable accuracy as well as predictive powers (for example [22]) that have allowed experimental results to be explained and new experimental regimes promoted. However, in this thesis we shall add in an explicit limit to this equation to ensure it only describes the low energy regime in which it is known to be valid.

2.3   The PGPE

In order to limit our treatment of the BEC to the coherent region, we shall include a projection operator in the GPE given above in order to produce the projected Gross-Pitaevskii equation (or PGPE), which will limit the mean-field wavefunction to only including atoms of energy $< \epsilon_{cut}$, that satisfy the equation:

$$i\hbar\frac{\partial \psi}{\partial t} = \mathcal{P}\left[-\frac{\hbar^2}{2m}\nabla^2 + \frac{m}{2}\boldsymbol{\omega}^2.\mathbf{x}^2 + g|\psi|^2\right]\psi.\qquad(2.6)$$

The projector, $\mathcal{P}$, will be explicitly included by expanding the mean field

wavefunction into energy states of the harmonic trap and truncating the number of states used:

$$\psi(\mathbf{x}, t) = \sum_{\alpha,\beta,\gamma=0}^{\alpha_{cut}\beta_{cut}\gamma_{cut}} C_{\alpha,\beta,\gamma}(t)\phi_\alpha(x)\phi_\beta(y)\phi_\gamma(z) \qquad (2.7)$$

where α, β and γ are state numbers in x, y and z respectively, $C_{\alpha,\beta,\gamma}(t)$ is the time varying complex amplitude of the state $n = \{\alpha, \beta, \gamma\}$ and $\phi_n(\mathbf{x}) = \phi_\alpha(x)\phi_\beta(y)\phi_\gamma(z)$ is the quantum harmonic oscillator (QHO) basis state given in each direction by:

$$\phi_\alpha(x) = h_\alpha H_\alpha(x/l_x)e^{-\frac{x^2}{2l_x^2}}, \qquad (2.8)$$

where $H_\alpha(x/l_x)$ is the αth order (physicist's) Hermite polynomial and $l_x = \sqrt{\hbar/m\omega_x}$ is the natural harmonic oscillator length. The term $h_\alpha = 1/\sqrt{2^\alpha \alpha!\sqrt{\pi}}$ is a normalisation constant that ensures the state satisfies the orthonormality completeness relation:

$$\int_{-\infty}^{\infty} \phi_n(\mathbf{x})\phi_m(\mathbf{x})d\mathbf{x} = \delta_{n,m}. \qquad (2.9)$$

The QHO state is the eigenvector of the non-interacting Schrödinger equation for a harmonically trapped particle:

$$-\frac{\hbar^2}{2m}\nabla^2\phi_n(\mathbf{x}) + \frac{m}{2}\boldsymbol{\omega}^2.\mathbf{x}^2\phi_n(\mathbf{x}) = E_n\phi_n(\mathbf{x}), \qquad (2.10)$$

where the energy of the nth state is:

$$E_n = (\alpha + 1/2)\hbar\omega_x + (\beta + 1/2)\hbar\omega_y + (\gamma + 1/2)\hbar\omega_z. \qquad (2.11)$$

Then by setting ϵ_{cut}, the states that satisfy $E_n \leq \epsilon_{cut}$ can be included in the expansion. This means that the maximum allowed modes in the three directions, α_{cut}, β_{cut} and γ_{cut} will be functions of ϵ_{cut} and each other.

Though this limit isn't entirely accurate, as the effect of the inter-atomic collisions will act to increase the energy of each mode (as they are no longer energy eigenstates of the system). If, however, the densities are low enough such that the energy of the interactions per particle is small in comparison to ϵ_{cut}, then this will be accurate enough to ensure that no higher energy dynamics are being included [16].

Choosing ϵ_{cut}

There has been much discussion on what values should be used in these 'coherent field' methods [23]. However, there appears no single definition of what this should be as a great range of values have previously been used and shown to agree well with experiment [16]. In general, the larger the cut-off energy, the higher the energy of the dynamics that can be simulated. However, the previous reference shows that the theory breaks down for very large energy cut-offs due to the coherence requirement stated earlier.

In this thesis we shall use two different techniques. In chapters 3-6 we are only interested in fast, non-equilibrium dynamics that are studied over relatively short timescales, which allows for little equilibration. In this case we shall use as many modes is as required so that $E_{tot} < \epsilon_{cut}$ and $N_{cut} \sim 0$, which effectively turns the PGPE into the GPE.

For the second part (chapter 8), which involves studying long time averages and equilibration dynamics, we shall instead adhere to equations (2.1) and (2.2). Therefore we will use the generally accepted value $\epsilon_{cut} = 3\mu$ where μ is the chemical potential of the system as explained later [24]. This allows the system enough modes to exhibit the complex equilibration dynamics we wish to study without spurious results due to the validity of the mean-field wavefunction approximation being violated.

2.3.1 Numerical Implementation and Oscillator Units

The PGPE is greatly complicated by the inclusion of the density dependant potential term (the GPE and PGPE are often referred to as non-linear Schrödinger equations, NLSE). However there is a relatively simple method to include the interactions in a computationally efficient manner.

Firstly we shall introduce the dimensionless PGPE by dividing the SI PGPE by one of the energy level spacing of the system, in this case $\hbar\omega_x$, then by introducing the dimensionless time $\tilde{t} = t\omega_x$ and length $\tilde{x} = x/l_x$ units we create:

$$i\frac{\partial \psi}{\partial \tilde{t}} = \mathcal{P}\left[-\frac{1}{2}\tilde{\nabla}^2 + \frac{1}{2}\tilde{\boldsymbol{\omega}}^2.\tilde{\mathbf{x}}^2 + \frac{g}{\hbar\omega_x}|\psi|^2\right]\psi, \qquad (2.12)$$

where:

$$\frac{1}{2}\tilde{\boldsymbol{\omega}}^2.\tilde{\mathbf{x}}^2 = \frac{1}{2}\left(\tilde{x}^2 + \frac{\omega_y^2}{\omega_x^2}\tilde{y}^2 + \frac{\omega_z^2}{\omega_x^2}\tilde{z}^2\right) \qquad (2.13)$$

and $\tilde{y} = y/l_y$, $l_y = \sqrt{\hbar/m\omega_y}$ and similarly for z, $\tilde{z}$ and l_z.
We can then simplify things further using the dimensionless wavefunction:

$$\tilde{\psi} = \sqrt{l_x l_y l_z}\psi \tag{2.14}$$

and interaction constant:

$$\tilde{g} = 4\pi a_s \frac{l_x}{l_y l_z} \tag{2.15}$$

to produce:

$$i\frac{d\tilde{\psi}}{d\tilde{t}} = \mathcal{P}\left[-\frac{1}{2}\tilde{\nabla}^2 + \frac{1}{2}\tilde{\boldsymbol{\omega}}^2.\tilde{\mathbf{x}}^2 + \tilde{g}|\tilde{\psi}|^2\right]\tilde{\psi}. \tag{2.16}$$

We can then create an 'equation of motion' for the expansion co-efficients by multiplying by $-i\phi_n(\mathbf{x})$ and integrating:

$$\frac{dC_n}{dt} = -i\left[\tilde{E}_n C_n + \tilde{g}M_n\right], \tag{2.17}$$

where $\tilde{E}_n = E_n/\hbar\omega_x$ and we have omitted the projector as this is included in the limit on n. The collisional interaction is then found via the integral:

$$M_n = \sum_{n'} C'_n \int_{-\infty}^{\infty} \phi_n(\mathbf{x})\phi'_n(\mathbf{x}) \sum_{n''} C_{n''}\phi_{n''}(\mathbf{x}) \sum_{n''} C^*_{n''}\phi_{n''}(\mathbf{x})d\mathbf{x} \tag{2.18}$$

To evaluate this integral we use a Gauss-Hermite quadrature method, a detailed description of which is given in appendix A.

Additional Perturbations

Many times in the later discussions we will apply additional perturbations to the trapped atoms which will typically be separable spatio-temporal potentials that have the form $U_{pert} = f(t)g(x)$. The effects of these potentials can be added into the PGPE with the addition of another matrix element S_n:

$$\frac{dC_n}{dt} = -i\left[E_n C_n + \tilde{g}M_n + f(t)S_n\right] \tag{2.19}$$

where:

$$S_n = \sum_{n'} C_{n'} \int_{-\infty}^{\infty} \phi_{n'}(x)\phi_n(x)g(x)dx. \tag{2.20}$$

Again, this integral can be evaluated very efficiently using the GHQ method given in appendix A.

2.3.2 Calculation of Observables

In order to efficiently evolve the wavefunction and calculate the necessary observables, we primarily wish to stay in the same basis throughout. This means not swapping back to the spatial wavefunction in order to calculate an observable such as the average position in some direction. Fortunately for most observables, there is some method of carrying out a single, time-independent, integration on the QHO modes that allows the observable to be fully calculated using a single set of matrix multiplications.

Chemical Potential

The chemical potential is the simplest and most numerically efficient value to calculate as, for the interacting system:

$$i\hbar\frac{d\psi}{dt} = \mu\psi. \tag{2.21}$$

In the dimensionless QHO basis this can be found using:

$$\mu = \frac{i}{N}\sum_n C_n^* \frac{dC_n}{dt} \tag{2.22}$$

where N is the total number of atoms.

Energy

The total energy of the atoms can be broken down into the energy due to momentum and the harmonic trapping potential (i.e. the energy associated with the QHO basis):

$$E_{HO} = \sum_n |C_n|^2 E_n, \tag{2.23}$$

and secondly the energy associated with the inter-atomic collisions:

$$E_{int} = \frac{\tilde{g}}{2}\sum_n C_n^* M_n \tag{2.24}$$

where the factor of $1/2$ is included to stop 'double counting'. Then, finally, the energy due to any other perturbations:

$$E_s = f(t) \sum_n C_n^* S_n. \tag{2.25}$$

The total energy is then, simply:

$$E_{tot} = E_{HO} + E_{int} + E_s. \tag{2.26}$$

Alternatively, using equations (2.19) and (2.22):

$$E_{tot} = N\mu - E_{int}. \tag{2.27}$$

Position

The average position of the cloud is a useful parameter to know when investigating the dynamics of a highly excited condensate, this can be found in any dimension using the weighted average formula:

$$\langle x \rangle = \frac{1}{N} \int_{-\infty}^{\infty} x |\psi(\mathbf{x},t)|^2 d\mathbf{x}$$

$$= \sum_{\alpha\alpha'} \int_{-\infty}^{\infty} x \phi_\alpha(x) \phi_{\alpha'} dx \sum_{\beta\beta'\gamma\gamma'} C_{\alpha\beta\gamma} C_{\alpha'\beta'\gamma'}^* \tag{2.28}$$

The integral above can be calculated using the GHQ techniques given earlier.

Momentum

We can use a Fourier transform to find the momentum distribution of the atoms, as follows:

$$n(\mathbf{p},t) = \frac{1}{(2\pi)^{3/2}} \int_{-\infty}^{\infty} e^{-i\mathbf{p}.\mathbf{x}/\hbar} |\psi(\mathbf{x},t)|^2 d\mathbf{x}$$

$$= \frac{1}{(2\pi)^{3/2}} \sum_{nn'} C_n^* C_n' \int_{-\infty}^{\infty} \phi_n(\mathbf{x}) \phi_{n'}(\mathbf{x}) e^{-i\mathbf{p}.\mathbf{x}/\hbar} d\mathbf{x}$$

$$= \frac{1}{(2\pi)^{3/2}} \sum_{\alpha\alpha'\beta\beta'\gamma\gamma'} C_{\alpha\beta\gamma} C_{\alpha'\beta'\gamma'}^* T_{\alpha\alpha'} T_{\beta\beta'} T_{\gamma\gamma'}, \tag{2.29}$$

14

where

$$T_{\alpha\alpha'} = \int_{-\infty}^{\infty} \phi_\alpha(x)\phi_{\alpha'}(x)e^{-ip_x x/\hbar}dx. \tag{2.30}$$

Alternatively, we can integrate over any two dimensions to produce the momentum distribution in the remaining dimension:

$$\begin{aligned}
n(p_x, t) &= \frac{1}{\sqrt{2\pi}} \int_{-\infty}^{\infty} e^{-ip_x x/\hbar} |\psi(\mathbf{x}, t)|^2 d\mathbf{x} \\
&= \frac{1}{\sqrt{2\pi}} \sum_{\alpha\alpha'\beta\beta'\gamma\gamma'} C_{\alpha\beta\gamma} C^*_{\alpha'\beta'\gamma'} T_{\alpha\alpha'}.
\end{aligned} \tag{2.31}$$

In the case of these integrals we cannot use the GHQ method as the exponential in the integral can only be considered to be a polynomial of order p in the limit that p goes to infinity. Instead, however, there are many numerical routines than can efficiently carry out the Fourier transform of the basis pair $\phi_\alpha(x)\phi'_\alpha(x)$.

Chapter 3

BECs in Travelling Optical Lattices

3.1 Introduction

Optical potentials created by the absorption and emission of photons from highly correlated laser fields have been used to carry out much work with cold atomic clouds. The ability to create stable, stationary potentials on experimentally useful length and time scales, has allowed phenomena such as atom transport [25–28] and Bloch oscillation [22, 29–33] to be thoroughly investigated. Similarly, the effects of strong inter-atomic interaction and deep lattices has been useful for the study of quantum information processes [34, 35].

However, comparatively little investigation has been carried out using dynamic optical potentials to study the evolution of atomic motion when the total energy of the atoms is no longer conserved [37, 38]. Though the work of Renzoni incorporates time-dependent optical lattices, these are typically employed to allow controllable transport of atoms through a lattice via a "quantum ratchet" [39–41] without driving excitation within the atoms themselves.

In this chapter, we will show that complex dynamics can be excited in cold, harmonically trapped atoms driven by a travelling optical lattice. Rich dynamics have been shown to exist for similar systems such as electrons in semiconductor superlattices driven by electric fields [42] and atoms driven to extreme temperatures in nuclear reactors [43].

The first part of the chapter uses established theories from classical chaotic motion to precisely describe and control the excitations caused by the moving lattice, with and without the presence of inter-atomic interactions. In the second half, we will show that specific optical lattices can be used, which cause a departure from classical mechanics and instead excite atoms to specific, quantised levels in a harmonic trap. This technique will then be expanded to excite atoms into prescribed superpositions such as cat states, opening up a large plethora of possible investigations which require precise state initialisation and manipulation [44–46].

3.2 Description of the System

In this chapter, we shall be studying the effects of a travelling optical lattice (OL) on a harmonically trapped cloud of ^{87}Rb atoms. In general, this can be described by the non-linear Schrödinger equation:

$$i\hbar\frac{d\psi}{dt} = \left[-\frac{\hbar^2\nabla^2}{2m} + \frac{m\boldsymbol{\omega}^2.\mathbf{x}^2}{2} + g|\psi|^2 + U_o\sin\left(k_l x - R\omega_x t\right)\right]\psi, \qquad (3.1)$$

where $\psi = f(\mathbf{x}, t)$ is a 3D time dependent wavefunction. Equation (3.1) is the $T = 0$ Gross-Pitaveskii equation described earlier with the addition of a spatio-temporal driving potential due to an OL of wavevector k_l and frequency $\omega_l = R\omega_x$, where R is a real, positive constant. This produces a travelling wave in the x direction with velocity ω_l/k_l.

Typically, optical lattices are produced by two phase-shifted counter-propagating laser beams (as described in many of the references above). Therefore, the potential will usually have a Gaussian profile in y and z which we have omitted as we are assuming that the width of the laser is much larger than the trapping length scale $l_{y,z} = \sqrt{\hbar/m\omega_{y,z}}$ and so is approximately constant across the width of the cloud in these directions. Secondly, any misalignment of the OL with the trap will, to first order, decrease the magnitude of the potential in the direction we wish to excite motion whilst also causing driving in the non-resonant perpendicular directions. However, as we shall show, the depth of the lattice is relatively un-important for the chaotic phenomena we wish to investigate and non-resonant driving causes very little excitation and so can effectively be ignored.
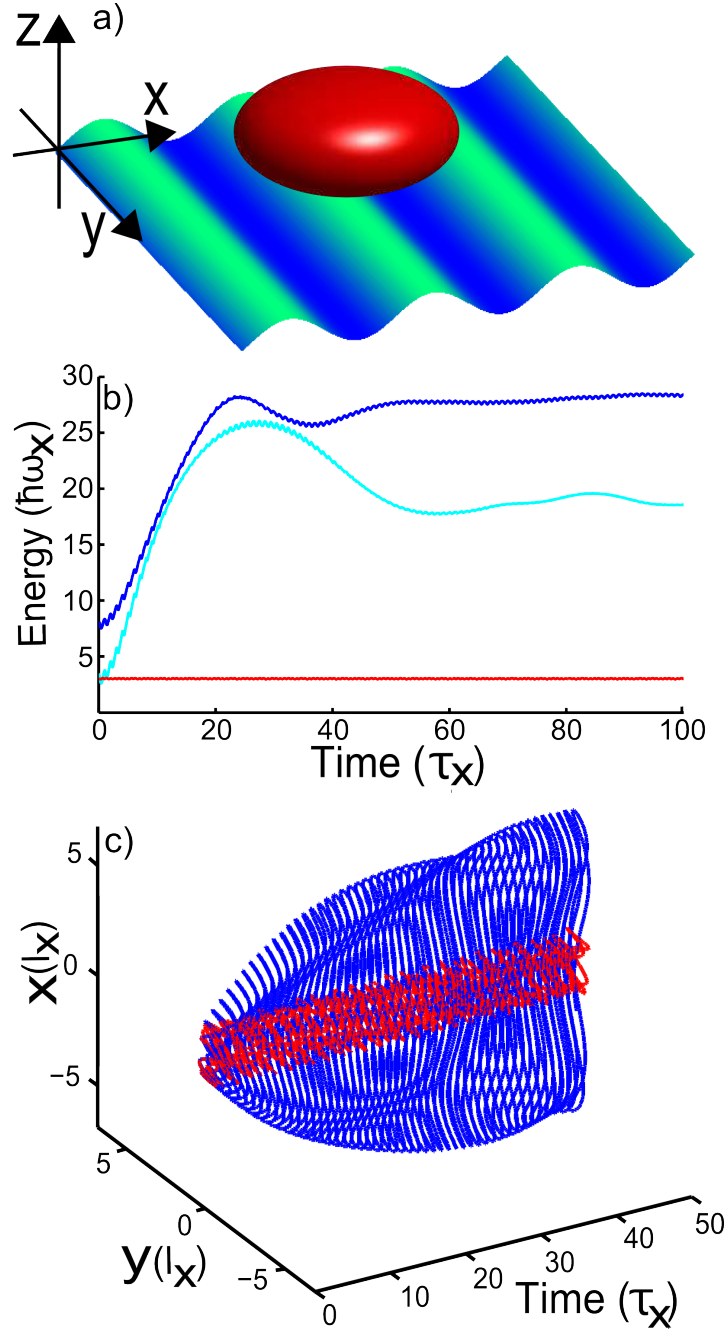
Figure 3.1: a) Iso-density surface (red) of groundstate BEC with a travelling wave potential, shown schematically, applied along the loosely trapped x direction, b) average atomic energies in units of the trap elevel spacing $\hbar\omega_x$, under the effects of a resonant, $R = 1$ OL for an interacting (dark blue) and non-interacting (light blue) cloud, also a non-interacting, non-resonant, $R = \sqrt{2}$, (red) OL against time, in units of the trap period, $\tau_x = 2\pi\omega_x$ and c) 2D projection of the centre of mass motion for non-interacting, resonant (blue) and non-resonant (red) OL in units of the harmonic oscillator length, $l_x = \sqrt{\hbar/m\omega_x}$. For all plots $U_o = 0.5\hbar\omega_x$ and $k_c = 0.5/l_x$.

Figure (3.1a) shows a schematic of the system, the red mass shows an iso-density plot (defined by 90% of the peak density) of a repulsive BEC in a harmonic trap of $\omega_{x,y,z} = 2\pi[30, 30, 120]$ Hz with the presence of the optical lattice shown by the sinusoidal travelling wave.

Evolving equation (3.1) we see the effect of the OL in figure (3.1b), which shows the average atomic energies of an interacting (dark blue) and non-interacting (light blue) cloud as it is driven by a resonant, $R = 1$ OL. In both cases the cloud is greatly excited to energies $\sim 25\hbar\omega_x$, with the atomic repulsion causing the interacting cloud to have consistently higher energies, the reason for this pronounced maximum will be explained in detail shortly. Interestingly there is a slight relaxation in both cases after the initial increase, this drop in energy is more pronounced in the non-interacting case, again this will be explained in detail later. For comparison, the average energy in the case of a non-interacting cloud driven by a non-resonant, $R = \sqrt{2}$ OL is included (red line) which shows no great excitation, only a modulation of $\sim U_o$. All were carried out with the same OL wavevectors $k_l = 0.5/l_x$ and amplitudes $U_o = 0.5\hbar\omega_x$. All of the parameters used in this example can be accurately simulated with the PGPE described earlier in chapter 2 and are also experimentally viable [16].

Figure (3.1c) shows the centre of mass in the x and y planes for the same resonant (blue) and non-resonant (red) OLs for the non-interacting system. In the resonant case the cloud can be seen to be oscillating with ever increasing amplitude in x, explaining the dramatic increase in energy. To show the scale of this excitation the cloud is initially placed off centre in the y direction by an amount $l_x/2$, resulting in simple oscillation as expected from a non-driven harmonic oscillator.

3.2.1   Dynamics and Non-KAM Chaos

It has been shown previously that for a non-interacting cloud ($g = 0$) the system given above can be analogously described by the classical dimensionless Hamiltonian [47, 48]:

$$H = \frac{\dot{x}^2 + x^2}{2} + U_o \sin\left(k_l x - Rt\right), \tag{3.2}$$

where we have used the harmonic oscillator units given earlier to create a dimensionless Hamiltonian. In the limit of $g = 0$ the transverse directions (y

19

and z) evolve exactly as harmonic oscillators with no coupling between any direction and, as such, their evolutions can be omitted from this discussion.

Additionally, although we are in principle considering a semi-classical mean-field system, we can consider the dynamics as classical as the relatively slowly varying optical lattice allows the particles to be treated as point like particles with no great errors. Secondly the small optical lattice depth ensures that atoms can typically, classically, travel over the potential barriers ensuring that the dynamics aren't greatly altered by quantum tunnelling.

The following mathematical treatment of equation (3.2) has been covered in detail previously for analogous systems so only the main points and useful results will be presented here. For a more rigorous treatment the reader is referred to [47, 49, 50]. Firstly we use a cylindrical co-ordinate transform to calculate a radius in dimensionless position-momentum phase-space:

$$\rho = x^2 + \dot{x}^2 \tag{3.3}$$

and a phase-space angle:

$$x = \rho \sin \theta. \tag{3.4}$$

Using these we can then create two 'action angles':

$$I = \frac{\rho}{2R} \tag{3.5}$$

and

$$\phi = R\theta - Rt, \tag{3.6}$$

which can allow us to separate the Hamiltonian into stationary and time dependant parts:

$$H = H_o + V(t), \tag{3.7}$$

where the stationary part is given by:

$$H_o = U_o J_R(k_l \rho) \cos(\phi) \tag{3.8}$$

and the time-dependent term is:

$$V(t) = U_o \sum_{m \neq R} J_m(k_l \rho) \cos \left[\frac{m}{R} \phi - \left(1 - \frac{m}{R} \right) Rt \right], \tag{3.9}$$

20

where $J_m(x)$ is the mth Bessel function of the first kind. Treating $V(t)$ as a small perturbation, it is possible to show that equation (3.2) exhibits stationary points given by:

$$\frac{\partial H_o}{\partial I} = 0 \text{ and } \frac{\partial H_o}{\partial \phi} = 0. \tag{3.10}$$

These stationary points give a set of stable, elliptic points:

$$J'_R(k_l \rho) = 0 \text{ and } \phi = 0, \pi \tag{3.11}$$

and a set of unstable, hyperbolic points:

$$J_R(k_l \rho) = 0 \text{ and } \phi = \pm\pi/2. \tag{3.12}$$

Figure (3.2) shows the positions of the stable islands at the elliptic points (blue) which are surrounded by the hyperbolic points (red) these are then connected by a series of separatrices (black), in the form of $2R$ radial filaments connected by a series of concentric ring filaments. These separatrices are infinitely thin in the limit of $V(t) = 0$ however as the perturbation is finite ($V(t) \sim U_o$, the depth of the OL) these filaments become wide enough to permit atoms to travel along them. This phase-space structure is known as a stochastic web and its presence allows the driven atoms to become delocalized in phase-space and so gain a great deal of energy.

Atoms with initially low energies (and so near the centre of phase-space, $x \sim \dot{x} \sim 0$) can travel along the thin black separatrices and outwards in phase-space greatly increasing their energies as:

$$E = \frac{x^2 + \dot{x}^2}{2} = \frac{\rho^2}{2} \tag{3.13}$$

It can be shown that the widths of these radial filaments are proportional to:

$$\Delta_{fil} \propto \sqrt{\rho}\, e^{-A\sqrt{\rho}}, \tag{3.14}$$

where A is a positive constant, which means that the likelihood of an atom travelling outwards becomes ever smaller with increasing delocalization. Whilst not a probabilistic mechanism *per se*, with greater excitation, the requirements on a particle's initial position in phase-space become exponentially stricter.
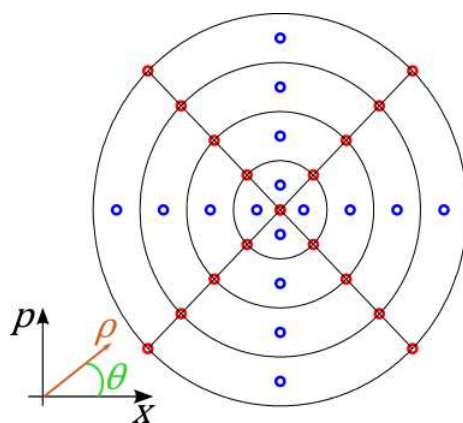
Figure 3.2: Phase-space schematic of the $R = 2$ stochastic web, created by stable islands centred on the elliptic fixed points (blue) surrounded by the hyperbolic points (red) which are connected by a series of separatrices (black) - bottom left, phase-space co-ordinate axes.

3.2.2 Non KAM Chaos and Classical Poincaré Sections

As the points that define the stochastic web, given by equations (3.11) and (3.12), depend on $\phi \sim \omega_x t$, they rotate in time with a period of $2\pi/\omega_x$. Therefore, in order to visualise the stochastic web, we must create a Poincaré section by imaging the evolution of the underlying orbits periodically.
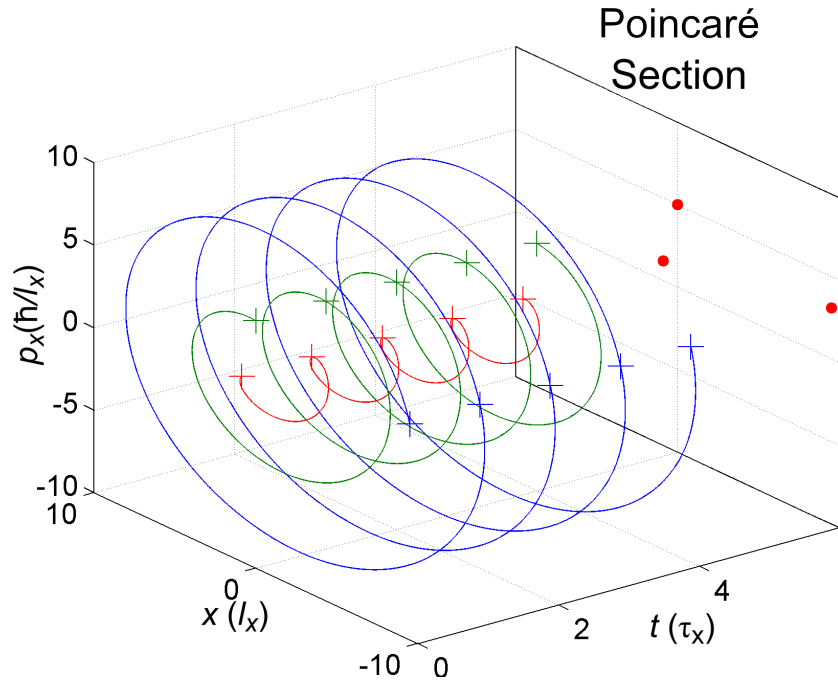
Figure 3.3: Phase space evolution of three atoms (coloured lines) with random initial conditions in a harmonic trap. Crosses show the phase-space positions at $t = [0, 1, 2, 3, 4]2\pi/\omega_x$, Poincaré section at the rear of the plot shows the phase-space projection of these points.

Figure 3.3 shows the phase-space, position-momentum, evolution of a set of classical particles evolved using equation (3.2) with $U_o = 0$ and varying initial conditions. The atoms are allowed to oscillate freely with a frequency that matches that of the harmonic trap. To the rear of the figure is the Poincaré section (red dots) which shows the periodically plotted ($t = [0, 1, 2, 3, ...]\tau_x$) positions and momenta of the atoms. As the OL is not present, the energy of each atom is conserved and, as such, so is the radius of their respective oscil-

lations. This ensures that at the same point in each period, the phase-space positions of the atoms remains the same (coloured crosses), which means that the Poincaré section only shows each atom as a single, stationary point in phase-space.

Figure 3.4 shows the evolution of three particles moving under the influence of an OL of depth, wavevector and frequency $[2\hbar\omega_x, 0.26/l_x, \omega_x]$. Plotted in time, the phase-space evolution of each atom is a complex set of Lissajous curves of time dependent amplitude [51] and the overall behaviour of the system is particularly complex. The Poincaré section at the rear of the plot shows the phase-space positions (red dots) of a set of 100 atoms with random initial conditions taken at the same points in time as above, but extended over 500 trap periods. This clearly shows the presence of the predicted $R = 1$ stochastic web, with the elliptic points, hyperbolic points and filaments shown in light blue.

This example shows the results of a relatively weakly driven system ($U_o \ll E_{ring}$) and, as such, the phase-space filaments can't be readily seen in the Poincaré section. Instead all the atoms appear to be travelling along stable orbits centred around the elliptic points. In the case of a much deeper lattice ($U_o = 8\hbar\omega_x$), as shown in figure 3.5, the filaments appear as a region of unconnected points, which create a 'chaotic sea' along the stochastic filaments. In the limit of infinite time, this sea allows atoms to travel from any point in the chaotic sea to any other point in the sea [47]. Due to the chaotic nature of this phase-space region, the evolution of any atom which begins in the chaotic sea will be extremely sensitive to its initial conditions, and will have a real, positive Lyapunov exponent λ given by:

$$\Delta\rho = Ae^{\lambda t}, \tag{3.15}$$

where $\Delta\rho = \sqrt{[x_a(t) - x_b(t)]^2 + [p_a(t) - p_b(t)]^2}$ is the phase-space separation of two particles, a and b with an arbitrarily small difference, A, in their initial conditions. This sensitivity to initial conditions is proof of chaotic evolution [51]. However, typical chaotic dynamics (referred to as Kolmogorov-Arnold-Moser or KAM chaos) appear slowly in a system usually via the period doubling of regular motion that eventually leads to chaotic behaviour. However in the case of the OL-driven system described above, the chaotic dynamics appear instantly in phase-space so long as the OL frequency some integer multiple of the harmonic trap frequency, this is known as non-KAM chaos. This type of system is interesting as it allows stable
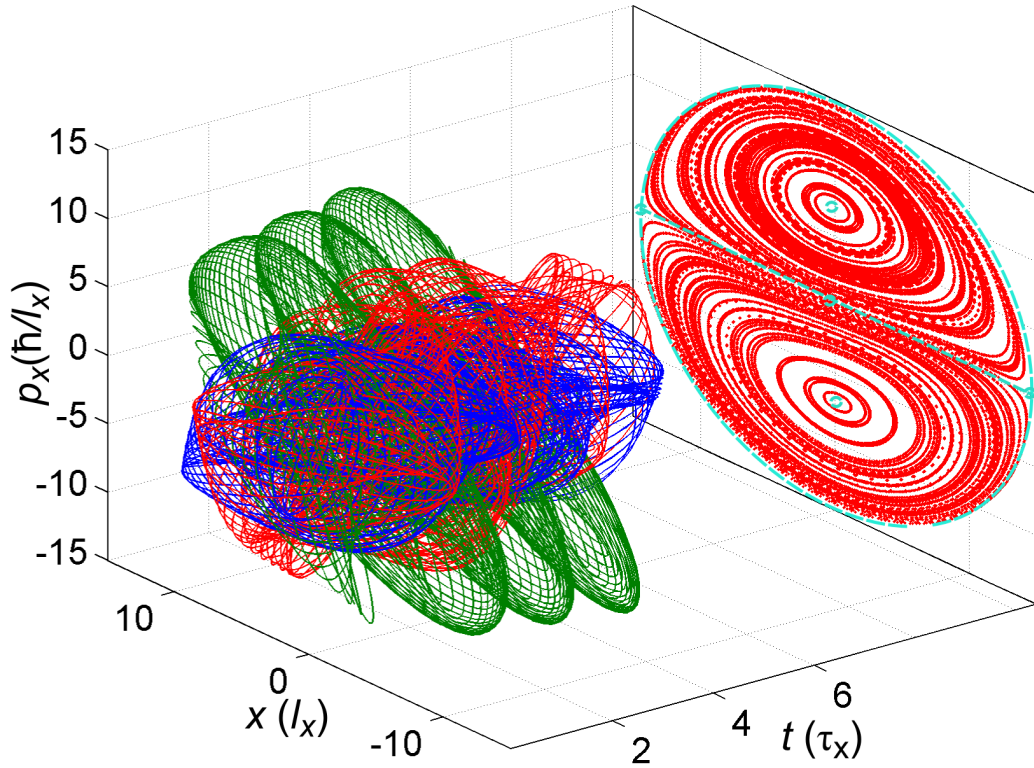
Figure 3.4: Phase space evolution of three atoms with random initial conditions in a harmonic trap (coloured lines), driven by an OL with $U_o = 2\hbar\omega_x, k_l = 0.26/l_x, \omega_l = \omega_x$, Poincaré section shows periodically-plotted phase-space points for 100 atoms evolved for $\tau_x = 500\tau_x$ (red dots) and expected $R = 1$ stochastic web and associated elliptic points, hyperbolic points, and filaments (light blue).
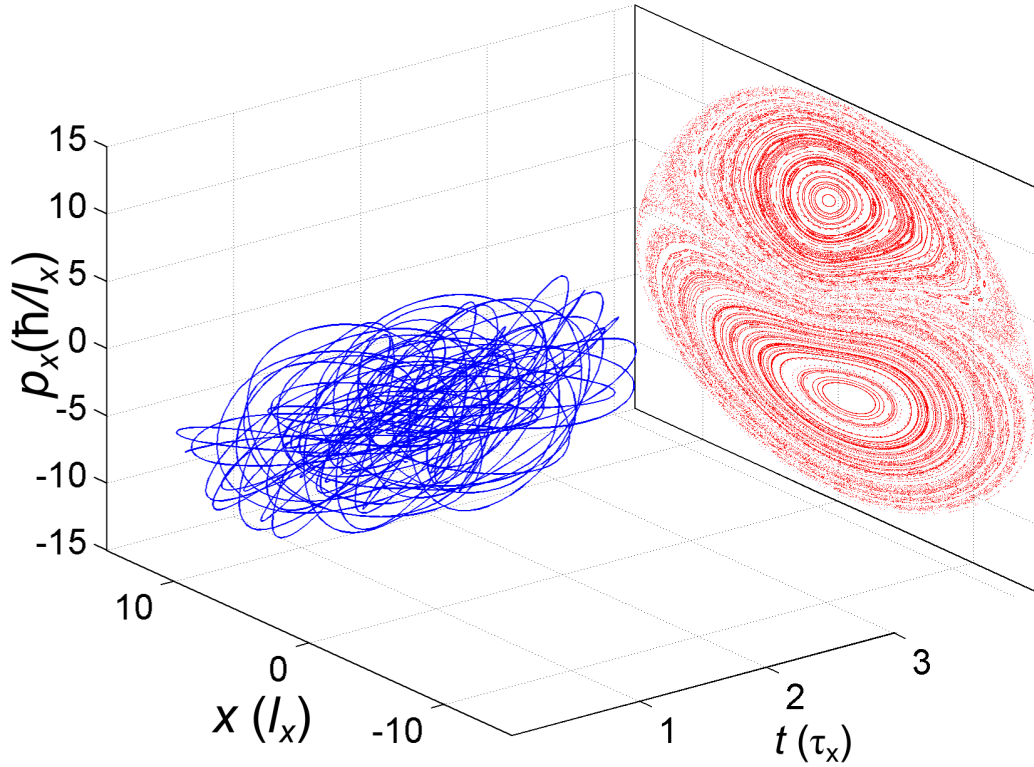
Figure 3.5: Phase space evolution of a single atom with random initial condition in a harmonic trap (blue line), driven by an OL with $U_o = 8\hbar\omega_x, k_l = 0.26/l_x, \omega_l = \omega_x$, Poincaré section plotted as above (red dots) which contains several perturbed stable orbits (solid red ellipses) surrounded by a large chaotic sea (region of evenly distributed red points). Asymmetry in Poincaré section is due to the action of the OL.

quasi-periodic motion (ellipses in the Poincaré section) to occur simultan-
eously with chaotic motion (chaotic seas) depending only on the position in
phase-space [47].

Note that, in the case of large U_o, the stochastic web is asymmetrical in $\pm x$
as although the equations of motion for a harmonic oscillator are completely
symmetric in space and momentum, the presence of the OL potential breaks
this symmetry, an effect more prominent when U_o is large.

Chaotic Evolution in the Quantum System

For a quantum system, chaotic motion cannot be measured by the Lyapunov
exponent, as the uncertainty principle doesn't allow knowledge of a particles
position and momentum with greater uncertainty than:

$$\Delta p \Delta x > \hbar/2. \tag{3.16}$$

Therefore it is impossible to define two atoms with arbitrarily similar
initial conditions. However the *correspondence principle* states that in the
limit of large quantum numbers (in this system, harmonic oscillator states),
or $\hbar \to 0$, the classical description must hold for the quantised system [52].
Therefore we expect to be able to see at least qualitatively similar behaviour
in the two models.

In order to plot the phase-space evolution of the quantum system de-
scribed in equation (3.1) we shall use the Wigner phase-space distribution
given in 1D by [53], normalised to unity by dividing by the total number of
atoms N:

$$W(x, p_x, t) = \frac{1}{N\pi\hbar} \int_{-\infty}^{\infty} \psi(x - \lambda, t)\psi^*(x + \lambda, t)e^{2i\frac{p_x \lambda}{\hbar}} d\lambda, \tag{3.17}$$

where the extraneous dimensions, y and z have already been integrated
over. This distribution function will give the relative occupation of each point
in phase-space (x, p_x) at any point in time t. In order to create an analogous
Poincaré section to those shown above, we will average the distribution func-
tion stroboscopically after every harmonic trap period, $\tau_x = 2\pi/\omega_x$, using:

$$W_{av}(x, p_x) = \frac{1}{N_\tau} \sum_{n=0,1,2,3...}^{N_t} W(x, p_x, t = n\tau_x), \tag{3.18}$$

27

where N_τ is the total number of periods that we will excite the cloud over.

Figure 3.6 a,i-iv) shows instantaneous Wigner functions (not averaged in time) for the evolution of the phase-space distribution of a non-interacting cloud as it's excited from the groundstate a,i) along the phase-space filaments (direction shown by the white arrow, a,ii) until it reaches the stochastic web ring (green dashed line, a,iii) whereupon it scatters around phase-space with a constant phase-space radius, ρ, and begins to travel back along the stochastic filament towards the centre of the plot (as shown by the curved white arrows, a,iv). This excitation, followed by a slight relaxation due to the atoms at least partially returning to the centre of the phase-space, explains the shape of the energy versus time plot shown in figure (3.1 b) in which the atoms' energy greatly increases, reaches a maximum, then partially decreases in energy.

Figure 3.6 shows b,i-iv) shows the creation of the Poincaré section as the Wigner functions are averaged, periodically over time, iv) shows the similarity to the classical results as the averaged Wigner function contains the same phase-space filaments as those shown in figure 3.4. Similarly, the slight asymmetry to the stochastic web is due to the finite size of the OL breaking the symmetry of the harmonic oscillator motion.

Effect of Interactions

The inclusion of inter-atomic interactions can greatly change the dynamics of a system [54, 55]. In the context of phase-space structures, interactions have been shown to cause well defined pathways to become 'blurred', allowing atoms to pass between previously isolated phase-space regions.

Figure 3.7 shows phase-space evolution for the interacting atomic cloud shown in figure 3.1 subjected to the same OL as used in figure 3.6. The stochastic web is only present in the one radial filament (figure 3.7a) along which the cloud initially travels. However, upon travelling around the web ring (figure 3.7b and c), the inter-atomic interactions cause the cloud to scatter throughout the entire phase-space region filling it with low probability density regions (figure 3.7d). As discussed above the interactions have allowed the atoms to travel between the previously isolated stable orbits and spread out, covering the entirety of the phase-space encircled by the web ring (shown as the light blue region).

The fragmentation of the cloud is responsible for the reduced relaxation in the energy shown in figure 3.1, as the cloud no longer travels back along
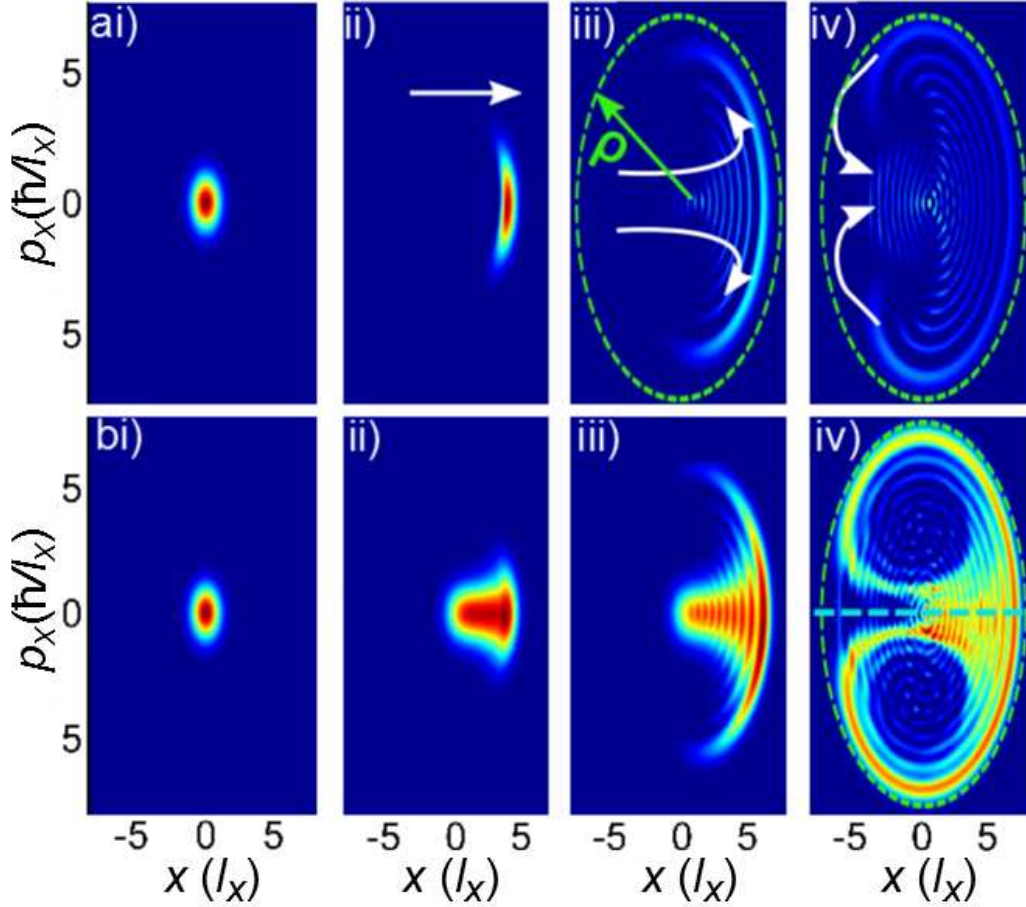
Figure 3.6: a,i - iv) Momentum-position phase space evolution of a non-interacting cloud, hotter colours show higher probability density and white arrows show direction of phase space movement at $t =$ i)0, cloud initially at rest, ii)$10\tau_x$, cloud is excited to larger phase radius along $p_x = 0$ pathway, iii) $25\tau_x$, cloud hits phase space limit and scatters around a ring of constant radius, ρ, as shown by dashed green circle, iv) $38\tau_x$, centre of mass begins to decrease in ρ along $p_x = 0$ pathway, reducing its energy. 3b,i - iv) Periodically averaged momentum-position phase space evolution at $t =$ i)0, cloud initially at rest, ii)averaged over $0-10\tau_z$, noticeable pathway along $p_x = 0$, iii)$0-25\tau_x$ average, radial pathway intersects radial filament iv) 0-75τ_x average shows full stochastic web with radial pathways (blue dashed line) and ring filaments (green dashed line) as predicted by classical theory.
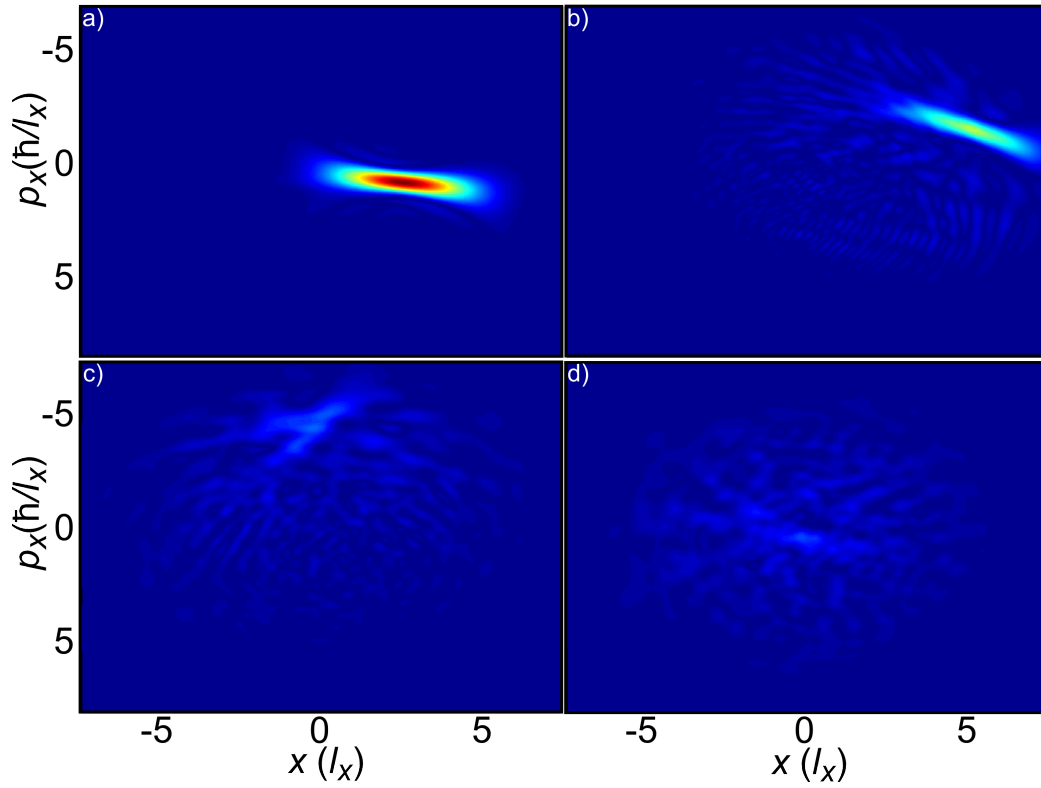
Figure 3.7: Instantaneous Wigner functions for an interacting cloud (parameters given in figure 3.1) subjected to the same OL as used in figure 3.6 a)$t = 5\tau_x$, initial distribution driven along stochastic filament b) $20\tau_x$ leading atoms reach the phase-space ring and begin to fragment and create low probability density regions (light blue), c) $25\tau_x$ atoms entirely scatter around the phase-space ring and d)$35\tau_x$ some atoms return to the centre of the web causing a slight relaxation in the energy of the cloud, however most spread around all phase-space.

the filaments after hitting the web ring limit as shown in figure 3.6 a,iv. Therefore the cloud retains a larger energy. This shows that the excitation is still caused (and limited) by the presence of the stochastic web. However, the inter-atomic collisions act to stabilise the oscillatory nature of the clouds' motion in phase-space.

3.2.3 Controlling the Excitation

Equation (3.12) predicts the phase-space limit of the clouds' excitation, as we have seen that, although the OL can allow travel along the stochastic filaments, there is no expansion past the first hyperbolic point due to the exponential thinning of these filaments. Therefore we can predict that, for any optical lattice wavevector k_l, the maximum phase-space radius of an atom beginning at rest in the middle of the harmonic trap is:

$$\rho_{ring} = \frac{A_R}{k_l},\tag{3.19}$$

where A_R is the first root of a Bessel function of order R (the resonance of the OL, $R = \omega_l/\omega_x$). Therefore the maximum energy that can be reached is given by:

$$E_{ring} = \frac{m\omega_x^2}{2}\left(\frac{A_n}{k_l}\right)^2.\tag{3.20}$$

Figure 3.8 shows the maximum energy reached by an interacting (black points) and non-interacting (red points) cloud of atoms both of which largely agree with the value predicted by equation (3.20) (blue line). The most notable difference is the larger energies reached by the interacting system due to the repulsive nature of the atomic collisions. It has also been shown that these interactions also create more unpredictable excitations as atoms no longer follow the stochastic web, leading to a less smooth relationship with k_l. This is most prominent in the region $0.75/l_x < k_l < 1.25/l_x$ where the wavelength of the perturbation, $\lambda_l = 2\pi/k_l$, becomes comparable, firstly, to the size of the condensate and, secondly, to the healing length of the condensate. An increase in excitation in this regime has been seen in condensates travelling through stationary lattices [56] and similar, though reduced, effects can be seen here.

The maximum, non-interacting, energies are typically less than the predicted values for $k_l < 1/l_x$ as the atoms travel around the stable orbits,
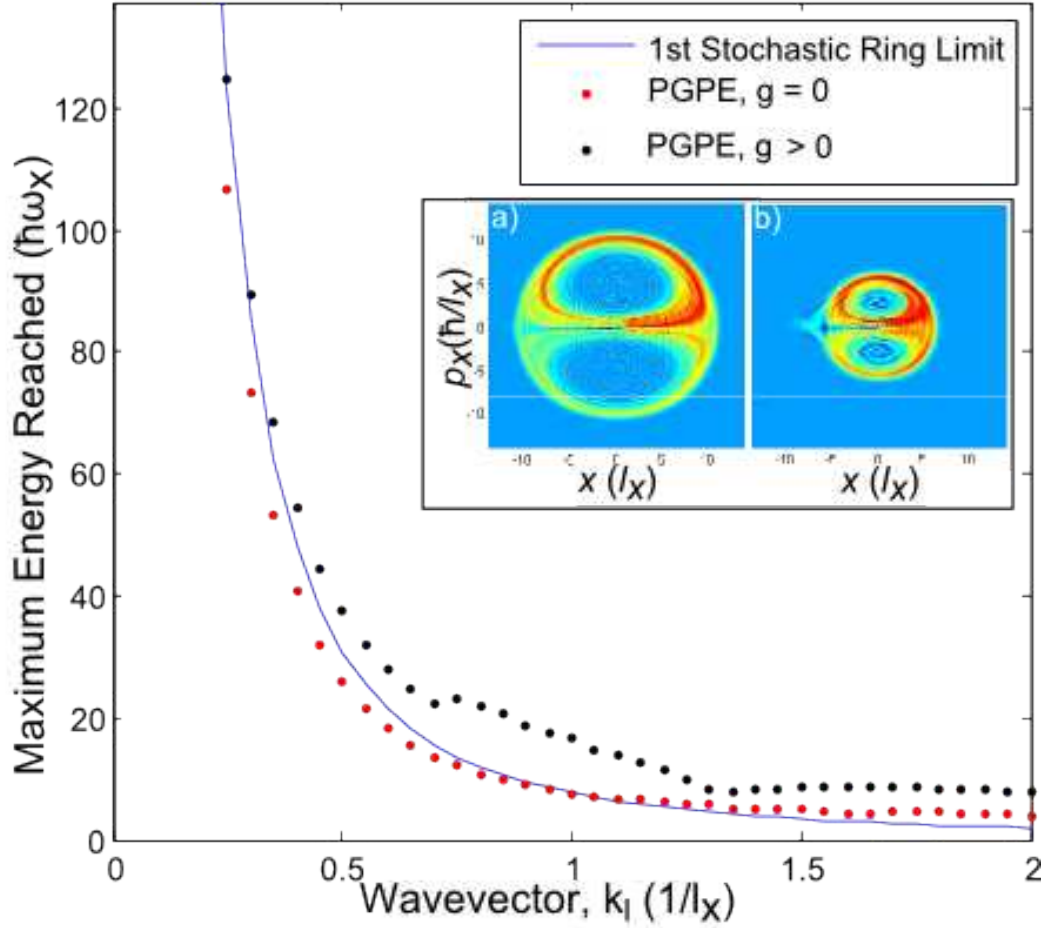
Figure 3.8: Maximum energy reached due to excitation from an OL of varying wavevector, for a non-interacting cloud (red points) and an interacting cloud (black points) and the values predicted by the stationary hyperbolic points of the equations of motion, given by equation (3.20). Inset: Poincaré sections showing the resulting stochastic webs for for OLs with $k_l =$ a) $0.4/l_x$ and b) $0.75/l_x$. U_o was changed to keep the dimensionless driving strength $\epsilon = U_o k_l^2/(m\omega_x^2)$ constant.

which are appreciably smaller than the web ring radius, ρ_{ring}, though this discrepancy is only small in comparison to the maximum energy. However, for $k_l > 1/l_x$ we can see that the energies become larger than those predicted. This is because the initial distribution of atoms is larger in comparison to the size of the stochastic web and so, given long enough excitation, the atoms can begin travelling out of the first stochastic web ring. This effect is shown in inset a) of figure 3.8 which shows the stochastic web for $k_l = 0.4/l_x$ in which all atoms stay within the predicted web ring. Inset b), however, shows that for $k_l = 0.75/l_x$ some atoms have begun exiting the first web ring (light blue region at $x \approx -6l_x$) as more atoms fulfil the requirements on their initial distribution to travel along the stochastic filaments (as explained earlier).

In order to create comparable stochastic webs over a range of wavevectors, the dimensionless driving strength:

$$\epsilon = \frac{U_o k_l^2}{m \omega_x^2} \tag{3.21}$$

was kept constant to ensure the same level of chaoticity was present in the excitations [47].

Figure 3.8 shows confirmation that for typical OL parameters the cloud doesn't significantly pass beyond the first web ring and, as such, can be limited *a priori* using the OL wavevector. However, this doesn't have to be the case because, as shown previously, large OL depths can be used to create large chaotic seas to open the web filaments and create larger heating. Similarly, it has been shown that additional perturbations can be used to open the web filaments [57]. However, both of these methods, whilst increasing the maximum energy for a fixed wavevector, cause less controllable excitations.

3.3   Comparison with Bloch Oscillation

Previously, work has been carried out which incorporates complex atom dynamics inside an optical lattice under the influence of a driving force [22,29–33]. The primary phenomenon considered is Bloch oscillation, wherein the relatively deep ($U_o > E_{atoms}$) and relatively small spatial period ($k_l > k_{atoms}$) of the optical lattice causes the formation of isolated energy bands. Atoms driven by an applied force are then driven to oscillate by the presence of these approximately sinusoidal energy bands. Whilst the majority of this theory originates from solid state physics, as it was first hypothesised

for electrons in a crystal lattice driven by an applied electric field [58], there has been much interest in creating an analogous system of cold atoms in an optical lattice [39–41]. Similarly, utilising Bloch oscillation, chaotic motion has been studied for atoms in optical lattices (e.g. by Monteiro [59]).

However, although the system described in this chapter may seem analogous to those used for Bloch oscillation, it can be shown that the non-KAM chaos seen above is an entirely independent phenomenon. Firstly, if we perform a co-ordinate transform and consider the optical lattice as stationary with a moving harmonic potential, then it may appear that we have the lattice potential and additional driving force required for Bloch oscillation. However, the curvature of the now moving trap means that the applied force is no longer constant and is instead linearly time dependant which will produce a very different evolution to Bloch oscillation.

In addition, periodic Bloch oscillation necessitates that atoms are kept in the same energy band so that the ensuing oscillation is sinusoidal in nature. For this the energy bands must have a sizeable gap between bands, i.e. the atoms are constrained to a single band throughout the evolution. However, if we calculate the energy bands for the relatively shallow ($U_o \lesssim \hbar\omega_x$) and relatively slowly spatially varying ($k_l \sim k_{atoms}$) optical lattices used here, the associated energy bands will have no energy gap and will instead form a connected set of very small energy bands that can instead be approximated as a continuum. This would cause any Bloch oscillation due to these small optical lattices to occur on frequencies of $\sim 100 \times \omega_x$ and with energies of $\sim 10^{-3}\hbar\omega_x$ and so the effects of Bloch oscillation can reasonably be ignored in our discussion of the evolution of the system.

3.4   Conclusion

In this chapter we have shown that the spatio-temporal potential created by oscillating optical lattices can induce strong, controllable, excitations in harmonically trapped atoms and BECs. Firstly, the classical dynamics known as non-KAM chaos were shown to be present in resonantly coupled travelling OLs and trapped atoms. Physical understanding of this system was obtained by using Poincaré sections of the atoms phase-space evolution.

These sections showed how phase-space pathways allow large scale excitation to take place. The form of these phase-space pathways was then used to control the extent to which atoms were excited and it was shown

that changes to the shape of the OL could be used to very precisely control the limit to which atoms are excited. All these effects where shown to persist even in the presence of atomic interactions which acted to stabilise the oscillatory nature of this excitation.

Chapter 4

State Excitation in BECs

4.1 Single State Excitation

In the previous chapter it was shown how well-understood non-KAM chaotic dynamics could be used to excite atoms in a very controllable manner. In the following chapter we will show how this effect can be extended using the quantised nature of harmonic oscillator states to allow single state excitation. Further, using numerical algorithms, it is shown that arbitrary superpositions can be created. These include cat states, which have never previously been observed in such a large macroscopic system as a BEC.

4.1.1 From the Classical to the Quantum Regime

So far, the classical description has agreed very well with the results found from the Schrödinger equation. This is not surprising as we have studied excitations where $E_{ring} \sim 30\hbar\omega_x$ i.e. many times greater than $\hbar\omega_x$, which allows the wavefunction to occupy many states and thus enter a classical, continuum limit as predicted by the correspondence principle. However, if $k_l \geq 2$ and $R = 1$, then $E_{ring} \sim \hbar\omega_x$ and we see different behaviour as the quantisation of the states becomes apparent.

Figure (4.1a) shows the average energy versus time for a 1D, non-interacting cloud subjected to a travelling OL of $k_L = 2$, $R = 1$, and $\epsilon = 0.5$, we can see the usual, initial heating rate as seen previously. However, at some time $\tau_{ex} = 10\tau_x$ this drops and instead we see a strong oscillatory pattern. Figure (4.1b) shows the occupation of the states n against time during this driving
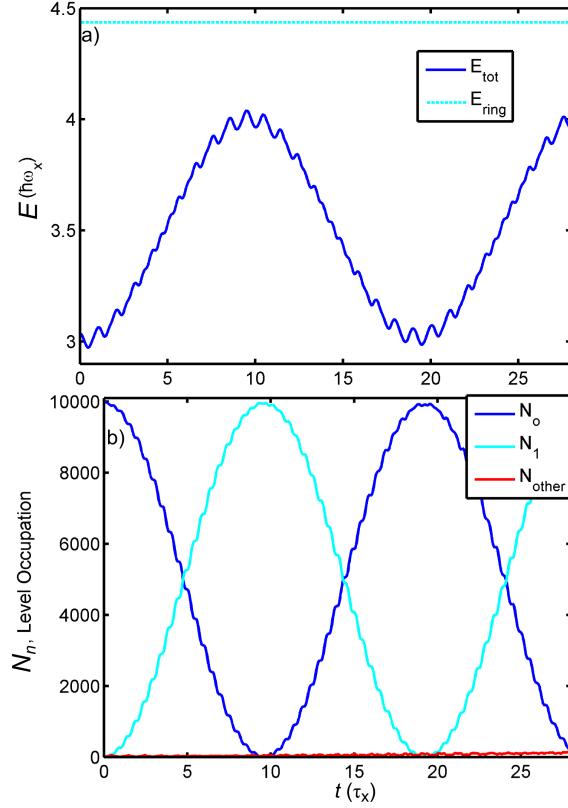
Figure 4.1: a) energy versus time for $k = 2$, $R = 1$, $\epsilon = 0.5$ (dark blue curve) and maximum energy obtainable from classical theory (light blue dashed curve) b) shows occupation inversion of the groundstate (dark blue) to the first excited state (light blue) with very few other states occupied (red) leading to 99.5% inversion.

and reveals that only the $n = 1$ atoms are excited, another break from the classical regime.

4.1.2 State Inversion and Fidelity

Upon further investigation we found that by altering the wavevector, k_l, we could change the maximum energy that was reached much like the classical case. However, this maximum energy was far from the value predicted by the non-KAM chaos description. Instead, the change of wavevector simply

altered the maximum fraction of atoms that were excited to the $n = 1$ state. Further, it was found that if R was changed to any integer value then a wavevector could be found that allowed the excitation of atoms from the groundstate to the $R = n$ state to approximately 100%.
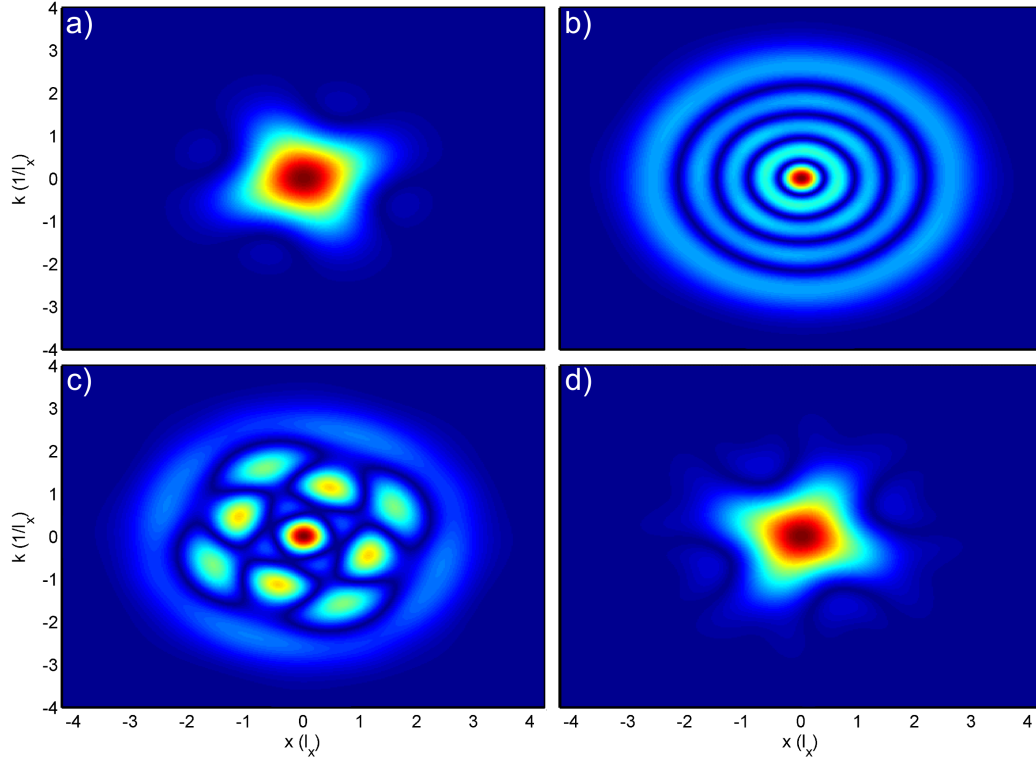
Figure 4.2: Instantaneous Wigner functions showing state inversion from initial groundstate to $n = 4$ state, a)$t = 4\tau_x$ atoms expand along half of the $2R$ radial filaments, b)$41\tau_x$, $n = 4$ state fully formed, c) $56\tau_x$, QHO rings fragment to form the second half of the $2R$ filaments, d)$77\tau_x$, atoms travel back to the centre of phase-space.

Figure 4.2 a) shows the Wigner function of $N = 10^4$ groundstate atoms excited by an $R = 4$, $k_l = 2.1492/l_x$ and $U_o = 0.0364\hbar\omega_x$ OL for $4\tau_x$. The initial Gaussian shape has been perturbed as the atoms travel outwards along half of the $2R$ stochastic filaments as previously seen in figure 3.6. Figure 4.2 b) shows the cloud after $41\tau_x$ in a phase-space distribution of a pure $n = 4$ QHO state, characterised by the 4 concentric circles around a central

38

Gaussian peak. Classical chaos theory would predict that the atoms should travel out in phase to a radius of $x = 6l_x$ or $k = 6/l_x$. However, in this quantised regime, the atoms return to the centre of the phase-space having only reached a maximum phase-space radius given by $\rho = \sqrt{2E_4}$ in dimensionless units. Figure 4.2 c) shows that this relaxation occurs because the fragmenting QHO rings form the remaining half of the $2R$ pathways and the atoms return along these back to the QHO groundstate, as shown in d).

Though the wavevector values required for complete inversion don't appear to have any obvious analytical form, the energy radius as calculated in the previous section for these wavevectors, k_n, follows the simple linear relationship:

$$E_{ring}^{(n)} = \frac{m\omega_x^2}{2}\frac{A_n^2}{2k_n^2} = (1.4517n + 0.4261)\hbar\omega_x. \tag{4.1}$$

Naively, we might assume that $E_{ring}^{(n)} = (n + 1/2)\hbar\omega_x = E_n$, however this does not appear to be the case, exactly why remains an open question.

However, once found empirically, the typical fidelity of the inversion:

$$\eta = \frac{N_n}{N} \tag{4.2}$$

is typically $> 1 - 10^{-4}$ and due to the dimensionless nature of this harmonic excitation the values found will hold for any given trap frequency ω_x.

Figure (4.3) shows the measured fidelities for the $n = 1$-8 excitations (varying colours as labelled) and varying driving strengths $\epsilon = [0.2, 0.4, 0.6, 0.8, 1]$ (decreasing hue). As the level n increases, the width of the fidelity curves for each level become thinner indicating a stricter requirement on the accuracy of k_l. Similarly, the widths, and primarily, the heights of the fidelity curves diminish with increasing driving strength. The presence of deviations in the inverted parabolas (present in $n = 1$ and 2 for $\epsilon > 0.6$) show an increase in the chaotic dynamics as expected with larger driving strengths, which greatly decrease the inversion fidelities.

Comparison with a Similar Experiment

Recently, an experiment was carried out in which a numerical scheme was used to calculate how to shake a very specific, non-harmonic trap in order to excite an interacting cloud of ^{87}Rb into the first excited state, $n = 1$ [60]. Numerically the investigators found this process could be carried out with
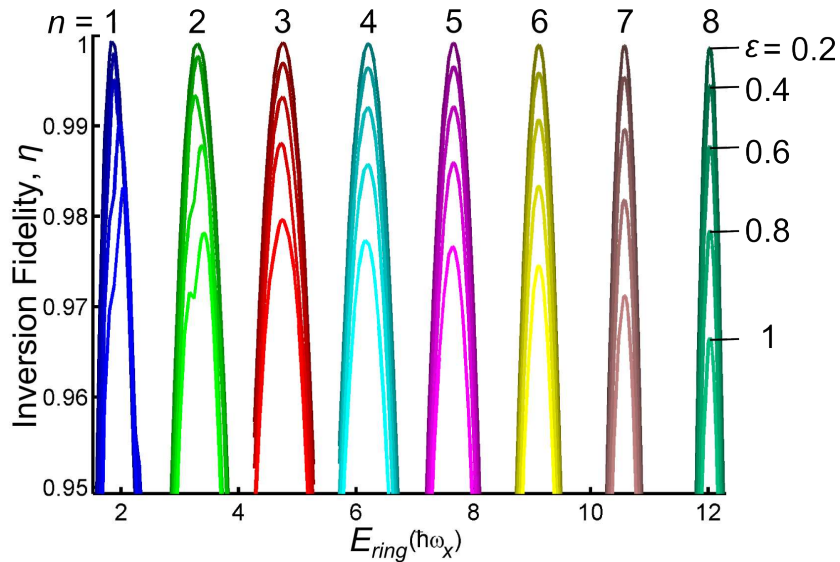
Figure 4.3: The fidelities of the $n = 1\text{-}8$ (varying colours as labelled) occupation inversions under varying E_{ring} and varying driving strengths ϵ resulting in decreasing fidelities (decreasing hues as labelled). Note the slight thinning of the fidelity distributions with increasing n.

a fidelity of $\eta \approx 1 - 10^{-3}$. However, due to experimental issues such as the limited accuracy of the non-harmonic trap, the effect of interactions, and the finite bandwith of the electronics responsible for the trap shaking, the experimentally found fidelity was ~ 0.97.

For the travelling OL scheme using $\epsilon = 0.2$ the inversion error is an order of magnitude smaller than the theoretical method used in the investigation described above. The major difference between these two schemes is that the shaking method used an interacting cloud and a very specifically designed anharmonic trap in order to carry out the excitation. For the travelling OL we greatly simplify things by assuming no interactions between atoms (i.e. by choosing atoms with naturally very small collisional cross-section or alternatively through the use of Feschbach resonances) and using a reasonably harmonic trap (i.e. contains no large anharmoncities for atoms of energies $\sim E_{ring}$). This then only requires the OL to be well described by the travelling wave potential and, as shown by figure (4.3), large fidelities $\eta > 0.99$ can still be achieved even with limited accuracy in the OL creation.

Lastly, the previous technique was restricted to studying only one exper-

imental set-up with a very strict requirement on the number of atoms and interaction energy as the scattering length of the ^{87}Rb added an absolute length scale to the system. This also restricted them to only exciting atoms to the first energy level. In the limit of no interactions, however, all the results shown in the above technique are dimensionless in nature and scale with the trap frequency, ω_x, and so will allow any experimental set up to excite atoms to the nth level.

4.1.3 Coupled State Equations

Though there appears to be no obvious relationship for the wavevector and fidelity, much of the excitation of the atoms can still be described analytically. If only two states are coupled via the OL then we can expand the 1D mean field wavefunction into just those states:

$$\psi(x,t) = a(t)\phi_o(x) + b(t)\phi_n(x), \tag{4.3}$$

where a and b are complex expansion coefficients that satisfy $|a(t)|^2 = N_o(t)$ and $|b(t)|^2 = N_n(t)$ and as only these two states are occupied then $N = N_o(t) + N_n(t)$ where N is the total number of atoms. We can then take the dimensionless Schrödinger equation:

$$i\frac{d\psi}{dt} = -\frac{1}{2}\nabla^2\psi(x,t) + \frac{x^2}{2}\psi(x,t) + \frac{\epsilon}{k^2}\sin(kx - nt)\psi(x,t) \tag{4.4}$$

and, integrating through by $\phi_o(x)$, we obtain:

$$i\frac{da}{dt} = \frac{1}{2} + a\,C_{oo}\sin(nt) + b\left[C_{on}\sin(nt) + S_{on}\cos(nt)\right]. \tag{4.5}$$

Similarly, integrating through by $\phi_n(x)$, we obtain:

$$i\frac{db}{dt} = n + \frac{1}{2} + b\,C_{nn}\sin(nt) + a\left[C_{on}\sin(nt) + S_{on}\cos(nt)\right]. \tag{4.6}$$

The coupling constants are given by:

$$C_{\alpha\beta} = U_o \int_{-\infty}^{\infty} \cos(kx)\phi_\alpha(x)\phi_\beta(x)dx \tag{4.7}$$

$$= U_o\,(-1)^{\frac{\beta-\alpha}{2}}\sqrt{\frac{2^{\alpha-\beta}\alpha!}{\beta!}}k^{\beta-\alpha}e^{-\frac{k^2}{4}}L_\alpha^{\beta-\alpha}\left(\frac{k^2}{2}\right) \equiv \epsilon I_{\alpha\beta}^c \tag{4.8}$$

41

for $\alpha < \beta$ and the parity of $\alpha \times \beta$ is even or $C_{\alpha,\beta} = 0$ and

$$S_{\alpha\beta} = U_o \int_{-\infty}^{\infty} \sin(kx)\phi_\alpha(x)\phi_\beta(x)dx \tag{4.9}$$

$$= U_o \left(-1\right)^{\frac{\beta-\alpha-1}{2}} \sqrt{\frac{2^{\alpha-\beta}\alpha!}{\beta!}} k^{\beta-\alpha} e^{-\frac{k^2}{4}} L_\alpha^{\beta-\alpha}\left(\frac{k^2}{2}\right) \equiv \epsilon I_{\alpha\beta}^s \tag{4.10}$$

$L_\alpha^{\beta-\alpha}\left(\frac{k^2}{2}\right)$ is the generalised Laguerre polynomial and we assume $\alpha < \beta$, the parity of $\alpha \times \beta$ is odd or $S_{\alpha,\beta} = 0$. These were calculated using integrals 7.388, 6 and 7 of [61] along with the definition of a normalised Hermite polynomial given earlier.

The overlap integrals of interest are given by:

$$C_{on} = U_o \left(-1\right)^{\frac{n}{2}} \frac{e^{-\frac{k^2}{4}}}{\sqrt{2^n n!}} k^n \tag{4.11}$$

and

$$S_{on} = U_o \left(-1\right)^{\frac{n-1}{2}} \frac{e^{-\frac{k^2}{4}}}{\sqrt{2^n n!}} k^n = -iC_{on}. \tag{4.12}$$

We can further simplify equations (4.5) and (4.6) by using the parity arguments $S_{oo} = S_{nn} = 0$ and choosing the parity of the nth state. For the following derivation we assume that n is even, so that $S_{on} = 0$ and only the $C_{\alpha\beta} \sin(n\omega_x t)$ terms are non-zero in equations (4.5) and (4.6). Though it can be shown that the ensuing derivation holds for odd n as well.

To progress, we now split the evolution of the occupation coefficients into the evolution of the state occupations (N_o and N_n) and the phases of each state (θ_o and θ_n). For this we use the Madelung transformations in the QHO basis:

$$a(t) = \sqrt{N_o(t)}e^{i\theta_o(t)} \tag{4.13}$$

and

$$b(t) = \sqrt{N_n(t)}e^{i\theta_n(t)}. \tag{4.14}$$

Substituting these into equations (4.5) and (4.6) and separating into real and imaginary parts we produce the coupled occupation-phase equations:

$$\frac{dN_o}{dt} = C_{on}\sqrt{N_o(N - N_o)}\sin(\theta)\sin(nt) \tag{4.15}$$

and

$$\frac{d\theta}{dt} = n - \left[C_{nn} - C_{oo} - C_{on}\left(\sqrt{\frac{N_o}{N - N_o}} - \sqrt{\frac{N - N_o}{N}}\right)\cos(\theta)\right]\sin(nt), \tag{4.16}$$

where $\theta = \theta_n - \theta_o$ is the relative phase between atoms in the two states.

Solving for the Excitation Time

Although the coupled ODEs above aren't immediately solvable, we can make the weak driving approximation: $C_{oo}, C_{on}, C_{nn} \ll n$ i.e. either the spatial over lap of the modes with the OL is very small or the depth of the OL is much less than the energy of the nth state. Under these conditions it is then trivial to solve for $\theta \approx nt$, assuming the initial phase difference is 0.

We can then integrate equation (4.15) to obtain a simple relationship for the excitation period τ_{ex}, using:

$$\int_N^0 \frac{dN_o}{\sqrt{N_o(N - N_o)}} \approx C_{on}\int_0^{\tau_{ex}}\sin(nt)^2 dt$$

$$\pi \approx C_{on}\left[\tau_{ex} - \frac{\sin(2n\tau_{ex})}{2n}\right]. \tag{4.17}$$

This is then solved by the two following conditions:

$$\tau_{ex} = \frac{\pi}{C_{on}} \tag{4.18}$$

and

$$2n\tau_{ex} = l\pi, \tag{4.19}$$

where l is any positive integer. These can both be met by using the definition of the coupling coefficients given earlier and placing a requirement on the driving strength:

43

$$\epsilon = \frac{2n}{lI_{on}^c}. \tag{4.20}$$

The occupation of the nth state can be found by integrating equation (4.17) over time, t:

$$N_n(t) = N_o \sin\left(\frac{\pi t}{\tau_{ex}}\right). \tag{4.21}$$

With the equations given above we can *a priori* excite a pre-determined fraction of atoms from the groundstate into any state n. This is carried out by finding the correct wavevector using equation (4.1) then choosing the lattice depth according to equation (4.20).

Difficulties with Cooling

Whilst the above analytic description of level coupling via an optical lattice seems as if any state can be created, we have assumed at all times that the atoms begin in a non-interacting groundstate. This means that all the atoms have a single phase θ, and, as discussed, if this were not the case then the previous derivation would not hold. Therefore if we were to begin with a thermal ensemble of atoms, even if it were still well described by a coherent mean-field, it would be impossible to perform any set of operations that would reliably place all the atoms into the groundstate. This is due to the mixture of semi-resonant coupling between levels and the mixture of phases and so would almost certainly cause further heating (due to the large number of higher energy states). Therefore we may be able to controllably de-excite atoms from a single excited state to the groundstate. However, we cannot reasonably call this cooling as the initial state was not in thermal equilibrium.

4.2 Creating Cat States and Arbitrary Superpositions

So far we have excited atoms from the non-interacting groundstate into other harmonic oscillator states which are analogous to photon Fock states [62,63] as each state contains a definite number of particles, i.e. at any moment in time there is no uncertainty of the number of particles in any given state.

Equivalently, we can say that our wavefunction, ψ, is an eigenvector of the number operator, $\hat{N}_n$:

$$\hat{N}_n|\psi\rangle = a_i^\dagger a_i|N_0, N_1, N_2...\rangle = N_n|\psi\rangle \tag{4.22}$$

where $a_i^\dagger$ and a_i are the particle creation and annihilation operators, respectively and N_n is the occupation of the nth quantum harmonic oscillator basis state [63]. Note that this limits our discussion to non-interacting particles, as interacting wavefunctions (when $g \neq 0$) will be superpositions of these states and so are not eigenvectors of $\hat{N}_n$.

Previously, photon Fock states have been used to carry out high precision quantum metrology experiments in a range of fields. A simple explanation and review can be found at [64]. However, it has been shown that increased precision can be obtained using coherent and entangled states, e.g. [65]. Coherent states can be created by atoms in a superpostion of Fock states given by:

$$|\alpha\rangle = e^{-\frac{|\alpha|^2}{2}} \sum_{n=0}^{\infty} \frac{\alpha^n}{\sqrt{n!}}|n\rangle, \tag{4.23}$$

where α is the order of the coherent state (which can be non-integer and complex). Coherent states were first derived by Erwin Schrödinger in 1926 as quantum mechanical states that would satisfy the correspondence principle and behave in a similar manner to classical atoms in a harmonic trap. Consequently, they appear as a Gaussian distribution in phase-space with a single localised peak, i.e. they appear to have one well defined value for position and momentum, subject to the uncertainty principle [66].

Cat states are the entangled superposition of two coherent states so as to create a non-classical state, which allows atoms to have two separated and well defined positions in phase-space, analogous to Schrödinger's thought experiment in which a cat is both alive and dead at the same instance in time. The general description of a cat state is:

$$|\text{cat}\rangle = |\alpha\rangle - e^{i\theta}|-\alpha\rangle, \tag{4.24}$$

where θ is a phase-angle between the coherent state $|\alpha\rangle$ and the anti-phase state $|-\alpha\rangle$. For simplicity, we shall use $\theta = \pi$ thus ensuring that the two Gaussian states are in complete anti-phase with one another. These are known as 'even' cat states because, due to the $(-\alpha)^n$ term in the summation

for the anti-phase coherent state, only even Fock states survive the addition of the two coherent states. A similar 'odd' cat state can be created using $\theta = 0$ or 2π. In this case, only the odd states survive although, as explained later, this would be considerably harder to create.

However, we must state that this is a non-interacting system and so the cat states given by equation 4.24 will produce a mean-field wavefunction with atoms that are evenly distributed between the two coherent states. This is because for a non-interacting system, taking many repeated measurements as to which coherent state a single atom is in must be equivalent to taking a single measurement for many atoms. Therefore an interesting question arises as to whether cat states produced with non-interacting atoms in this mean-field description are superpositions of single atom states or many-body states and whether this allows them to be called '*true* cat states. Whilst we do not answer this question here and highlight the above caveat in labelling cat states, it presents an interesting avenue of further investigation.

4.2.1 Semi-Resonant Coupling

So far we have only shown that atoms in the groundstate can be excited to a single QHO level. In order to create superpositions we must be able to excite atoms to one state and then perform subsequent excitations to promote atoms to other levels. However, the OL will still be felt by the first set of excited atoms and will excite them into other, unwanted states.

Figure 4.4 shows the final state occupations after a third of the initial groundstate atoms have been excited to the 6th QHO state and a third have subsequently been excited to the 9th QHO state (blue points) both with OLs defined by the required parameters given in the previous section. The red circles indicate that if there had been no coupling between the atoms in the 6th and the second OL operation, i.e. there would be a third of the atoms in the groundstate, 6th and 9th QHO states. However as shown there are also many atoms now inhabiting QHO states given by:

$$n_{semi} = |\pm an_1 \pm bn_2| \tag{4.25}$$

where n_1 and n_2 are the two excited states (in this example 6 and 9) and a and b are integers. This semi-resonant coupling greatly increases the complexity of creating superpositions beyond just the groundstate and one other state. Lastly, the black crosses in figure 4.4 show the final state occupations
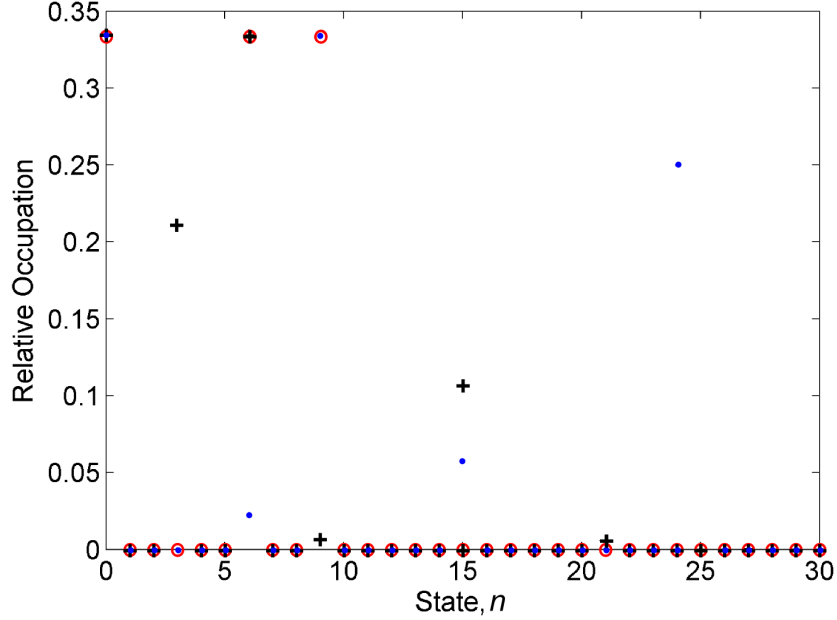
Figure 4.4: State occupations after attempting to create a superposition comprising of a $1/3$ of the atoms in the groundstate, 6th and 9th states, after carrying out required OL excitations (blue points), resulting in a fidelity of 62%, reversing the order of excitations (9th then 6th) produces 75% fidelities (black crosses), the occupations of the desired superposition are shown by red circles.

after the excitations have been carried out in the reverse order, i.e. a third of the groundstate atoms excited to the 9th state then a third excited to the 6th state. These crosses show a reduced amount of semi-resonant coupling as the second operation takes considerably less time (as shown earlier $\tau_{ex} \sim \sqrt{2^n n!}$) and so perturbs the already excited atoms far less.

To lessen the difficulties created by semi-resonant coupling, we will only consider creating cat states that contain even parity QHO states. This means that all driving by the OL can be carried out by a standing cosine wave, as its even parity will ensure that the groundstate and any semi-resonant coupling will only ever cause atoms to occupy the even QHO states. If we were to create odd cat states, in order to excite atoms into the odd QHO states an odd parity sine wave would be needed, which would semi-resonantly excite atoms to *both* odd *and* even QHO states.

4.2.2 Fidelity and Optimisation

Due to the sizeable number of modes that are needed to create a cat state there will significant semi-resonant coupling as atoms are excited into the required states. This coupling is hard to predict and, as many states become occupied, will become a major factor in how states are filled. Therefore, there appears to be no analytical prediction of the OL lattice operations needed to produce the correct distribution of atoms.

Instead, we will use a numerical approach wherein we perform a series of excitations in descending order of state, starting with the highest order state that has an occupation of $> 0.01\%$ of the total number of atoms, and working backwards until we excite atoms to the lowest occupied state. This excitation process is carried out in reverse order to limit the semi-resonant coupling as discussed above. We then use a numerical technique based around a genetic algorithm, which is explained in detail in appendix B. This alters the length of time that the excitation is applied for during each excitation. To find the optimum set of OL excitations, we maximise a phase varying fidelity given by:

$$\eta = \max \left[\left| \sum_n C_n^* B_n e^{in\varphi} \right| \right]_\varphi , \tag{4.26}$$

where C_n are the QHO state expansion co-efficients given by the resulting PGPE simulation and B_n are those required by the cat state being created, given by equations (4.23) and (4.24). The phase φ is used to calculate the overlap between the state found by the PGPE and the cat state as it oscillates in time. We use φ over a range of $0 \to 2\pi$ and take the maximum value of the fidelity for the optimisation algorithm.

To increase the efficiency of this optimisation, we assume that all states above the largest state we are exciting are perturbed out of resonance or semi-resonance with the OL. This could be experimentally produced by creating a dimple trap consisting of a low frequency trap, which contains in the centre a high frequency trap of a depth equal to the highest state that we wish to excite.

Lastly, the duration of each OL operation is limited so that a full excitation of atoms from the groundstate to each excited state (assuming no other states are occupied) will take $\tau_{ex} = 3\tau_x$. To do this we use equation (4.18) to define the required OL depth for each level excitation. This short times-

cale will require very deep optical lattices and will cause particularly chaotic dynamics, which will not give very good single-state excitation fidelities as shown in figure 4.3. However, this effect is no larger than the semi-resonant coupling and will therefore be corrected for in the optimisation algorithm whilst simultaneously ensuring that the procedure for creating cat states won't take prohibitively long times to carry out experimentally.

4.2.3   Results

Figure 4.5 a) shows the Wigner function of a state created by an optimised series of OL operations in order to create an $\alpha = 1$ even cat state, b) shows the Wigner function of the target cat state. As $\alpha = 1$, the bimodal distribution that characterises the cat state is obscured because the finite width of the two Gaussian distributions is larger than the separation between them. Note that the distribution is rotated slightly (i.e. does not lie along the x or k axes) because the created cat state is produced with $\varphi = 0.683\pi$ phase. Figure 4.5 c) shows a schematic of the duration of each OL excitation required, where the length of each horizontal line shows the duration of each OL excitation. The decreasing height shows the descending order in which the excitations were carried out. As only 3 separate excitations were carried out the optimisation routine was quick to produce a particularly high fidelity of $\eta = 0.999$. As described earlier, the OL parameters for each step are set using $U_o = f(\tau_{ex} = 3)$, $k_l = f(E_{ring}^{(n)})$ and $\omega_l = n\omega_x$.

Figure 4.6 a) shows the Wigner function of a created $\alpha = 2$ even cat state, b) shows the Wigner function of the target cat state, c) shows a schematic of the duration of each OL excitation required. As $\alpha = 2$, the bimodal distribution of the cat state can clearly be seen in the two circular peaks at $x = \pm 5l_x$, showing that each atom has sizeable probability of being in two distinct phase-space positions at a given time. There is also a very noticeable interference pattern in the centre of the distribution, which is only present for $\theta = \pi$ cat states and can be used as a measure of the coherence between the two peaks [67]. The large negative regions (dark blue) in this interference pattern shows the non-classicality of this state as negative probabilities have no classical explanation.

Figure 4.7 a) reveals the Wigner function of a state created by an optimised series of OL operations in order to create an $\alpha = 3$ even cat state, b) shows the Wigner function of the target cat state, c) shows a schematic of the duration of each OL excitation and shows the requirement for an increasing
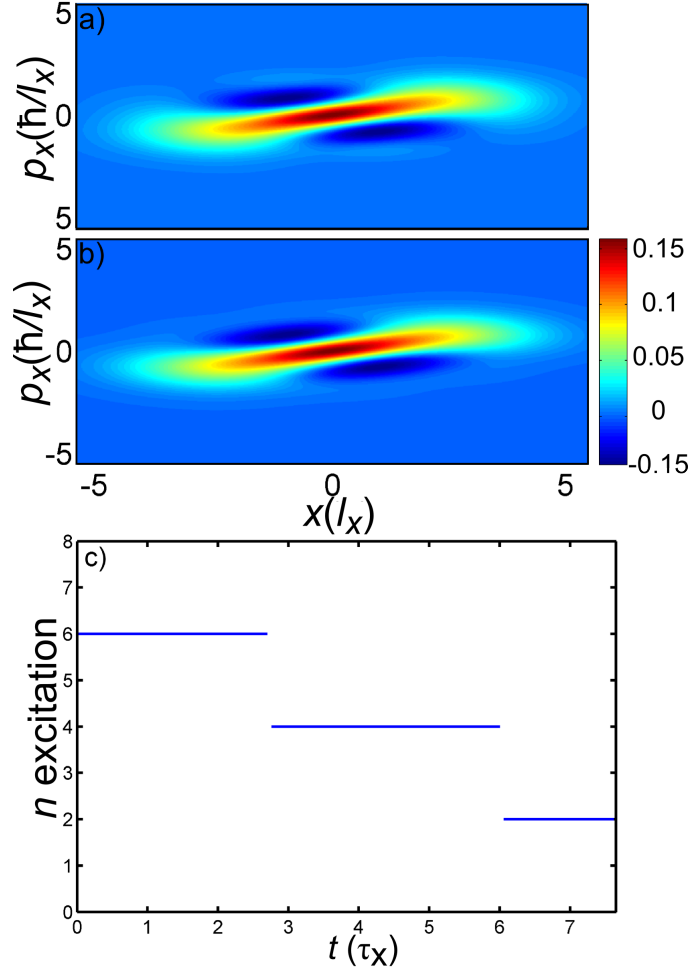
Figure 4.5: a) Wigner function showing the position-momentum phase-space distribution of a created $|1\rangle + |-1\rangle$ cat state, produced with a fidelity of 99.9% of the target state shown in b), the colour bar shows the relative probabilities for both plots, c) shows the series of OL excitations required, horizontal length indicates the length of time required for each operation.

number of steps with the order of the cat states; 3 for $\alpha = 1$, 5 for $\alpha = 2$ and 7 for $\alpha = 3$. The number of operations is related primarily to how many QHO states are needed in the summation in equation (4.23) which increases for larger α as the coherent states become less and less similar to the QHO Fock states, i.e. there is less and less overlap between the coherent state and
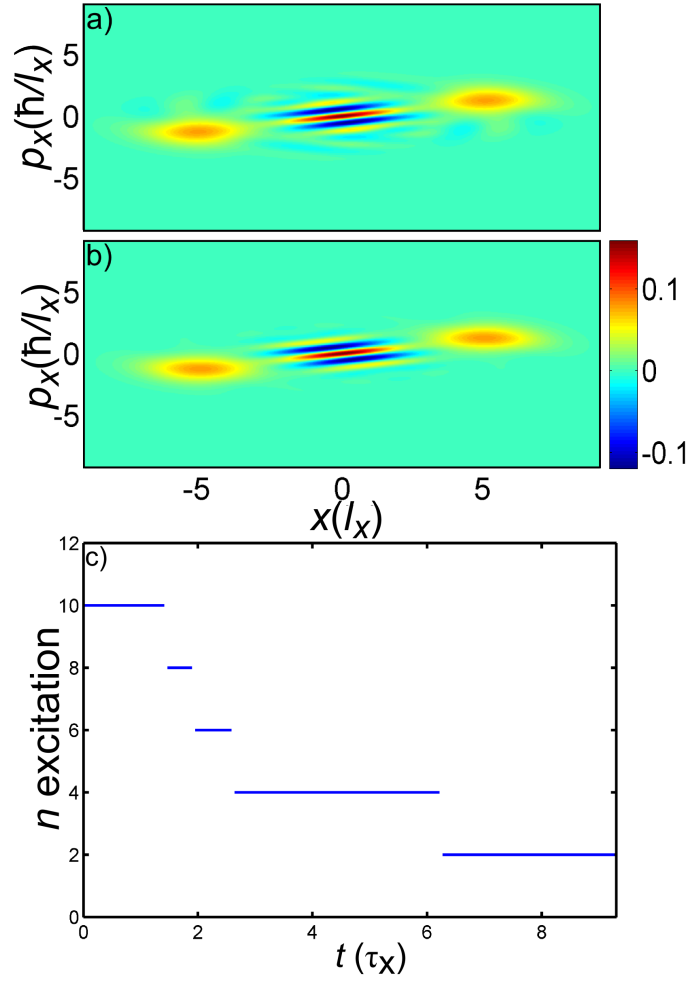
Figure 4.6: a) Wigner function of the created $|2\rangle + |-2\rangle$ cat state, produced with a fidelity of 99.2% of the target state shown in b), colourbar shows the relative probabilities for both plots, c) shows the series of OL excitations required.

any given single QHO state, though the exact numbers used are only chosen for numerical efficiency as described above.
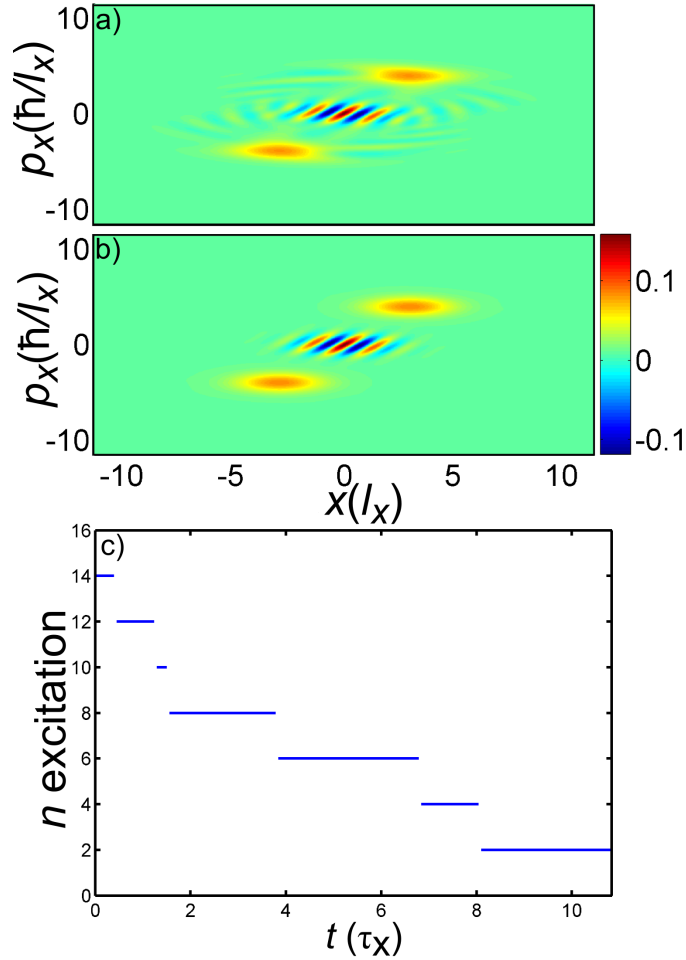
Figure 4.7: a) Wigner function of the created $|3\rangle + |-3\rangle$ cat state, produced with a fidelity of 98.5% of the target state shown in b), colorbar shows the relative probabilities for both plots, c) shows the series of OL excitations required.

4.3 Conclusion

Following the demonstration of clear agreement between the classical dynamics and the results from a quantum mechanical model in the previous chapter, we showed that OL parameters can be chosen which induced non-classical behaviour as the quantised level spacing in the harmonic trap begins to play a role. This quantum-mechanical effect can be harnessed to allow atoms to

be excited from a non-interacting groundstate to any other single trapped energy level with great precision and control.

Creating arbitrary superpositions using this single-state excitation technique is problematic as semi-resonant coupling allows atoms to be excited to multiple different unwanted states. However using a mixture of a genetic algorithm and the Nelder-Mead minimisation algorithm we found that a series of OL excitations could be used to excite atoms into predetermined superpositions. To the authors knowledge, the examples shown, namely three different even parity cat states, have never been observed in this macroscopically occupied, mean-field, system. However, for clarity, we state again that this is a non-interacting system and so the Wigner quasi-probability functions show equivalently, the probabilities of finding one atom at a given position in phase-space after many repeated measurements and the probability of finding many atoms at a given position in phase-space after one measurement. Therefore, it remains an open question as to whether these states are then "true" cat states, which require the states to be a many-body state, or if they are simply a superposition of single atom states. If it is the former, then the closest similar proposal thus far has been using small numbers of atoms in mixtures of internal spin states [46]. Consequently, the results presented here allow for many novel experimental systems to be realised.

Chapter 5

Optimal Near Surface BECs

5.1 Introduction

Bose-Einstein condensates have been routinely created for a number of years [7, 68, 69]. One area of growing interest in this field is how such an ensemble of atoms interacts with macroscopic surfaces such as micro-mechanical semiconductor structures [70] and atom chips designed to hold atoms very close to their surface [71]. The interest is firstly because this is an interface between two very disparate systems; a very small, low energy, quantum mechanical BEC and a relatively large, hot, classical object. Secondly, there are many practical applications for a near-surface BEC such as cooling a micromechanical device [72] or the miniaturization of the entire BEC experimental set-up [73].

The aim for such interfaces is to ensure strong, coherent, coupling between the BEC and the surface, whilst maintaining experimentally useful lifetimes for the trapped atoms. This is made difficult as the scale of imperfections in the surface structures of typical devices become sizeable on the distance scales of interest (typically sub-micron). The effect of the imperfections in the electronic structures, such as the trapping wires, usually manifest in "rough" trapping potentials that add spatially varying anharmonicities. These effects can often be large enough to cause observable deviations in the BEC density or, in extreme cases, fragmentation of the entire cloud. Other effects, such as finite temperature fluctuations in the current [74] and the effect of surface adsorbates and imperfections, [72] will also play a role in creating additional perturbations to the expected trapping potentials.

Similarly, other variables such as the atom species, atomic state and additional magnetic and electric fields can also alter both the interaction of the atom with the surface as well as other loss mechanisms [75–78]. However, in the following chapter we limit our investigation to the role played by the intrinsic Casimir-Polder interaction between a typical BEC of Rb[87] atoms and a stationary dielectric surface. This is because the interaction will affect the potential felt by the atoms in a particularly strong and predictable manner and, as shown in the previous sources, is a considerable issue in many experimental systems.

5.2 The Casimir-Polder Atom-Surface Attraction

The Casimir-Polder force between two neutral atoms in a vacuum can be considered as the quantum-mechanical analogue of the classical Van-der-Waals attraction, where the instantaneous dipoles of two atoms causes an attraction [79]. In more detailed terms, it can be show to arise due to the quantisation of vacuum fluctuations between two atoms leading to a net potential minimum between them [80].

Figure 5.1 shows a schematic representation of this interaction between a neutral atom (shown in red) and a surface (shown in blue). If the atom has an instantaneous dipole, $\underline{d}$ (indicated by the black arrow) then the resulting effect on the surface can be modelled by a mirror dipole $-\underline{d}$. As with the Van-der-Waals attraction, the potential between the atom and the surface can be described in terms of the size of the dipole and a power-law dependence on the atomic separation. The energetic shift, U, of a dipole in an electric field $\underline{E}$ goes as:

$$U \sim -\underline{E}.\underline{d}. \tag{5.1}$$

The dipole, in this case, is that of the near surface atom and the electric field is due to the close proximity of the mirror dipole:

$$\underline{E} \sim -\frac{d}{\Delta^3}, \tag{5.2}$$

where Δ is the atom-surface separation. We then see the energetic shift:
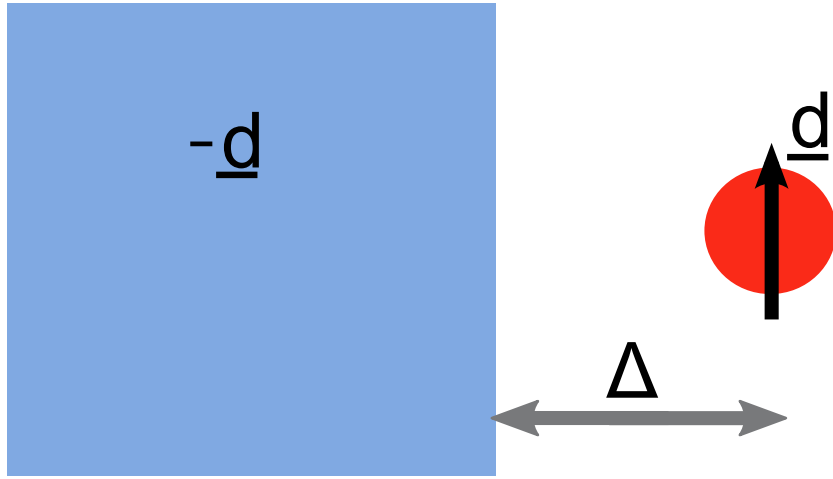
Figure 5.1: Schematic of the classical interpretation of the Casimir-Polder interaction between an atom (red) and a bulk solid (blue). The instantaneous dipole $\underline{d}$ causes a mirror dipole to be created in the surface, $-\underline{d}$. These then interact via the electric fields created by the dipoles. Due to the dipoles' opposing nature, this interaction is strongly attractive.

$$U \sim -\frac{d^2}{\Delta^3}, \tag{5.3}$$

where d is the magnitude of the dipole. From this simple understanding we see that the potential shift, U, is always negative and the interaction is attractive. The attraction is also given by a negative power law relationship with distance and so quickly increases with decreasing separation.

Many other factors will affect the exact magnitude and spatial form of the attraction, such as the relative polarisations of the surface and BEC atoms. Similarly, the geometry of the surface will play a role, i.e. can it be treated as a semi-infinite solid or will finite size effects play a role [81]. Lastly, relativistic effects will also need to be included, as often the finite-time taken for the interaction, $\tau_{int} \sim \Delta/c$, will be comparable to $\tau_{level} \sim \hbar/E_{level}$, the period of the energetic level, E_{level}, in the atom which creates or feels the instantaneous dipole. All of these effects must be taken into account, the details of which are presented [81].

The materials we will investigate are bulk silicon nitride (SiN), thin membranes of silicon nitride and sheets of graphene. These are of interest as bulk

silicon is the mainstay of semiconductor devices and chip traps. Increasingly however, the structures being created are have micron-scale thicknesses and so we need to investigate how this affects the strength of the interaction. For this reason, we will consider silicon membranes. Lastly, graphene is currently being investigated for its many useful electronic and structural properties, which include the possibility of high-quality chip traps.

As explained above, the Casimir-Polder potential can be approximated by a power-law relationship of the form:

$$U_{CP} \approx -\frac{C_j}{\Delta^j},\tag{5.4}$$

where C_j is a real, positive, potential co-efficient and j is the approximate power used to model the spatially-varying potential. The following table gives the approximate power law potentials we will use for the three materials:

Substance	Power Law, j	Co-efficient	References
Silicon Nitride (bulk)	4	$C_4 = 8.2513 \times 10^{-56}$ Jm^4	[?]
Silicon Nitride (membrane)	5	$C_5 = 5.8045 \times t \times 10^{-55}$ Jm^5	[81]
Graphene	4.238	$C_{4.238} = 1.0242 \times 10^{-58}$ Jm$^{4.238}$	[83]

where the values for graphene were approximated in the region $\Delta = 0.2 - 0.75\mu$m where most atomic loss from reasonably tight traps will occur and t is the thickness of the SiN membrane, which we will take to be 0.1 μm [82].

5.2.1   The Casimir-Polder Effect on Trap Potentials

Due to the attractive nature of the Casimir-Polder interaction, we can surmise that the trap centre will be pulled towards the surface, as well as having its frequency reduced. We also expect a global decrease in the trap potential. Therefore, if we create a harmonic trap transverse to a surface, initially centred at position δ_z, with unperturbed frequency ω_o, and a constant, positive, potential offset, δU, we obtain a total potential:

$$U_{tot} = \frac{m\omega_o^2}{2}(z - \delta_z)^2 - \frac{C_j}{(\Delta + z)^j} + \delta U,\tag{5.5}$$

where the surface is situated at $z = -\Delta$. To see what effect this perturbation has on the trapping potential, we can use a Taylor series expansion around $z = 0$ on the power law potential, which gives:

$$U_{tot} = \frac{m\omega_o^2}{2}(z - \delta_z)^2 - \frac{C_j}{\Delta^j}\left[1 - \frac{j}{\Delta}z + \frac{j(j+1)}{2\Delta^2}z^2 + \mathcal{O}(z^3)\right]. \qquad (5.6)$$

If we then equate this to a new, effective, harmonic trap with frequency, ω_z, centred at $z = 0$, at distance Δ from the surface and with the constant energy offset now equal to 0, we find:

$$U_{eff} = \frac{m\omega_z^2}{2}z^2. \qquad (5.7)$$

Equating this with equation (5.6), ignoring the higher-order terms and equating powers of z we find:

$$\omega_z = \sqrt{\omega_o^2 - \frac{j(j-1)C_j}{m\Delta^{j+2}}}, \qquad (5.8)$$

$$\delta_z = \frac{jC_j}{m\omega_o^2\Delta^{j+1}} \qquad (5.9)$$

and

$$\delta U = \frac{C_j}{\Delta^j}\left(\frac{j^2 C_j}{2m\omega_o^2\Delta^{j+2}} - 1\right). \qquad (5.10)$$

Therefore, the effect of the surface can be approximated firstly by a decrease in the trap frequency, as equation (5.8) shows that $\omega_z < \omega_o$. Secondly, the perturbation will reposition the trap minimum closer to the surface, as $\delta_z > 0$ so $\Delta < \Delta + \delta_z$. Lastly, the offset, $-\delta U$, will cause the entire trap to undergo a spatially invariant potential drop, which positions the new trap minimum at $U_{tot}(z = 0) = 0$.

Figure 5.2 shows these results pictorially, with the initial trapping potential (light blue dashed line) perturbed by a graphene surface at a distance $0.275\ \mu$m from the trap centre, causing the attractive potential shown in the dashed red curve. This results in the total potential (dark blue line) which can be approximated by the new harmonic potential (dashed green line). We can see, near the trap minimum, the expansion in equation (5.6) is rather accurate as the original trap is loosened, producing the more 'open' trap. We approximate the new potential using a smaller trapping frequency and, similarly, the trap centre is shifted left, towards the surface by an amount, δ_z.
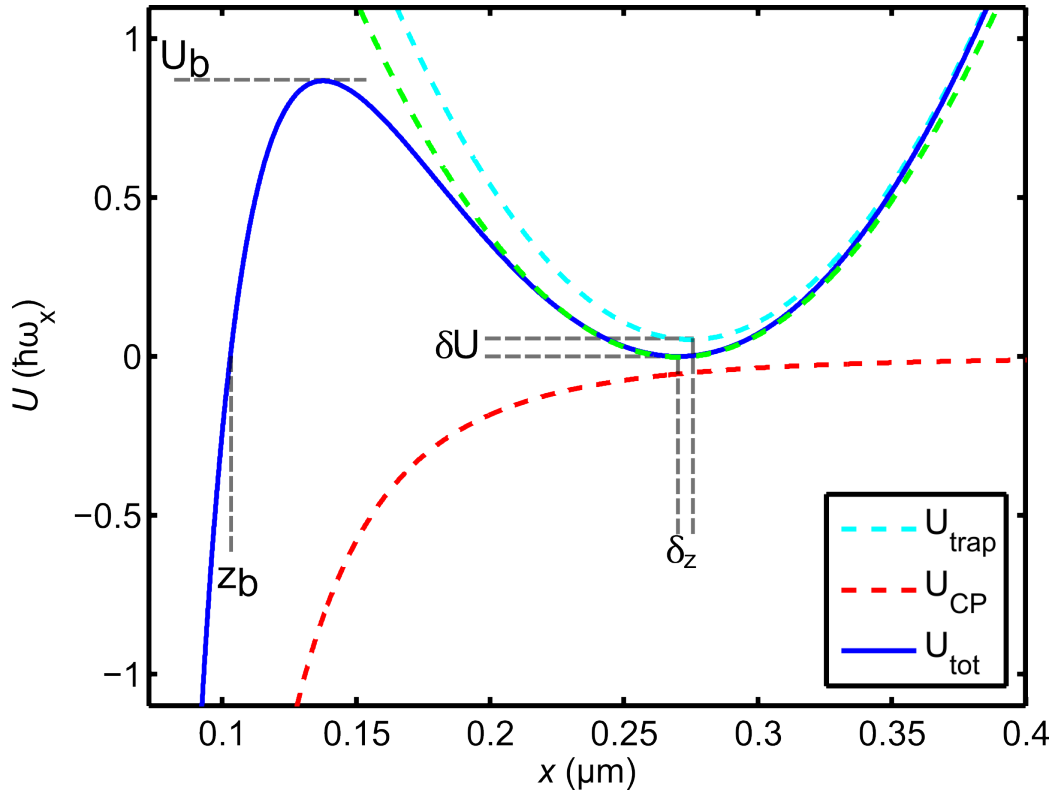
Figure 5.2: Total potential (dark blue) felt by ^{87}Rb atoms in a harmonic trap (light blue dashed) of $\omega_z = 2\pi 10$ kHz that is warped by the attraction of a graphene surface (red-dashed line) 0.275 μm away from the trap centre. U_b and z_b mark the position of the resulting barrier height and effective width (defined by the position where U $= 0$), respectively.

However, we can see large discrepancies further from the trap minimum, towards the surface. Here, the higher order terms in the expansion, i.e. terms of order z^3 and larger, become sizeable as $-z/\Delta$ approaches unity. These cause additional curvature in the trap, which results in a potential of finite height, shown by U_b in figure 5.2. The position of U_b is given by one of the roots of the (non-approximate) $(j + 2)^{th}$ order polynomial:

$$(\Delta + z)^{j+1}z + \frac{jC_j}{m\omega_o^2} = 0, \tag{5.11}$$

which can be numerically solved given the required parameters. The

value of U_b is then simply the total potential at the first real, negative, root of greater magnitude than δz.

Travelling further towards the surface, the potential drops to (the newly defined) zero, at the point z_b, which is a root of another $(j+2)^{th}$ polynomial:

$$(\Delta + z)^j z^2 - \delta z (\Delta + z)^j z + \frac{2C_j}{m\omega_o^2} \left(\frac{\Delta + z}{\Delta} \right)^j - \frac{2C_j}{m\omega_o^2} = 0. \qquad (5.12)$$

The root, z_b, will (again) be the first real, negative, root of greater magnitude than δ_z.

This creates a finite energy barrier which can be very roughly approximated by a rectangle of height U_b and width z_b. Using the standard formula for a particle of energy $E = \hbar^2 k_E^2 / 2m$ tunnelling through a square barrier, the transmission probability is given by:

$$T = \frac{1}{1 + \frac{U_b^2 \sinh^2(k_E z_b)}{4E(U_b - E)}}. \qquad (5.13)$$

Figure 5.3 shows the barrier heights and widths and resulting tunnelling probabilities for groundstate ^{87}Rb particles ($E = \hbar\omega_z/2$ so $k_E = 1/2l_z$) in traps of $\omega_z = 2\pi 20$ kHz, held $\Delta = 0.5$ μm above the three different materials of interest. The plots show that for SiN membranes, the combination of low barrier width, shown in figure 5.3a, with low barrier height, figure 5.3b, results in a greatly increased probability that atoms can escape. Conversely for graphene the large barrier width and height produces a lower tunnelling probability.

It may seem counter-intuitive that the SiN membrane would have a larger effect on a harmonic trap than the bulk substance. However, from table 5.2, we can see that for surface-trap separations:

$$\Delta < \frac{C_5}{C_4} t \approx 0.7 \mu\text{m}, \qquad (5.14)$$

the 5th order power law potential of the SiN membrane will cause a stronger attraction than the 4th order SiN bulk potential.

Although, these three plots are simple estimations, they show how the different coefficients and spatial power laws effect the ease of trapping atoms close to these substances. In order to investigate further, we must more accurately calculate the tunnelling rates and take into account additional
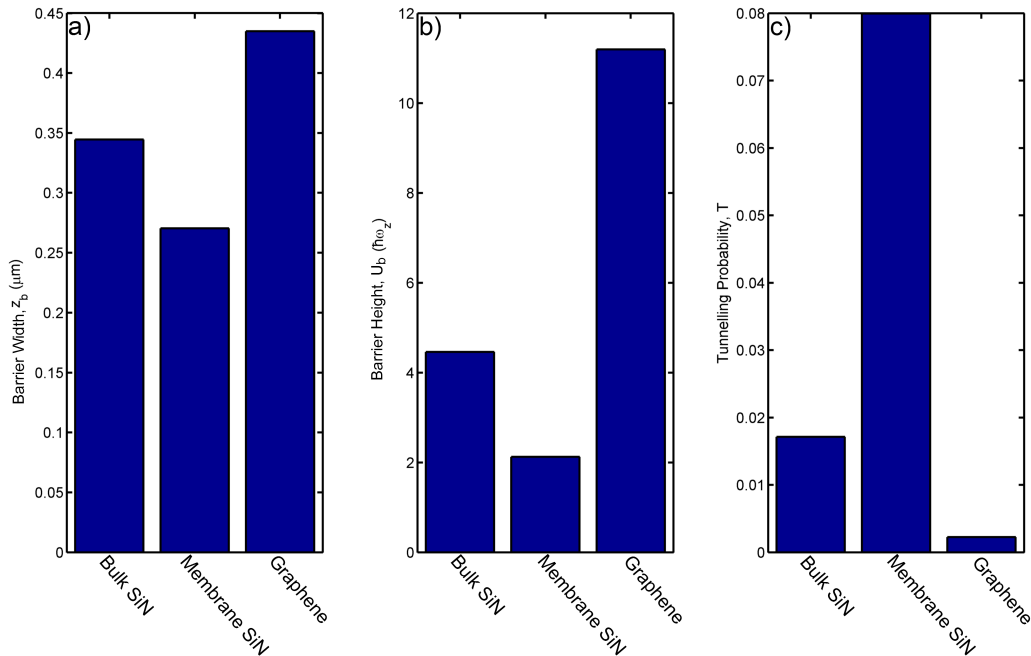
Figure 5.3: Bar graphs showing a) barrier width, b) barrier height and c) approximate tunnelling probability for a groundstate ^{87}Rb atom in an $\omega_z = 2\pi$ 20 kHz trap held $\Delta = 0.5$ μm above three different surfaces.

loss mechanisms as well as the 3D nature of the condensates that will be held above these materials.

5.3 Three-Body Losses

When discussing dynamics inside a condensate, we usually only consider low-energy binary collisions that are entirely elastic, the total kinetic energy of the atoms involved is entirely conserved during the collision. Then, so long as the depth of the trap is around twice as large as the most energetic atoms, no atoms should be lost.

However, if the density of atoms is large enough, some collisions will cause two atoms to temporarily form a molecule (also known as a dimer). The kinetic energy of the atoms is then greatly increased due to the release of the large binding energy of the molecule. To conserve both the momentum and energy of this interaction, a third atom must be involved in the collision,

which is more likely when the atom density is high. Typically, these types of collisions release large amounts of energy, allowing atoms to escape classically, even relatively deep traps, leading to atomic losses [84].

It is assumed that the energy gained from these collisions leads to the immediate loss of the atoms [85]. Therefore, the rate of loss is simply the rate of collisions multiplied by the probability of three atoms being involved in a collision of this type, which is given by the three-body correlation function. The loss rate is then:

$$\frac{dn(\mathbf{x})}{dt} = -K_3 \langle \hat{\psi}^\dagger(\mathbf{x})\hat{\psi}(\mathbf{x})\rangle^3, \tag{5.15}$$

where $K_3 = 5.8 \times 10^{-42}$ m^{6}s^{-1} is the three-body recombination rate constant for ^{87}Rb [21]. Using a semi-classical approach, and assuming the cloud is at zero temperature, this can be re-written:

$$\frac{dn_c(\mathbf{x})}{dt} = -K_3 n^3(\mathbf{x}). \tag{5.16}$$

5.4   1D Condensates

If the aspect ratio (or the ratio of the trap frequencies) is high enough and the atom number low enough, the cloud can be treated as 1D. This means that along one direction (x) the cloud is very extended and in the two transverse directions $(y$ and $z)$ the cloud is very spatially limited. This occurs if the chemical potential of the condensate fulfils the two conditions:

$$5\hbar\omega_x < \mu < \frac{3}{2}\hbar\omega_{y,z}. \tag{5.17}$$

Under these conditions the condensate can only occupy the non-interacting groundstate in the y and z directions, but is free to occupy many states in x. This produces a 'cigar' shaped condensate. We will assume that to obtain reasonable lifetimes the 'cigar' axis must be aligned parallel to the surface.

Figure 5.4 shows a schematic of the system, with the iso-density surface of a 1D condensate (red) close to a surface (blue) of bulk silicon nitride. The parameters are given in the figure caption and were chosen to give a balance of tunnelling losses and three-body losses, as described in section 5.4.4. Taking note of the axis labels, this figure shows that condensates can be held for experimentally useful lengths of time very close to a surface (less
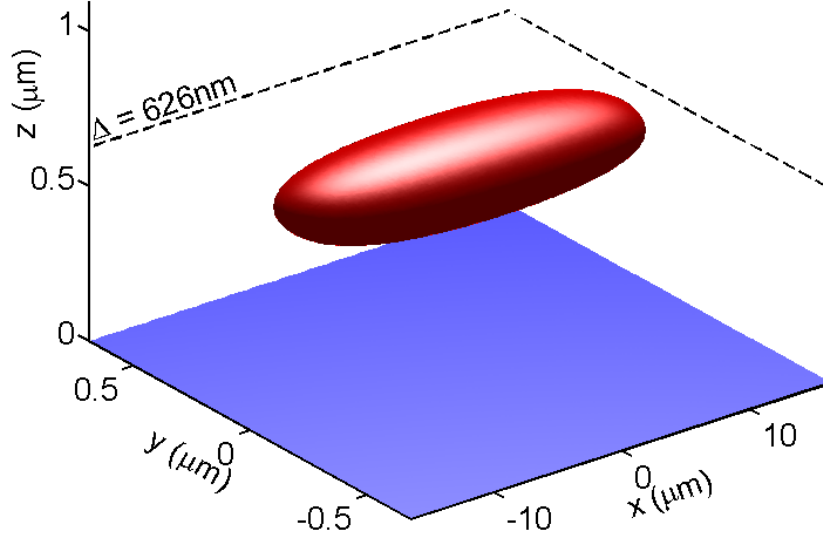
Figure 5.4:   Iso-density plot (red) of a $T = 0$, 1D ^{87}Rb condensate with trapping frequencies $\omega_{x,y,z} = 2\pi[0.2, 13.5, 56]$ kHz and $\Delta = 626$ nm above bulk silicon nitride. The parameters were chosen to give $\tau_{3B} = \tau_{tunnel} = 10$ ms.

than 1 micron) with very extreme 1D aspect ratios ($\omega_{y,z}/\omega_x \sim 150$) meaning that the surface-trap centre separation is considerably less than the length of the condensate ($2x_{TF}/\Delta \sim 30$).

To simplify our descriptions of these condensates, we can use the cylindrical symmetry substitutions:

$$\omega_r = \sqrt{\omega_y \omega_z} \tag{5.18}$$

and

$$r = \sqrt{y^2 + z^2}. \tag{5.19}$$

.

The 1D Thomas-Fermi condensate density is then given by:

$$n(x,r) = \frac{1}{g}\left(\mu - \frac{m\omega_x^2}{2}x^2\right)e^{-\frac{r^2}{l_r^2}}, \tag{5.20}$$

in the region $-x_{TF} \leq x \leq x_{TF}$, where $x_{TF} = \sqrt{2\mu/m\omega_x^2}$ and $l_r =$

$\sqrt{\hbar/m\omega_r}$. Integrating equation (5.20) radially to obtain the line density we find:

$$n_{line}(x) = 2\pi \int_0^\infty n(x,r)r\,dr = \frac{\pi l_r^2}{g}\left(\mu - \frac{m\omega_x^2}{2}x^2\right). \qquad (5.21)$$

We can then invert this to get a simple formula for the chemical potential as a function of the peak line density, $n_{line,0}$ at $x = 0$:

$$\mu = 4a_s n_{line,0}\hbar\omega_r. \qquad (5.22)$$

5.4.1   Defining A Lifetime

We define the lifetime of the condensate as the time required for the peak line density of the condensate to drop below n_{min}. The exact minimum detectable density is debatable as it depends on the resolution and sensitivity of the experimental set up. However, we will use $n_{min} = 3 \times 10^6$ m^{-1} as the minimum resolvable density [86]. We will use this definition for lifetime as it gives an absolute measurement, alternative definitions such as the half life (the time taken for half of the cloud to be lost) will only give the time-scale of the loss as opposed to a single definite value of lifetime.

The initial value of the density will, of course, depend on the total number of atoms originally trapped. However, using the inequalities in equation (5.17) it is possible to show that:

$$n_{max} = \frac{3}{8}\frac{1}{a_s} = \alpha n_{min}, \qquad (5.23)$$

where a_s is the s-wave scattering length and α is a parameter that defines the ratio of the initial peak line density to the minimum resolvable density. For ^{87}Rb we can use equations (5.17) and (5.22) to show that the maximum this can be is:

$$\alpha_{max} = \frac{3}{8a_s n_{min}}\min\left\{\sqrt{\frac{\omega_y}{\omega_z}}, \sqrt{\frac{\omega_z}{\omega_y}}\right\}. \qquad (5.24)$$

If $\omega_y = \omega_z$ then $\alpha_{max} = 23.15$, i.e. the maximum number of atoms that can be loaded into a trap in order to create a 1D condensate, produces a peak line density roughly 23 times the minimum density. In section 5.4.4, we will see that the lifetimes, counter-intuitively, are only weakly affected by the exact value of α in the limit $\alpha \gg 1$.

To make the description of the lifetimes analytically tractable, we will assume that as the condensate loses atoms it remains in the equilibrium distribution given by equation (5.20) but with a decreasing chemical potential, i.e. the cloud is always described by a radial Gaussian distribution and longitudinal Thomas-Fermi distribution.

5.4.2 Tunnelling Losses

In the near-surface trap described above, the trap can become greatly weakened by the Casimir-Polder attraction resulting in a finite trap height that can be low enough to allow both classical ($E_{atoms} > U_{barrier}$) and quantum-mechanical tunnelling losses ($E_{atoms} < U_{barrier}$). We will calculate the rate of this loss mechanism using the Gamow transmission method. This was first used to calculate the tunnelling rate of protons in alpha-decay [87], [88] and can be extended to calculate transmission probabilities through any arbitrary potential. To do this, we first calculate a spatially-varying tunnelling wavevector for the atoms, which is then used to find the transmission probability for the atoms travelling through the finite trap barrier. Due to the 1D nature of the condensate, the atoms can only be in one trap level (and so $E_{atoms} = \hbar\omega_z/2$). The tunnelling wavevector can therefore be calculated as:

$$k(z) = \frac{1}{\hbar}\sqrt{m\left(2U(z) - \hbar\omega_z\right)}, \tag{5.25}$$

where $U(z)$ is the potential in the z direction. To make $U(z)$ independent of x and y, we set $U(\{x, y\} = 0, z)$, as the peak density lies along the z axis. We can then calculate a transmission probability:

$$T = \left|\exp\left(-2\int_0^{z_b} k(z)dz\right)\right|, \tag{5.26}$$

where $z = 0$ is defined as the position of the trap minimum and z_b is the point at which $U = 0$ on the surface side of the barrier, as shown in figure 5.2. This probability can then be used to find the tunnelling loss rate:

$$\frac{dn_{tunnel}}{dt} = -\frac{T\omega_z}{2\pi}n_{line,0}. \tag{5.27}$$

The lifetime due to tunnelling loss alone is given by:

$$\tau_{tunnel} = \frac{2\pi}{T\omega_z}\log(\alpha). \tag{5.28}$$

5.4.3 Three-Body Losses

As described above, the three-body loss rate is given by:

$$\frac{dn}{dt} = -K_3 n(x,r)^3. \tag{5.29}$$

The three-body loss rate can then be calculated in terms of a line density via a similar radial integration as used earlier:

$$\frac{dn_{3B}}{dt} = -K_3 \frac{n_{line,0}^3}{3\pi^2 l_r^4}. \tag{5.30}$$

We can integrate this rate to determine the lifetime:

$$\int_{\alpha n_{min}}^{n_{min}} \frac{dn_{line}}{n_{line}^3} = -\frac{K_3}{3\pi^2 l_r^4} \int_0^{\tau_{3B}} dt, \tag{5.31}$$

which gives a lifetime due to three-body losses:

$$\tau_{3B} = \frac{3\pi^2 l_r^4}{2K_3 n_{min}^2} \left(1 - \frac{1}{\alpha^2}\right). \tag{5.32}$$

5.4.4 Total Lifetime

The lifetime of the atoms will be affected by both tunnelling and three-body loss mechanisms can be found using:

$$\frac{dn_{tot}}{dt} = \frac{dn_{tunnel}}{dt} + \frac{dn_{3B}}{dt}, \tag{5.33}$$

which can be solved to determine the lifetime due to both losses:

$$\tau_{tot} = \frac{\pi}{T\omega_z} \log\left[\frac{1 + \frac{2n_{min}^2 K3}{3\pi T \omega_z l_r^4}}{\frac{1}{\alpha^2} + \frac{2n_{min}^2 K3}{3\pi T \omega_z l_r^4}}\right], \tag{5.34}$$

which, as previously stated, is only weakly related to the initial atom density ratio α.

5.4.5 Rate of Decay of the Atom Cloud

So far, we have only considered the initial and final densities of the condensate which give a range of surface separations required to attain a specified lifetime of an atom cloud for a given trap frequency. We can, however, integrate equation (5.33) in order to obtain, firstly, the line or area density versus time and then use this to calculate how the atoms are lost through three-body collisions or tunnelling. To simplify the maths, we note that the general form of the total loss rate is:

$$\frac{dn}{dt} = -An^3 - Bn \tag{5.35}$$

where A and B can be found from equations (5.30) and (5.27) and the subscript *line* has been dropped for brevity. This total rate of loss can then be integrated to find the line density at any point in time, t:

$$n(t) = \left[\left(\frac{1}{\alpha^2 n_{min}^2} + \frac{A}{B}\right) e^{2Bt} - \frac{A}{B}\right]^{-1/2} \tag{5.36}$$

where n_o is the initial density. Using equation (5.36, we can then calculate the total density lost through both mechanisms:

$$\Delta n_{3B}(t) = \sqrt{\frac{B}{A}}(-A_1 + A_2 - A_3 + A_4) \tag{5.37}$$

and

$$\Delta n_{tunnel}(t) = \sqrt{\frac{B}{A}}(A_3 - A_4), \tag{5.38}$$

where:

$$A_1 = \left[-1 + e^{2Bt} \left(1 + \frac{B}{An_o^2} \right) \right]^{-1/2}$$

$$A_2 = \left[\frac{B}{An_o^2} \right]^{-1/2}$$

$$A_3 = \tan^{-1} \left[\sqrt{ -1 + e^{2Bt} \left(1 + \frac{B}{An_o^2} \right) } \right]$$

$$A_4 = \tan^{-1} \left[\sqrt{ \frac{B}{An_o^2} } \right] . \tag{5.39}$$

5.4.6   Results for 1D Condensates

Figure 5.5 shows colour maps of the total lifetimes given by equation (5.34). The plots show the base 10 logarithm of the total lifetimes (hotter colours show longer lifetimes) versus the trap frequency, ω_z, (which for simplicity we assume to also equal ω_y) and the effective trap centre to surface distance, Δ. We can see that all three surfaces give similar looking lifetime plots, with very large lifetimes for traps with low frequencies ($\sim 2\pi$ 10 kHz)and large atom-surface separations ($\Delta \gtrsim 0.9$ μm). Similarly, they all show very low lifetimes for all frequencies, if the traps are very close to the surface, ($\Delta \lesssim 0.2$ μm). This is primarily because the tunnelling probabilities are bounded, $0 \leq T \leq 1$, and given by high-order dependencies on Δ and ω_z. Therefore, there are large regions in parameter space for which $T \to 0$ or 1 for each surface.

Secondly, the coupling between the two loss mechanisms diminishes the differences between tunnelling losses due to the different Casimir-Polder forces for each surface. Simply put, if atoms aren't lost through tunnelling then the density stays higher and they are lost through three-body collisions instead. Therefore, bulk silicon nitride may cause a smaller Casimir-Polder attraction than membrane silicon nitride, resulting in less tunnelling losses, however this will result in larger three-body losses which will negate the difference.

However, in the region $\Delta \sim 0.4$ μm and $\omega_z \sim 2\pi$ 20 kHz there is a significant difference in the lifetimes. For these parameters, we can see that the membrane and bulk SiN surfaces behave in the same way (as $C_5^T/z \approx$
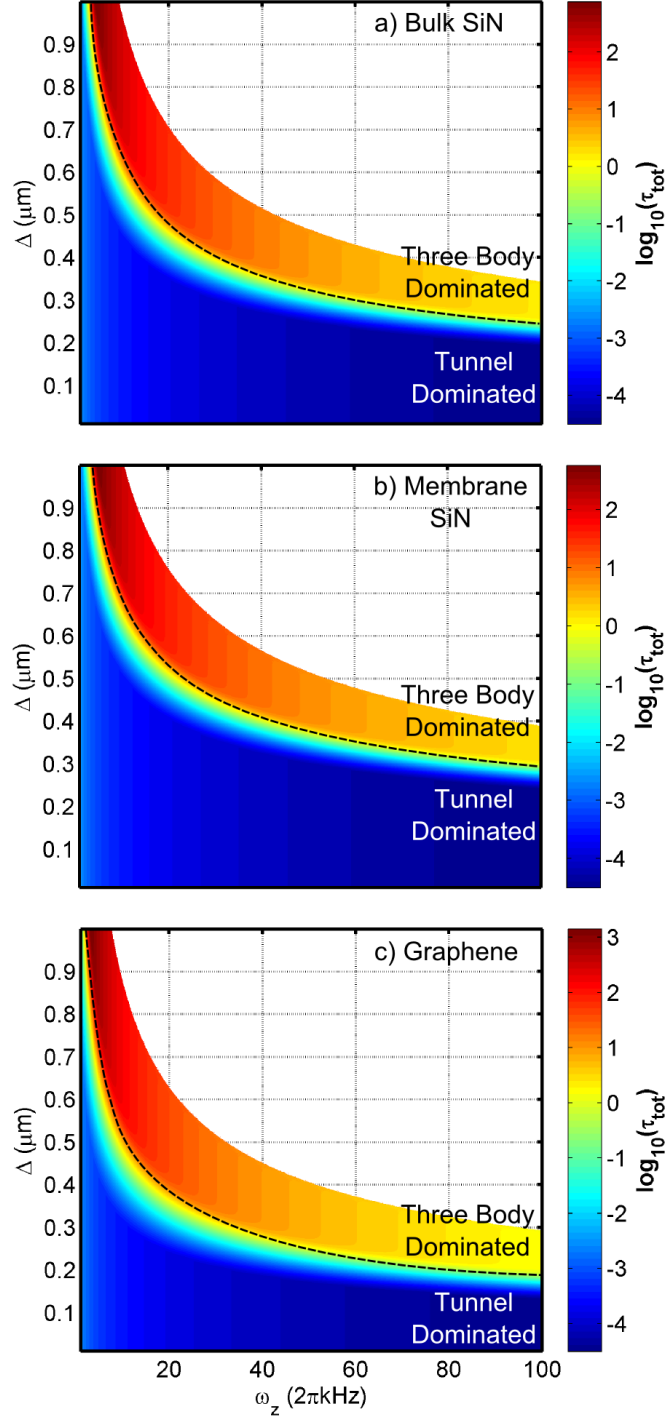
Figure 5.5: Total lifetime of a 1D ^{87}Rb condensate held at a distance Δ from a) bulk SiN, b) membrane SiN and c) graphene surfaces as given by equation (5.34). Dashed curves separate regions where three-body or surface tunnelling dominates the loss (as labelled). White regions in the top right-hand corner are due to $T \approx 0$ and $\tau_{tot} \to \infty$.
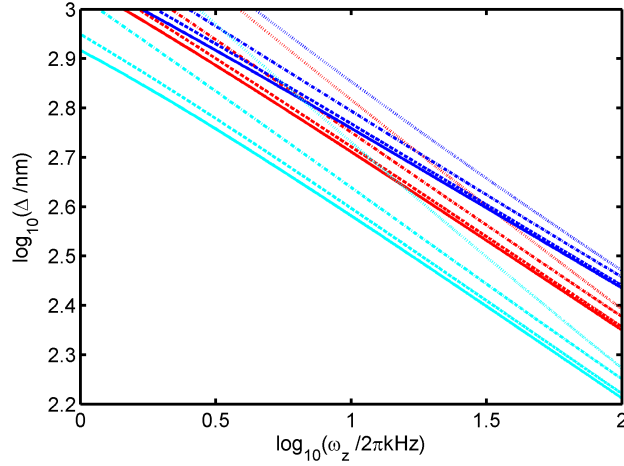
Figure 5.6: Log-log plot of constant lifetimes for a 1D ^{87}Rb condensate held above a graphene (light blue), SiN membrane (dark blue) and bulk SiN (red) surface. The lines are plotted for total lifetimes of 5 ms (solid lines), 10 ms (dashed lines), 100 ms (dash dot lines) and equal three body and tunnelling losses (dotted line).

C_4). However, the stronger Δ dependence causes greater losses above the membrane as the barrier widths, z_b, are thinner and the attraction is more sensitive to changes in Δ. Conversely, the graphene surface produces a much smaller Casimir-Polder potential in this region ($20 - 40 \times C_{4.238}/z^{0.238} \approx C_4$), which allows for much smaller surface separations than either SiN surface. Also, due to its smaller power law relationship, the lifetimes above graphene decrease slower with decreasing Δ.

We can see clearer differences if we compare the lines of constant lifetimes, i.e. points in this parameter space described by the surface-trap separation required for each trap frequency in order to produce a given total lifetime. The log-log plot of figure (5.6) shows the total lifetimes of 5 ms (solid lines), 10 ms (dashed lines), 100 ms (dash dot lines) and equal three body and tunnelling losses (dotted line) for a ^{87}Rb cloud held above a graphene (light blue), SiN membrane (dark blue) and bulk SiN (red) surface.

On this scale we can see more clearly that graphene surfaces allow for much closer trapping to a surface and SiN membranes require larger atom-surface separations than bulk SiN to attain these lifetimes. All of these effects are greatly increased for higher ω_z and smaller surface-trap distances
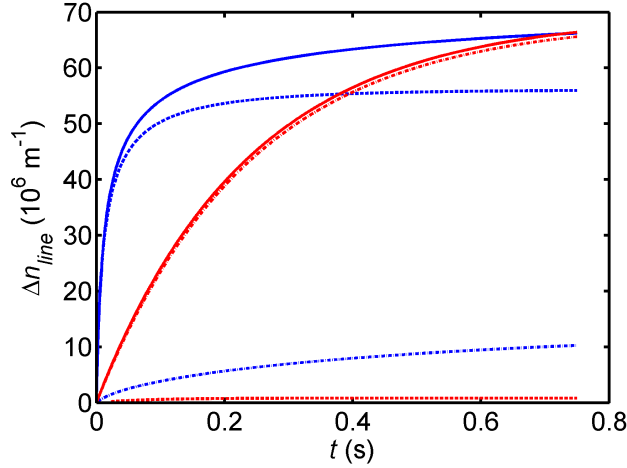
Figure 5.7: Total (solid lines), 3 body (dot dashed lines) and tunnelling (dashed lines) losses for a tunnelling loss dominated trap (red, $\omega_z = 2\pi$ 3 kHz and $\Delta = 1$ μm) and 3 body loss dominated trap (blue, $\omega_z = 2\pi$ 70 kHz and $\Delta = 0.33$ μm) above a SiN membrane, both of which have a lifetime of 750 ms.

and the lifetimes for all surfaces diverge entirely for $\omega_z > 2\pi 40$ kHz and $\Delta < 400$ nm. This divergence indicates the parameter region required for accurate measurement of comparative Casimir-Polder surface interactions.

Lastly, figure 5.7 shows the change in line density due to three-body losses (dot dashed lines) and tunnelling losses (dashed lines) when tunnelling losses dominate (red) due to a low trap frequency, $\omega_z = 2\pi$ 3 kHz, situated far from the surface $\Delta = 1$ μm. This is compared with a trap that is dominated by three-body losses (blue), with tight trapping frequency $\omega_z = 2\pi$ 70 kHz close to the surface, $\Delta = 0.33$ μm. Both of which are above a SiN membrane and have a lifetime of 750 ms.

This figure shows that although the two traps have identical lifetimes, the nature of the loss for both traps is very different. The three-body losses cause atoms to be lost rapidly: in figure 5.7, 80% of the tightly trapped atoms are lost in the first 100 ms. This is because the rate of loss is proportional to a higher power of the line density than tunnelling losses. Therefore, traps that are three-body loss dominated aren't favourable as too many atoms are lost before any atom-surface interaction has taken place. Due to the numerical nature of our evaluation of the tunnelling rate T it is not possible

71

to *a priori* define a set of trapping parameters that will be dominated by one loss mechanism or the other. Whilst figure 5.5 allows us to note in general that large frequency, large surface-separation, traps will be three-body loss dominated and, conversely, low frequency, small surface separation, traps will be tunnelling loss dominated, for more quantative analysis we have to use equations (5.37) and (5.38) for any given trap parameters.

5.5 2D Condensates

We now consider harmonic traps that fulfil the conditions:

$$5\hbar\omega_{x,y} < \mu < \frac{3}{2}\hbar\omega_z. \tag{5.40}$$

This produces a so called 'pancake' shaped condensate, whose plane is parallel to the surface.
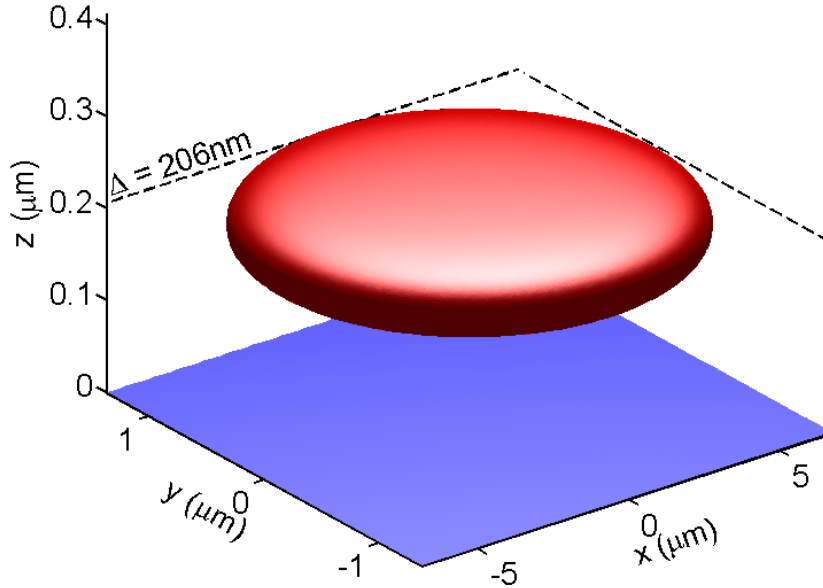
Figure 5.8: Iso-density plot (red) of a $T = 0$, 2D ^{87}Rb condensate with trapping frequencies $\omega_{x,y,z} = 2\pi[0.78, 3.87, 1205]$ kHz, $\Delta = 626$ nm above bulk silicon nitride (blue). The parameters were chosen to give $\tau_{3B} = \tau_{tunnel} = 10$ ms.

Figure 5.8 shows a schematic of the system, showing the iso-density of a 2D condensate (red) close to a surface (blue) of bulk silicon nitride. As earlier, the parameters were chosen to give a balance of tunnelling losses and three-body losses, which for a 2D condensate will be described in section 5.6. As for the 1D condensate, the surface separation is much smaller than the size of the condensate $(2x_{TF}/\Delta \sim 50)$. However, due to the more relaxed requirements on the trapping frequencies, we are able to trap much closer $(\Delta_{1D}/\Delta_{2D} \sim 3)$, for the same lifetimes.

Using similar techniques as before, we use the Thomas-Fermi density:

$$n(x, y, z) = \frac{1}{g}\left(\mu - \frac{m\omega_x^2}{2}x^2 - \frac{m\omega_y^2}{2}y^2\right)e^{-\frac{z^2}{l_z^2}} \tag{5.41}$$

to find the line density

$$n_{line}(x) = 4\int_0^{y_{TF}}\int_0^\infty n(x, y, z)dzdy$$

$$= \frac{\sqrt{\pi}m\omega_y^2 l_z}{g}\left(\frac{2}{3}\sqrt{\frac{2\mu}{m\omega_y^2}} - \frac{\omega_x^2}{\omega_y^2}x^2\right). \tag{5.42}$$

The peak line density is then:

$$n_{line}(x = 0) = n_{line,0} = \frac{\omega_z}{3a_s\omega_y}\sqrt{\frac{2}{\pi}}\left(\frac{\mu}{\hbar\omega_z}\right)^{3/2}. \tag{5.43}$$

The limits on the initial density can then be found, as earlier, by setting:

$$\mu = \left(\frac{3a_s n_{line,0}\omega_y}{\omega_z}\sqrt{\frac{\pi}{2}}\right)^{2/3}\hbar\omega_z, \tag{5.44}$$

which gives:

$$\alpha_{max} = 0.168\frac{\omega_z}{\omega_y}. \tag{5.45}$$

5.5.1 Three-Body Losses

We can use exactly the same method given above to calculate the three-body losses:

$$\frac{dn_{3B}}{dt} = -\frac{\pi K_3}{530\sqrt{3}l_z^4 a_s^{2/3}} \left(\frac{6n_{line,0}}{\pi}\right)^{7/3} \left(\frac{\omega_y}{\omega_z}\right)^{4/3} \tag{5.46}$$

and the corresponding lifetime:

$$\tau_{3B} = \frac{420\sqrt{3}l_z^4 a_s^{2/3}}{\pi K_3} \left(\frac{\pi}{6}\right)^{7/3} \left(\frac{\omega_z}{n_{min}\omega_y}\right)^{4/3} \left(1 - \frac{1}{\alpha^{4/3}}\right). \tag{5.47}$$

5.5.2 Tunnelling Losses

These are identical to the 1D tunnelling losses, as we are still assuming that all atoms are in the non-interacting groundstate in the z direction and so equations (5.27) and (5.28) will also be valid for a 2D condensate.

5.5.3 Total Lifetime

We can use the same general addition of the loss rates as equation (5.33) to find the total lifetime for a 2D condensate:

$$\tau_{tot} = \frac{3\pi}{2T\omega_z} \log \left[\frac{1 + \frac{K_3}{280\sqrt{3}Tl_z^4}\left(\frac{6^7\omega_y^4 n_{min}^4}{\pi a_s^2 \omega_z^7}\right)^{1/3}}{\frac{1}{\alpha^{4/3}} + \frac{K_3}{280\sqrt{3}Tl_z^4}\left(\frac{6^7\omega_y^4 n_{min}^4}{\pi a_s^2 \omega_z^7}\right)^{1/3}}\right]. \tag{5.48}$$

5.6 Area Density Lifetimes of 2D Traps

The line density relations given above require both ω_y and ω_z to be useful and, using an approximate form of the total lifetime:

$$\tau_{tot} \approx \frac{3\pi}{2T\omega_z} \log \left[\frac{280\sqrt{3}Tl_z^4}{K_3}\left(\frac{\pi a_s^2 \omega_z^7}{6^7\omega_y^4 n_{min}^4}\right)^{1/3}\right], \tag{5.49}$$

we can see that the lifetimes will be increased by increasing ω_z and decreasing ω_y. Physically, this can be explained by the need to increase the frequency in the surface direction to lessen tunnelling losses, whilst attempting to lower all other frequencies to keep the density and three-body losses to a minimum.

This makes the loss rate a 3D parameter (ω_y, ω_z and Δ) problem. However, we can reduce this back to 2 parameters by considering the peak *area* density, given by:

$$n_{area,0} = 2 \int_0^\infty n(\{x, y\} = 0, z) dz = \frac{1}{4\sqrt{\pi} a_s l_z} \frac{\mu}{\hbar \omega_z}. \tag{5.50}$$

We then define the lifetime by using the minimum resolvable area density, $n_{min,area} = n_{min}^2 = 9 \times 10^{12} \text{ m}^{-2}$ and $\alpha = n_{area,0}/n_{min}^2$. Using the area density and the right hand side of condition (5.17) we find:

$$\alpha_{max} = 6.1852\sqrt{\omega_z}. \tag{5.51}$$

Analogous three-body loss rates and lifetimes are given by:

$$\frac{dn_{3B}}{dt} = -\frac{K_3 n_{area,0}^3}{\sqrt{3}\pi l_z^2} \tag{5.52}$$

and

$$\tau_{3B} = \frac{\sqrt{3}\pi l_z^2}{2K_3 n_{min}^4} \left(1 - \frac{1}{\alpha^2}\right). \tag{5.53}$$

The tunnelling loss rates and lifetimes are, as always:

$$\frac{dn_{tunnel}}{dt} = -\frac{T\omega_z}{2\pi} n_{area,0} \tag{5.54}$$

and

$$\tau_{tunnel} = \frac{2\pi}{T\omega_z} \log(\alpha). \tag{5.55}$$

Combining the two loss rates, we can obtain a total lifetime:

$$\tau_{tot} = \frac{\pi}{T\omega_z} \log \left(\frac{1 + \frac{2K_3 n_{min}^4}{\sqrt{3}T\omega_z l_z^2}}{\frac{1}{\alpha^2} + \frac{2K_3 n_{min}^4}{\sqrt{3}T\omega_z l_z^2}} \right). \tag{5.56}$$

In this case, the lifetimes are defined by a single frequency, ω_z, and the surface-trap separation, Δ, via the transmission probability T.

The area density will decrease in time in the same manner as the 1D line density, given in equations (5.36,5.37,5.38), with A and B taken from the area density three-body (5.52) and tunnelling (5.54) loss rates, respectively.

5.6.1 Results for 2D Condensates

Figure 5.9 shows the total lifetime of a 2D, $T = 0$, cloud of ^{87}Rb atoms held above a) bulk SiN, b) a SiN membrane and c) graphene for varying trap frequencies, ω_z, and trap-surface separations, Δ. As we previously found for 1D clouds, holding atoms above the three surfaces generally gives the same results because the coupling of the two loss mechanisms acts to diminish the difference in the atom-surface attractions. In 2D, this effect appears to be increased, as now the lifetimes above all three surfaces look relatively similar (note the now identical colourbars in figure 5.9). However, the qualitative relationships found earlier still appear to hold, with bulk SiN causing less atom loss than the membrane, whilst graphene allows the longest lifetimes.

Figure 5.9 also shows that, for a given trap frequency and atom-surface separation, higher lifetimes can be achieved using 2D rather than 1D condensates. This is especially apparent for higher trap frequencies, as figure 5.9 shows a much slower decrease in lifetime at higher trap frequencies for all surfaces.

As seen for the 1D condensate, the differences between surfaces are made clearer if we compare the loci of constant lifetimes. The log-log plot in figure 5.10 shows the total lifetimes of 5 ms (solid lines), 10 ms (dashed lines), 100 ms (dash dot lines) and equal three body and tunnelling losses (dotted line) for an ^{87}Rb cloud held above a graphene (light blue), SiN membrane (dark blue) and bulk SiN (red) surface.

Figure 5.10 shows that the divergence for the three surfaces appears more gradually and at larger trap frequencies ($\omega_z > 2\pi60$ kHz) and smaller separations ($\Delta < 320$ nm) than the region required for the 1D condensate, as shown in figure 5.6. This would make it harder to investigate comparative Casimir-Polder surface interactions in this configuration.

5.7 3D Condensates

If the conditions in equation (5.17) can't be upheld then we must use a fully 3D condensate. This comes with the requirement that:

$$5\hbar\omega_{x,y,z} \lesssim \mu. \tag{5.57}$$

Anything in between the conditions in (5.17) and (5.57) can be thought of as quasi-1D and the lifetimes can only be accurately calculated using more
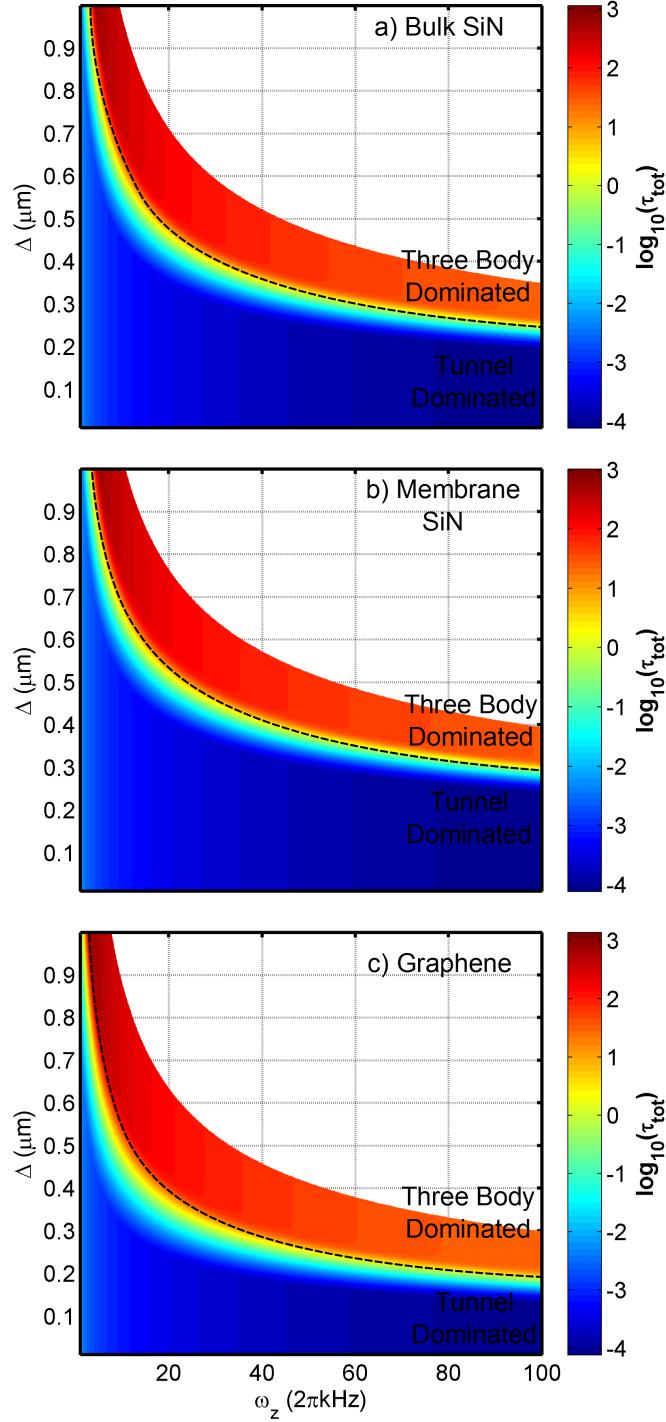
Figure 5.9: Total lifetime of a 2D ^{87}Rb condensate in a harmonic trap held at a distance Δ above a) bulk SiN, b) membrane SiN and c) graphene surfaces. Dashed curves separate regions where three-body or surface tunnelling dominates the loss (as labelled). White regions in the top right-hand corner are due to $T \approx 0$ and $\tau_{tot} \to \infty$.
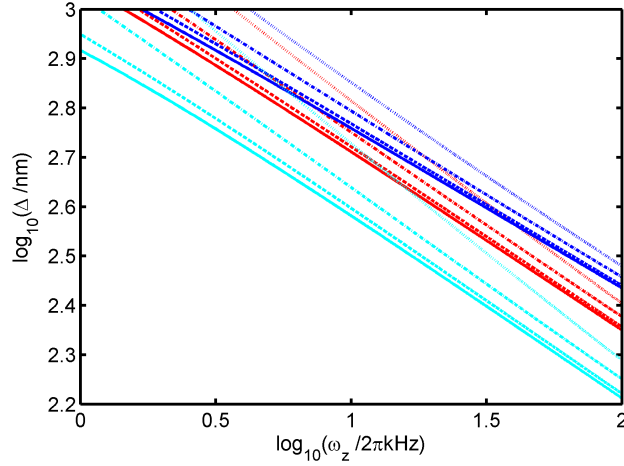
Figure 5.10: Log-log plot of constant lifetimes for a 2D ^{87}Rb condensate held above a graphene (light blue), SiN membrane (dark blue) and bulk SiN (red) surface. The curves are plotted for total lifetimes of 5ms (solid lines), 10ms (dashed lines), 100ms (dash dot lines) and equal three body and tunnelling losses (dotted line).

numerical means.

Whilst three-body losses can be calculated in a very similar manner to the 1D condensate, the rate at which atoms are lost through tunnelling is greatly complicated for a 3D condensate. This is because the energy available for the particles to tunnel through the barrier is now a function of the chemical potential, meaning that the transmission probability T will be a function of the line or area density. Therefore, the only accurate method of calculating the lifetime will be entirely numerical.

Lastly, in order for the 3D condition given above to be fulfilled, either all the trapping frequencies, including ω_z, must be very low, producing exponentially large tunnelling losses, or the initial chemical potential must be very large. However, as the condensate depletes, depending on the frequency ratios ω_x/ω_z and ω_y/ω_z the condensate will almost certainly alter from 3D to 2D to 1D and so any analytical 3D lifetime will not be accurate for longer times.

5.8 Conclusion

In this chapter we have seen that atoms can be held for long times ($\tau_{tot} \gg \tau_z$) above different surfaces. Large, but realistic, trapping frequencies are needed to overcome the Casimir-Polder attraction between the neutral atoms in the cold cloud and those in the surface. However, the high resulting condensate densities cause three-body recombination losses, which have to be balanced with surface losses to find optimum parameter ranges for the trap frequencies and surface-trap centre separations.

The results we have produced (primarily figures 5.5 and 5.9) are in good quantitative agreement with previous experimental findings, [72, 74]. However, we have been able to expand this knowledge over a much larger parameter range in order to show the trap frequencies and condensate dimensionality required for much decreased atom-surface separations. Whilst other additional parameters (atom species, atom state and additional electric and magnetic fields) could be used to alter these results, we have shown that the intrinsic interaction in a typical BEC experiment can be overcome.

Chapter 6

Coupling of a BEC to an Oscillating Cantilever

6.1 Introduction

The coupling discussed in the previous chapter, dealt with atoms interacting with a stationary surface. The only motion was atoms leaving the trap due to both three-body losses and surface attraction overcoming the trapping potential. In this chapter, we will investigate the effects of an oscillating surface coupled to a harmonically trapped cloud of atoms.

Micro-mechanical and nano-mechanical oscillators have been created with mechanical properties that can be observed to a high degree of accuracy, primarily in terms of oscillation amplitude and frequency. These have been shown in a multitude of experiments [89–91].

The following investigation is based on an experiment carried out in which a harmonically-trapped BEC was coupled to an oscillating SiN cantilever via the Casimir-Polder attraction explained in chapter 5, [70]. In the experiment, the condensate was first moved close to the un-driven cantilever and the atom loss rate was measured. The results were quantitatively similar to the results given in the previous chapter. Secondly, using a piezoelectric crystal, the cantilever was driven to oscillation. By changing the trap frequency of the atoms, the experimentalists showed a broad range of excitations by studying the amount of atoms lost from the trap.

6.1.1 Perpendicular Driving and Atom Loss

Perpendicular Experimental Set Up
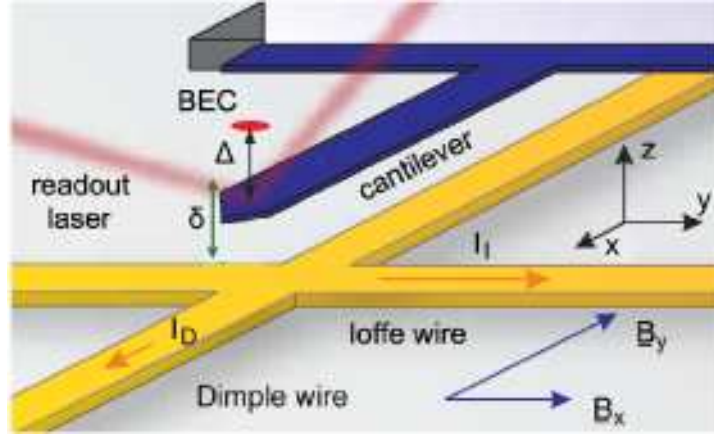
Figure 6.1: Experimental set up (adapted from [70]) showing the wires (yellow) required to make the harmonic trap which held a cloud of ^{87}Rb atoms (red) a distance, Δ, above the cantilever (blue).

Figure 6.1 shows a schematic of the physical arrangement for the experiment mentioned above. The atoms (red) are placed in a harmonic trap with, typically, $\omega_{x,y,z} = 2\pi[10.4, 0.8, 10.5]$ kHz, though as explained ω_z is changed to cover a range of frequencies. This trap can be held at varying distance Δ from the SiN cantilever (blue), which is driven into resonant excitation in the z direction with a frequency of $\omega_c = 2\pi$ 10 kHz and a typical amplitude of $\delta = 120$ nm. The figure also shows the wire structure (yellow) and currents (I_D and I_I) which, along with B_y and B_x (blue) the components of the additional homogeneous bias field, are required to create the trap magnetic field. The faint red lines show the path of the readout laser used to measure the magnitude of oscillation of the cantilever.

We will call this arrangement the "perpendicular" set up as the condensate motion is excited in the z direction, perpendicular to the $x - y$ plane of the cantilever. In order to create a simple model of this excitation, we will make the following assumptions: the atoms are weakly driven, so $\Delta \gg \delta$, and the driving potential is constant over the expanse of the cloud in x and y.

Then the Casimir-Polder potential can be described by:

$$U_{CP}(z,t) = -\frac{C_4}{[\Delta + z + \delta \cos(\omega_c t)]^4}, \tag{6.1}$$

where we have used the same 4th order power law as shown in table 5.2. This can then be expanded in the same manner as section 5.2.1 to give a total potential in z:

$$U_{tot} = \frac{m\omega_z^2 z^2}{2} - 20\frac{C_4}{\Delta^6}z\delta \cos(\omega_c t), \tag{6.2}$$

where ω_z is the final, effective, trapping potential created by an initial, tighter trap that is weakened and shifted by the surface attraction. This approximation requires that we use the 2nd order terms in the expansion around $(z + \delta \cos(\omega_c t))/\Delta = 0$ in order to couple the time dependent oscillation with the z position. Even so, the interaction between the condensate and the cantilever is linear in $\delta \cos(\omega_c t)$, which will allow the equations of motion to be solved analytically. Lastly, in this linear driving regime, the force due to the oscillating cantilever will be entirely resonant with ω_c. If more terms were required in the expansion in equation (6.2) then $2, 3, 4... \times \omega_c$ terms would enter into the dynamics.

Surface Adsorbates

In the previous experiment [70], the atoms were first moved towards an undriven ($\delta \approx 0$) cantilever. The results revealed losses from the trap for any surface-trap separation < 1 μm and complete loss for $\Delta \lesssim 0.5$ μm. This agrees quantitatively with the results given in the previous chapter (section 5.4.6) for a 1D condensate held in an $\omega_z = 2\pi$ 10 kHz trap above bulk SiN, as shown in figure 5.5a.

Next, the experimentalists used a piezoelectric crystal to resonantly excite motion in the cantilever. Then, by changing the atoms' trap frequency, resonant and non-resonant motion was excited. In order to quantify the level of excitation, the experimentalists simply observed a qualitative comparison of atom losses from the trap for the different frequencies. However, as they note in their investigation, whilst carrying out this experiment, many of the atoms lost from the trap will have been deposited onto the cantilever. This is an issue as the Casimir-Polder interaction is greatly effected by such contamination [92]. From their data, the experimentalists extrapolated that the layering of the ^{87}Rb atoms on the cantilever resulted in a 200($\pm$100)

times increase in the strength of the Casimir-Polder attraction. However, this was calculated from a relatively simple loss model, which did not take into account the excitation explicitly.
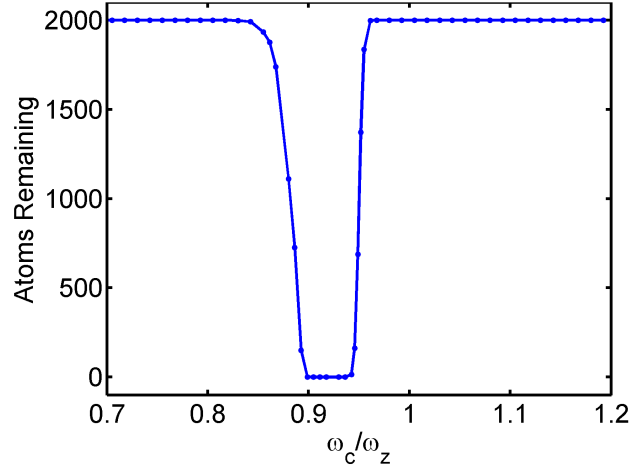
Figure 6.2: Atoms remaining in traps of varying perpendicular frequency ω_z after 20 ms of excitation from a cantilever driven to oscillate with $\delta = 120$ nm and $\Delta = 1.6$ μm. $C_4^{eff} = 200C_4$ to account for the cantilevers surface contamination.

Figure 6.2 shows the results of a full PGPE simulation in which we calculated the number of atoms remaining in traps of different perpendicular frequency, ω_z, after they have been excited for 20 ms with a cantilever oscillating with $\delta = 120$ nm at a distance $\Delta = 1.6$ μm and a fixed cantilever frequency 2π 10 kHz. To increase the accuracy of the results, the non-approximate form of the Casimir-Polder potential, given in equation (6.1), was used and an increased C_4 value was calculated in order to simulate the effect of the metal coatings placed on the cantilever [70]. To account for the surface contamination, $C_4^{eff} = 200C_4$ was also used to determine the surface potential.

The results in figure 6.2 show that there is a wide range of frequencies, $0.85 < \omega_c/\omega_z < 0.96$, that will cause the atoms to be excited out of the trap. This is due to the large Casimir-Polder surface potential, which causes a substantial distortion of the trap potential: an effect that increases as the cantilever moves towards the surface as it oscillates. It can be shown using equations (5.8) and (5.12) that this causes an initially resonant trap,

to have an effective frequency which varies around $0.85 < \omega_c/\omega_z < 0.97$ as the cantilever oscillates. This frequency regime is exactly where the atom loss occurs in figure 6.2.

The results from the previous experiment do not show this resonant frequency broadening, instead only a thin peak is seen around $0.98 > \omega_c/\omega_z > 1.02$. This indicates that the simple model used by the authors of [70] was not sufficient to account for the excitation of the atoms and/or that surface contaminants play a large role in altering the Casimir-Polder potential. However, they also indicate that increased atom losses and stronger surface attraction causes greater uncertainty in the position of the trap which, as previously indicated, can have a large effect on atom loss. Therefore, a systematic overestimation of Δ, as well as an increased surface attraction, could be a better candidate to explain the experimental results.

In order to model the excitation and loss of atoms in an interacting system that is not described by a 1D condensate, we used an imaginary potential. This acted to rapidly diminish the mean-field wavefunction in the region $z < 2z_b$. This method of atom loss has been previously used with great success and appears to give reasonable results that don't alter with small variations to the imaginary potential depth or position [83, 93].

6.2   Thermal Cantilever Oscillation

A primary objective in the coupling of micro-mechanical devices to cold atoms is to carry out state manipulation and readout between the two very different systems. However, there is a large issue with coupling these together. Atoms can be effectively isolated from their environments and cooled to temperatures low enough to cause macroscopic occupation of the groundstate (i.e. Bose-Einstein condensation). Conversely, micro-mechanical structures cannot be so effectively isolated from their environments, and due to their much larger size, the typical energy scale at thermal equilibrium is prohibitively large when trying to cool them to degeneracy. There has been some success in cooling and manipulating these sizeable structures [94–96]. Typically, however, the experiments are carried out on smaller nano-scale devices and require the structures to contain electronic devices and other complicated mechanisms, unlike the solid SiN cantilever used in this investigation.

In the following section, we consider how thermal oscillation of the cantilever can excite motion in resonantly-coupled trapped atoms. Firstly, by

investigating the perpendicular experimental system described in the previous section, and then by suggesting a different approach that builds on the stochastic motion discussed in chapter 3.

Equations of Motion

For the following investigation, we consider a classical set of non-interacting ($g = 0$) particles, initially at rest at the centre of the effective trap. These will be driven by a cantilever that is in thermal equilibrium with its environment, which has previously been shown to be well described by the classical equation of motion:

$$\ddot{z}_c = -\omega_c^2 z_c - \gamma_d \dot{z}_c + \frac{F_{th}}{M_{eff}} \tag{6.3}$$

and:

$$\dot{z}_c = \frac{p_c}{M_{eff}}, \tag{6.4}$$

where z_c is the position of the tip of the cantilever, γ_d is the damping coefficient for the system, F_{th} is thermal excitation due to the environment and M_{eff} is the effective mass of the cantilever. There are many derivations of these equations of motion, mostly concerned with creating accurate models for scanning tunnelling microscopy [97–99]. However only the key results will be given here.

The effective mass of the cantilever can be found by halving the usual relation for the unsupported total mass:

$$M_{eff} = \frac{1}{2}\rho L_x L_y L_z. \tag{6.5}$$

The damping co-efficient is given by:

$$\gamma_d = \frac{k_B T}{\hbar Q}, \tag{6.6}$$

and the thermal noise is defined by a power spectral density given by:

$$F_{th}^2 = 4k_B T \gamma_d M_{eff}, \tag{6.7}$$

where Q is the quality factor of the cantilever and accounts for the effects of the environment, which is treated as an infinite thermal bath at temperature T.

The equations of motion can then be solved to yield:

$$z_c = \delta_{th} \sin(\omega_c t), \tag{6.8}$$

where the thermal oscillation amplitude is given by:

$$\delta_{th} = \sqrt{\frac{k_B T}{M_{eff} \omega_c^2}}. \tag{6.9}$$

For the cantilever used in the perpendicular experiment [70] which has $M_{eff} = 5$ ng, $\omega_c = 2\pi\, 10$ kHz, $T = 300$ K and $\delta_{th} = 133.8$ pm. This is substantially less than the 120 nm driven oscillation amplitude and so it isn't immediately obvious that it will cause any great excitation in the trapped atoms. To calculate the effects of the cantilever analytically, we can, using the potential given in equation (6.2), create the equations of motion for the atoms:

$$\ddot{z} = -\omega_z^2 z + \frac{F_o}{m} \cos(\omega_z t) \tag{6.10}$$

and:

$$\dot{z} = \frac{p_z}{m}, \tag{6.11}$$

where the force constant is given by:

$$F_o = 20 \frac{C_4}{\Delta^6} \delta. \tag{6.12}$$

.

It is straightforward to show that the equations of motion are solved by:

$$z = \frac{F_o t}{2m\omega_z} \sin(\omega_z t). \tag{6.13}$$

From this, the energy of the atoms is given by:

$$\begin{aligned}
E_a(t) &= \frac{m\omega_z^2}{2} z^2 + \frac{p_z^2}{2m} - F_o z \cos(\omega_z t) \\
&= 50 \frac{C_4^2 \delta^2}{m\Delta^{12}} \left[t^2 - 2\frac{t}{\omega_z} \cos(\omega_z t) \sin(\omega_z t) + \frac{\sin^2(\omega_z t)}{\omega_z^2} \right].
\end{aligned} \tag{6.14}$$

86

The prefactor in equation (6.14) shows that the key parameter in the atom-cantilever coupling is the trap-surface separation, due to the high power law relationship. Therefore, in order to obtain similar results for both the driven and thermal cantilever, the cantilever-trap separation must satisfy:

$$\Delta_{th} \approx \Delta_{dr} \left(\delta_{th}/\delta_{dr} \right)^{1/6}, \tag{6.15}$$

where the subscripts th and dr denote the thermal and driven parameters respectively. Using the values given above, this would require a trap surface separation of $\Delta_{th} = 331$ nm, a little over 20% of the driven value. Whilst this separation is not entirely prohibitive, the results in the previous section show that it would cause significant atom losses due to tunnelling, which will be greatly increased by the excitation of the atom cloud.

Therefore a balance must be struck which allows the atoms to be held close enough to the cantilever to allow as much heating as possible without too much atomic loss. To quantify this balance, we will calculate the total energy of the atom cloud, taking into account a time-dependent number of atoms:

$$E_{tot} = N(t)E_a(t). \tag{6.16}$$

The number of atoms remaining at time, t, can be calculated using a similar method as equation(5.27):

$$N(t) = N_o \exp\left[-2\pi\omega_x \int_0^t T[E_a(t')]dt' \right], \tag{6.17}$$

where $N_o = 2,000$ is the initial number of atoms used in the experiment and we have now used a continuum approach to loss for atoms of energy E_a rather than assuming they are in the groundstate or any quantised harmonic oscillator level. The atomic loss due to a finite barrier also requires that we implement an upper bound on E_a, as the trap potential (shown in figure 5.2) is very anharmonic as it approaches the barrier height U_b, which means that any atoms excited to U_b will simultaneously be short lived and anharmonic. This requires that $\max[E_a(\Delta)]_t \leq U_b(\Delta)$. We will also assume that three-body losses are negligible as the atom density used in the experiment was relatively low and so few atoms would be lost in this manner.

To quantify the level of coupling between cantilever and the atom cloud, we will use the average power transferred between the cantilever and the atoms:

$$P(t) = N(t)\frac{E_a(t)}{t}. \tag{6.18}$$

For strong coupling, we require that the energy transferred between the atoms and the cantilever is larger than the energy transferred to the cantilever from its surroundings. It is in this regime that state manipulation, transfer and readout can be carried out on the cantilever, as the energy in the system will be entirely dictated by the initial conditions of the cantilever and atoms without incoherent noise destroying any information we wish to exchange with the cantilever.

From the thermal damping relation given in equation (6.6), we can see that the energy lost from the cantilever, over one oscillation period, at equilibrium, must be:

$$E_{damp} = -\frac{k_B T}{Q}. \tag{6.19}$$

Therefore, in order to continue oscillating with the same amplitude, the thermal bath of phonons present in the large coupled support structure, used to hold the cantilever in place, must equal this loss. Therefore, the average thermal power is given by:

$$P_{th} = \frac{k_B T \omega_c}{2\pi Q}. \tag{6.20}$$

For the cantilever used in the above experiment, $P_{th} = 1.92 \times 10^5 \hbar\omega_z/\tau_z$. This unit system shows that 1.29×10^5 phonons, of average energy $\hbar\omega_z$, enter the cantilever every oscillation period, τ_z.

Figure 6.3 shows the results of using equations (6.14) and (6.18) to calculate the average power transferred from the cantilever to the trapped atoms versus time and for a range of surface-trap centre distances. The atoms are given initial energies of $\hbar\omega_z/2$ to replicate the QHO groundstate and the trap geometries are as above. With varying atom-cantilever separation, there are three distinct regions separated by the white dashed lines. Firstly, when $\Delta < 0.45$, μm the surface attraction destroys the trapping potential entirely and so the atoms immediately leave the trap before any heating can take place. The second region, $0.45\ \mu\text{m} < \Delta < 0.625\ \mu\text{m}$, allows some heating of the atoms before they leave the trap. This results in two regimes. For lower Δ, the heating rate is initially very high due to the finite time taken to lose atoms from the trap. For larger Δ, there is slower heating than the
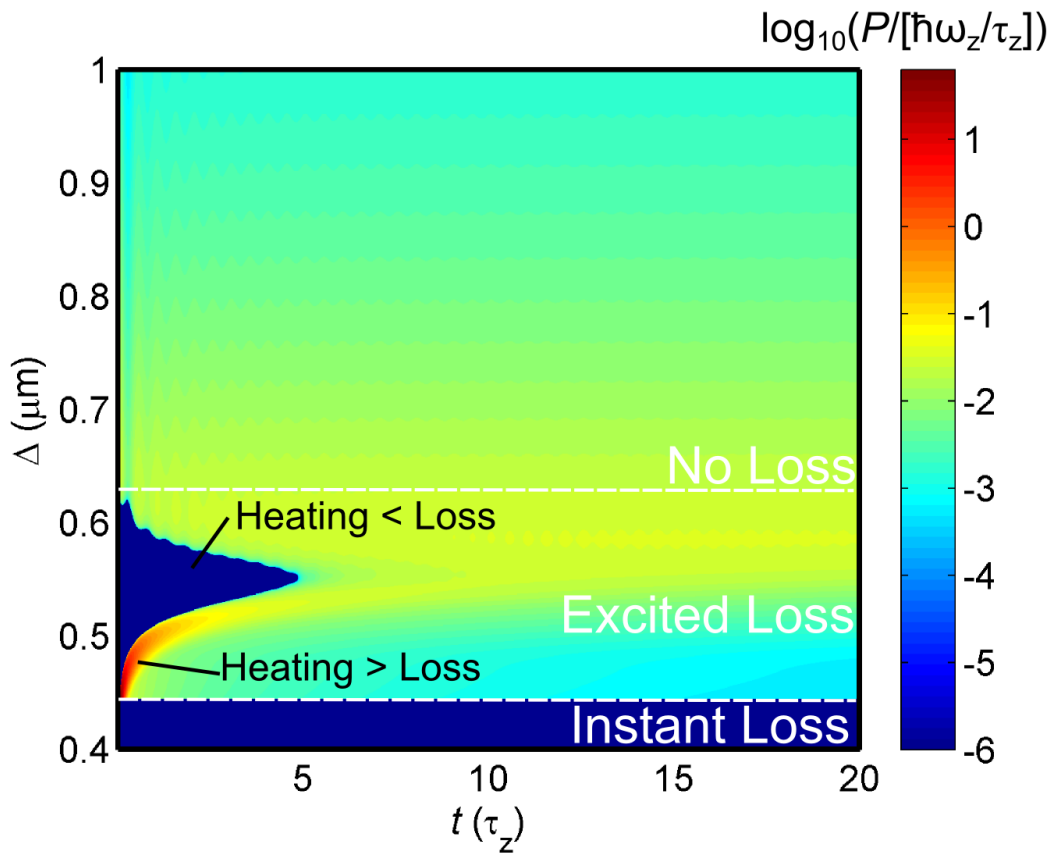
Figure 6.3: Plot of average power exchanged between cantilever and atoms, P versus t and surface-trap centre separation Δ. Labelled regions show instant trap loss for small Δ, intermediate atom loss due to excitation (including regions where the heating is greater than the loss rate due to the finite time required for loss and the opposing region) and the large Δ region where low heating and negligible loss occurs.

loss rate and so very little power transfer. The last two regimes both reach a steady state at longer times due to heating, atom loss, and the U_b limit of trap harmonicity. The third regime occurs at very large separations, where almost no atoms are lost from the trap. However, increasing Δ reduces the driving due to the cantilever, resulting in very little heating. Figure 2 of [70], which shows the fraction of atoms remaining when held near a thermal oscillating cantilever, agrees strongly with these results. However, as explained in the reference, the thermal part of the atom cloud, along with the increased surface attraction due to adsorbates, caused a broadening of the loss rates measured in the experiment.

Figure 6.3 shows that there is no possible surface-trap separation where this experimental set up could allow for coherent exchange between the cantilever and the condensate, as the power transfer rate is, at maximum, only $\sim 10^2 \hbar \omega_z / \tau_z$, which is much less than the $10^5 \hbar \omega_z / \tau_z$ required. Secondly, this transfer rate needs to be near instantaneous and remain for the majority of the interaction in order to allow the cantilever to feel the presence of the condensate. Therefore, even using a cryogenicaly-cooled cantilever with a higher quality factor, ($T = 5$ K and $Q = 80,000$ [100]) so that $P_{th} \sim 10^3 \hbar \omega_z / \tau_z$, would not allow $P > P_{th}$.

6.3   Parallel Driving Configuration

We now propose a different experimental configuration which should allow for much greater power transfer between the condensate and the cantilever. The largest issue with the perpendicular arrangement, described above, is the resonance requirement $\omega_z = \omega_c$. This ensures that the trap must have a fixed trap frequency in the surface direction, z, which greatly constrains the possible trap-surface separations.

Figure 6.4a) shows an alternative arrangement, which uses a cigar-shaped condensate (red) with $\omega_x = \omega_c$, which allows ω_z to be much greater than in the previous experiment. Thereby allowing the condensate to be placed much closer to the cantilever (blue) and increasing the δ / Δ ratio. Figure 6.4b) shows the previous experimental set up for comparison. The restriction that $\omega_z = \omega_c$ limits the minimum value of Δ, as shown by the results of figure 6.3.

In addition, this 'parallel' configuration is useful because, in the limit of no interactions, the atom motion wont be excited in the z direction and so the atoms won't escape the trap any faster than the low energy groundstate
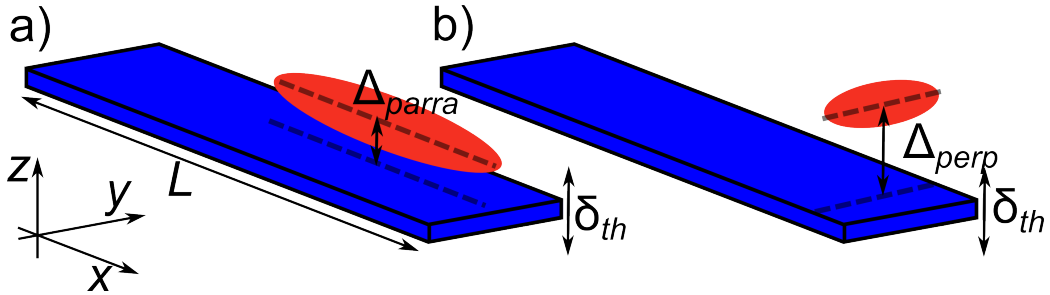
Figure 6.4: Schematic of a) parallel trap-cantilever orientation, in which the condensate is confined tightly in the z direction in order to minimize Δ_{parra}, b) perpendicular orientation used in [70], which sets $\omega_z = \omega_c$, requiring $\Delta_{perp} > \Delta_{parra}$ in order to trap atoms for experimentally useful lifetimes.

will allow. This means that the primary readout method will not be the loss of atoms, which pollutes the cantilever and leaves small signal-to-noise ratios. Instead, readout will be via the direct observation of the condensate motion and energy distribution, allowing for much greater information to be ascertained.

However, the energy transferred also depends on how long a large number of atoms can be held. Therefore, we can further aid the coupling by vastly increasing the number of atoms that can be held for longer times. As shown in previous discussions of atom-cantilever interactions, this attempt to overcome the incredible mass disparity between these two systems is a reasonable method to increase their coupling [69]. To do this, we assume that the trap frequency in the y direction is low enough that we are in the 2D regime, as defined in the previous chapter, section 5.5. To ensure there are no edge effects, we will then make the following restriction:

$$\omega_y \leq \frac{2}{L_y}\sqrt{\frac{2\mu}{m}}. \tag{6.21}$$

Then, using a large, but experimentally viable, perpendicular trap frequency $\omega_z = 2\pi\ 70$ kHz [101], we need to find the optimal separation that will cause large driving whilst allowing the trap to hold a large number of atoms for a significant amount of time.

The initial number of atoms that are placed in the trap is calculated by fully integrating the 2D atom density in equation (5.50) with a chemical potential that satisfies the requirements in equation (5.40). This produces a

condensate with $N_o = 15.5 \times 10^3$ atoms, less than one order of magnitude greater than those used in the previous experiment. Therefore any increase in coupling cannot simply be attributed to an increase in atom number.

6.3.1 Cantilever Oscillation Modes

Aligning the atoms along the cantilever will also allow the spatial form of the cantilever's flexing to play a role in the coupling between the two systems. As explained above, there are many texts that derive the motion of a cantilever and its profile as it oscillates [99]. We summarise the key results here. Cantilevers can flex in series of quantized modes given by:

$$z_c(x) = \delta \sin(\omega_n t) f_n(x, L), \tag{6.22}$$

where:

$$f(k_n l) = [\cos(k_n x) - \cosh(k_n x)] - \left[\frac{\cos(k_n L) - \cosh(k_n L)}{\sinh(k_n L) - \sin(k_n L)}\right] \tag{6.23}$$
$$\times [\sin(k_n x) - \sinh(k_n x)]$$

and L is the length of the cantilever. The wavevector of each mode, k_n, can be found from the solutions to:

$$\cos(k_n L)\cosh(k_n L) = -1, \tag{6.24}$$

which go as $k_n \approx (n + 1/2)\pi/L$ for larger n. The frequencies for each mode are given by:

$$\omega_n = B_c k_n^2, \tag{6.25}$$

where $B_c = \sqrt{E_Y/12\rho}L_z$ is a constant defined by the physical parameters of the cantilever, E_Y is the Young's modulus, ρ is the density and L_z is the cantilever thickness. For the cantilever used in [70], these produce a ground-state wavevector $k_1 = 9375$ m^{-1} and, using the accepted values for SiN, a frequency of $\omega_1 = 2\pi\ 17.5$ kHz; much larger than that found experimentally. However, this frequency relation doesn't take into account the addition of the metal layer to the cantilever, which makes the cantilever stiffer and denser, hence lowering its oscillation frequency. Therefore, we use an altered E_Y/ρ ratio to give $\omega_1 = 2\pi\ 10$ kHz, the value measured in the experiment [70].
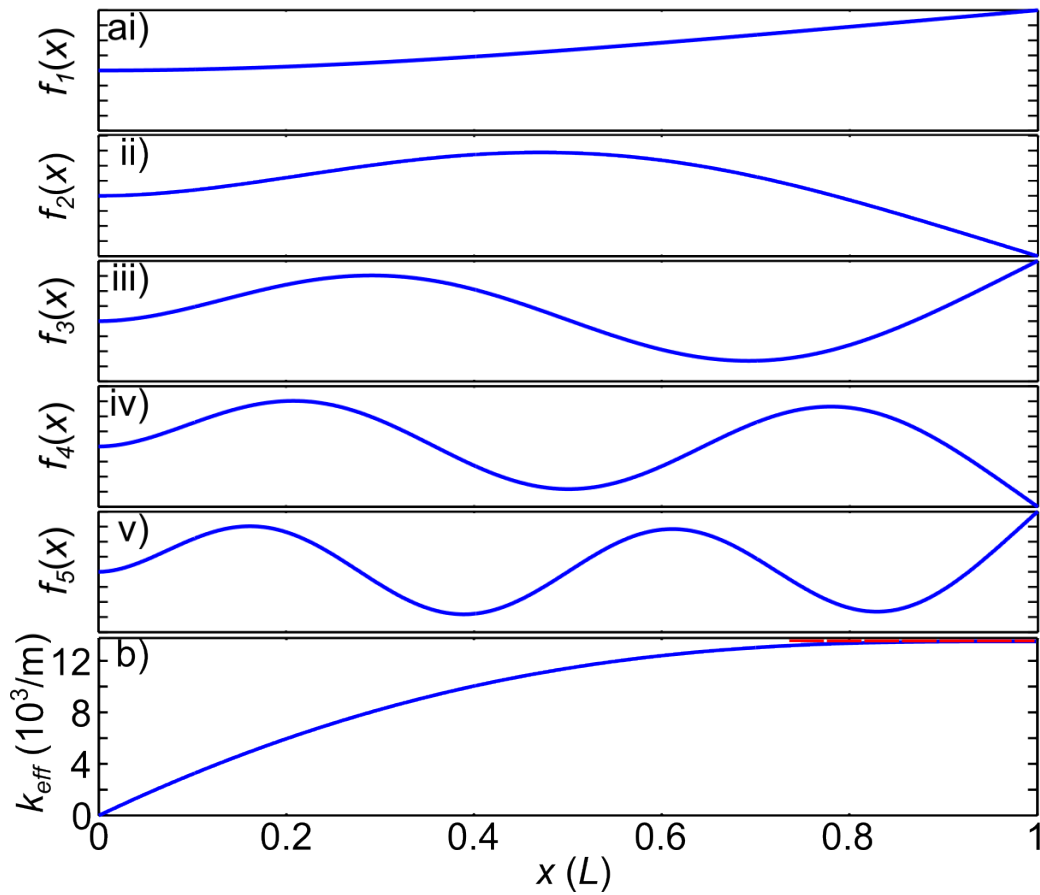
Figure 6.5: ai-v) Spatial profiles, $f_n(x)$, of the $n = 1 - 5$ flexing modes of a cantilever fixed at $x = 0$, in arbitrary units. Note the increasing sinusoidal nature with increasing n. b) Effective wavevector of the $n = 1$ mode. Harmonic traps centred on $x > 0.9L$ will be driven by an effective wavevector greater than k_1 (shown by red dashed line).

Figure 6.5ai-v) shows the spatial profiles of a cantilever oscillating in modes $n = 1 - 5$. The $n = 0$ mode has been omitted as this gives $k_0 = 0$ and $\omega_0 = 0$. For the lowest mode, it can be seen that the cantilever bends non-linearly for low x and becomes more straightened as $x \sim L$. This is shown in figure 6.5b), which shows the effective wavevector, $k_{eff} = dz_c(x)/dx$, with position along the cantilever. For low x, this varies greatly and becomes larger and constant near the end of the cantilever. Conversely, for higher n, the cantilever modes become ever more sinusoidal. For the ensuing discussion, we will assume that all oscillation of the cantilever takes place in the groundstate $n = 1$ mode as higher modes are only minimally occupied by thermal phonons [99].

This means that in the weak driving regime, $\Delta \gg \delta$, the force felt by the atoms from the cantilever can be approximated by:

$$F_o = \frac{4C_4}{\Delta^5} \delta k_{eff}(x + x_o), \tag{6.26}$$

where x_o, is position of the trap centre along the cantilever. Figure 6.5b shows that for $x_o > 0.9L$ the wavevector, $k_{eff} = 1.38 \times 10^4$ m^{-1} is maximal and independent of x. This will also allow the atoms to travel a distance of $0.1L = 20$ μm in their trap, along the cantilever, without 'falling off the edge'.

Lastly, we have omitted any z dependence in equation (6.26), as the larger trapping frequencies in this direction will be far from resonance with the cantilever oscillation frequency, thus limiting excitation along z.

Comparing equation 6.26 with the force from the perpendicular driving, equation (6.12), we see that this actually produces a weaker force as $k_{eff} \ll 1/\Delta$. Therefore, if we wish to produce stronger coupling, we must compensate by reducing the atom-surface separation by an amount:

$$\Delta_{para} < \left(k_{eff} \frac{\Delta_{perp}^6}{5} \right)^{1/5}, \tag{6.27}$$

where $perp$ and $para$ signify perpendicular and parallel separations. From the results in figure 6.3, the optimum separation is around $\Delta_{perp} \approx 0.55$ μm. This means that, to be comparable, the separation in the parallel configuration would have to be $\Delta_{para} < 150$ nm. The results in the previous section show that this can only be achieved if the atoms are trapped for very short times $\tau_{exp} \ll 1\tau_x$ or the perpendicular trap is tightened to a prohibitively high frequency of $\omega_z \gg 2\pi$ 100 kHz.

Cantilever Scaling Relations

Instead of decreasing Δ to produce increased heating power, we can use the previous cantilever relations to find more optimal cantilever dimensions. First, as we have seen from the forced oscillator solutions:

$$E_a \sim F_o^2 t^2, \tag{6.28}$$

where

$$F_o \sim \delta k_{eff} \sim \frac{1}{\sqrt{L_x L_y L_z}} \frac{1}{\omega_x} \frac{1}{L_x}. \tag{6.29}$$

Therefore, the power goes as:

$$P \sim \frac{E_a N}{t} \sim \frac{1}{L_x^3 L_y L_z \omega_x^3 \omega_y}. \tag{6.30}$$

where $L_x = L$ is the cantilever length and L_y and L_z are the cantilever width and thickness. Note that we have used the 2D condensate to approximate the atom number. We can then relate the frequencies to the cantilever dimensions using the wavevector and y-direction Thomas-Fermi relations:

$$\omega_x \sim \frac{L_z}{L_x^2} \tag{6.31}$$

and

$$\omega_y \sim \frac{1}{L_y}, \tag{6.32}$$

which gives:

$$P_{av} \sim \frac{L_x^3}{L_z^4}. \tag{6.33}$$

Finally, the value we wish to maximise is the ratio of the average power to the incoherent thermal phonon power, which gives:

$$\frac{P}{P_{th}} \sim \frac{L_x^9}{L_z^7}. \tag{6.34}$$

Therefore, in order to maximise the coupling, we need a long (large L_x), thin (small L_z) cantilever. However, this may well push the cantilever into

the thin-membrane regime and, hence, for $L_z \sim 100$ nm we will need to use the 5th order Casimir-Polder relation given in the previous chapter, section 5.2. This slightly alters the scaling relation to:

$$\frac{P_{av}}{P_{th}} \sim \frac{L_x^9}{L_z^5}, \tag{6.35}$$

as a factor of L_z appears in the numerator of the force constant. Note that L_y doesn't appear, as a wider cantilever allows for more atoms to be placed on top of it without edge effects, but is heavier which causes a drop in the oscillation amplitude and power.

It has been shown that very thin, very high quality cantilevers can be made. We will therefore use an extreme, but still viable, cantilever with dimensions $L_{x,y,z} = [200, 8, 0.04]$ μm [100, 102, 103].

Figure 6.6 shows the average power transfer from the cantilever to the condensate, in the parallel configuration, for a range of trap-surface separations over an extended time $0 < t < 100\tau_x$. In general the average power is typically 1000 times larger for this parallel configuration across all separations and for longer times than those found in the perpendicular experiment. Power transfer is also improved by the increased atom number, but that alone does not explain the size of the increase, which mainly results from decreased losses at small atom-surface separation. However, we still see the same large initial heating rates for very small Δ due to the finite time taken to lose atoms as explained in the previous section. Note that even for the smallest separation, $\Delta > 300\delta$, and so the weak driving approximation still holds.

Figure 6.6 also shows the clear optimum region for atom-surface separations, $\Delta \approx 0.3$ μm, which balances the losses due to the surface whilst also compensating for the weaker parallel driving, resulting in $P_{av} \approx 10^5 \hbar \omega_x / \tau_x$. The average atom loss rate is $0.22\%/\tau_x$ at this separation.

For a cantilever of these dimensions and a relatively high Q factor, $P_{th} \sim 10^6 \hbar \omega_x / \tau_x$. Therefore we are below of the value required to completely overcome the thermal driving of the cantilever. The thermal coupling of the cantilever could be overcome by using the high-order power in the scaling equation (6.35). By lengthening the cantilever further to 300 μm the maximum power would jump to $\sim 10^7 \hbar \omega_x / \tau_x$ and dominate the incoherent thermal noise. This would lead to rapid cooling of the cantilever, on a scale that can easily be detected by observing the change in amplitude of the cantilever's oscillation [104].

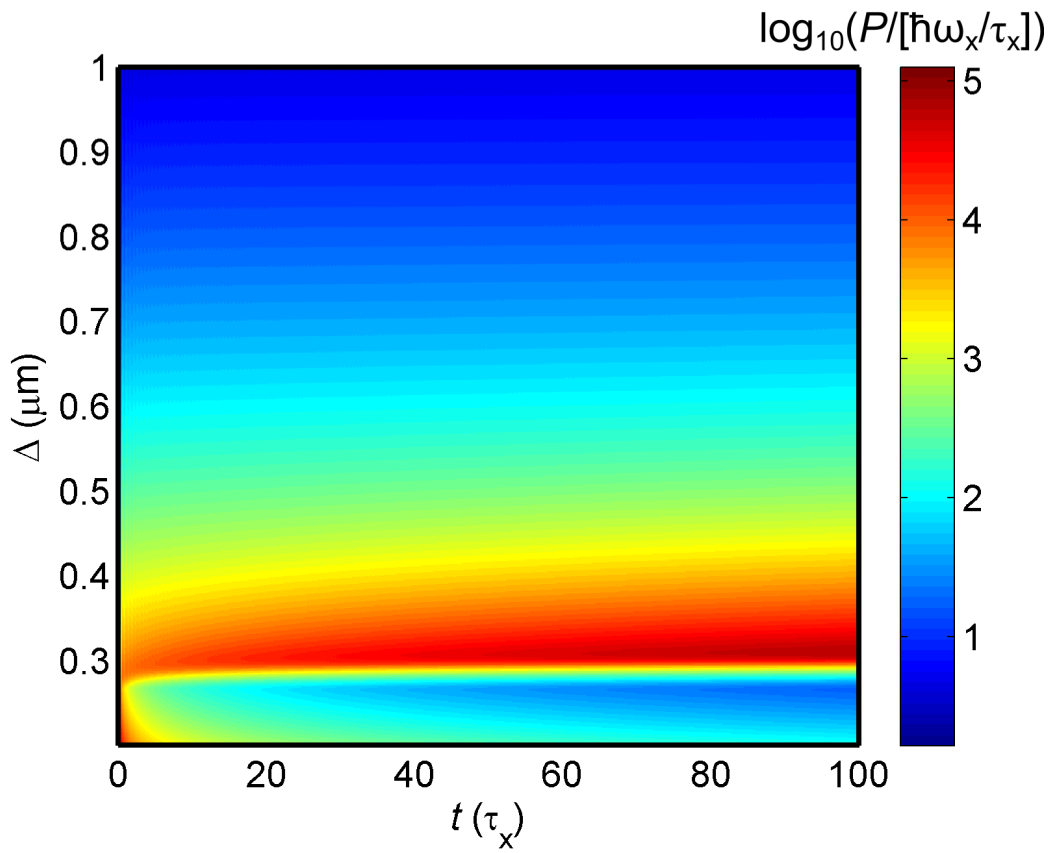Figure 6.6: Plot of average power exchanged between the cantilever and atom cloud, P, versus time, t, and surface-trap centre separation, Δ, for the parallel arrangement described above. Initial high heating rates at small separations are due to the finite time taken for atom losses. The optimum surface separation, which balances losses with large driving strength, occurs when $\Delta = 0.3$ μm.

Lastly, we have ignored the back action on the cantilever from the atoms. If the cantilever's motion heats the atoms faster than the cantilever can re-equilibrate, then the amplitude of the cantilever oscillation will diminish and so will the heating rate. This could be modelled in a simple manner by increasing the γ_{th} term in the cantilever's forced-damped equation of motion (6.3). However, this would only be correct when a steady state exchange of energy between the thermal bath, the cantilever and the atoms is reached. This would occur on very long timescales as the energies of the trapped atoms and cantilever become comparable, which is not experimentally viable. A more accurate model would need to include the transient, non-equilibrium, dynamics when the tip of the cantilever is not in thermal equilibrium with the bath, thereby producing a spatially dependant F_{th}.

However, even though $P < P_{th}$, this is still an exceptional feat considering the energy and mass disparity of these two systems. By analogy, cooling a micromechanical system with a condensate is similar to using a room temperature planet earth to cool something a hundred times the mass and core temperature of the sun.

Quantum and Interacting Results

The previous results were derived by using analytical results for the excitation of the atoms, which, as shown in chapter 3, often agree well with quantum mechanical simulations in the limit that $E_a \gg \hbar\omega_{x,y,z}$. However, in the extreme geometry that we propose, this is not certain to still be the case. Therefore, in the following we present the results from the numerically evolved PGPE:

$$i\hbar\frac{d\psi}{dt} = \mathcal{P}\left[-\frac{\hbar^2}{2m}\nabla^2 + \frac{m}{2}\boldsymbol{\omega}^2.\mathbf{x}^2 + g|\psi|^2 + U_{CP}\right]\psi, \qquad (6.36)$$

defined in chapter 2. Atom loss will be included by normalising the wavefunction to the $N(t)$ relation given in equation (6.17).

Figure 6.7 shows the average power versus time calculated using the optimum system parameters revealed in figure 6.6 for the classical analysis (dashed light blue), and using the non-interacting (red) and interacting (blue) PGPE. Firstly, the non-interacting and classical results agree very well as expected. However, the interacting system shows a small reduction in the energy transferred to the condensate. This reduction is due to the large interacting cloud behaving as a much 'stiffer' system because the ensemble of
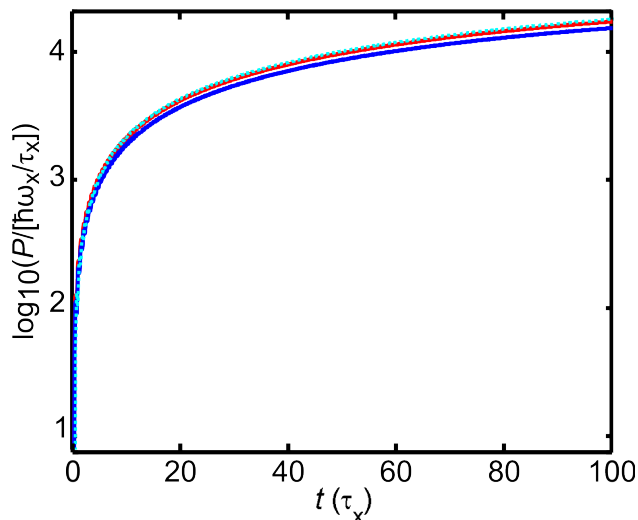
Figure 6.7: Comparison of power transfered from the cantilever to the harmonically-trapped atoms using the non-interacting (red) and interacting (blue) PGPE, both of which largely agree with the classical results (dashed blue).

atoms act more like one solid mass, which effects the cantilever's ability to excite them. Therefore in the limit of large interactions, to first order:

$$F_o \sim \frac{1}{m} \to \frac{1}{Nm}, \tag{6.37}$$

which means that the power drops as $P \sim 1/N$. Previously the average power had no scaling with L_y, but with interactions $P \sim 1/L_y$. Therefore, the reduction in heating due to interactions can be at least partially mitigated by reducing the width of the cantilever.

Figure 6.7 also clearly shows that the coupling power increases with increasing t. This suggests that greater coupling can simply be achieved by holding atoms longer above the cantilever. However, this is not particularly useful as the atoms would need to be placed in ever deeper and more harmonic traps and, over long timescales, there would still be a sizeable decohering effect from the thermal phonons. Therefore, larger initial power is preferable.

6.3.2 Higher Modes and Stochastic Webs

Harmonically trapped atoms can be coupled to higher modes of the cantilever. However, due to their decreasing amplitudes resulting from thermal excitation, or a single 'ringing' perturbation [99], these modes have to be specifically driven. This can be carried out via devices, such as the piezoelectric crystal used in the experiment described in [70], set to oscillate in resonance with a mode frequency ω_n.

As shown in figure 6.5, for larger mode number, $n \gtrsim 5$, the cantilever profile becomes very sinusoidal, with increasing wavevector, especially at lower x. Firstly, this means that it is possible to create the same type of non-KAM chaos as seen in chapter 3, as the cantilever produces a perturbation similar to a standing wave. Secondly, the high wavevector will allow a large driving force, F_o, even in the weak driving limit, $\Delta \gg \delta$.

For $n \geq 5$ we approximate the atom-cantilever attraction using the standing wave potential:

$$U_{CP} = 4\frac{C_4}{\Delta^4}\delta \sin(\omega_n t) \sin(k_n[x - x_o]).$$ (6.38)

The amplitude of the oscillation, δ, and the trap position, x_o, are now free parameters (subject to the weak driving constraint and the $x \lesssim L/2$ sinusoidal requirement).

Frequency-Length Scale Relation

Equating the trap frequency and the mode frequency, $\omega_x = \omega_n$, fixes the harmonic oscillator length, $l_x = \sqrt{\hbar/m\omega_n}$. Therefore, using the wavevector relation given in equation (6.25), the dimensionless wavevector of the cantilever is given by:

$$\tilde{k} = k_n l_x = \sqrt{\frac{\hbar}{mB_c}}.$$ (6.39)

This wavevector relation results in the mode overlap integral:

$$S_{\alpha\alpha'} = \int_{-\infty}^{\infty} \phi_\alpha(x/l_x)\phi_{\alpha'}(x/l_x) \sin(k_n x)dx/l_x$$
$$= \int_{-\infty}^{\infty} \phi_\alpha(\tilde{x})\phi_{\alpha'}(\tilde{x}) \sin(\tilde{k}\tilde{x})d\tilde{x},$$ (6.40)

which is now entirely independent of n, ω_n, or L. This means that, for any mode, the harmonically-trapped atoms will see exactly the same effective wavevector, even if the frequency of the cantilever is greatly altered. This effect is evident in figure 6.8, which shows the energy of a non-interacting atom calculated versus time as it is resonantly driven by cantilevers of lengths (160 to 220 μm). The change in L results in different frequencies ($\approx 5-20 \times 2\pi$ Hz) for a cantilever, driven with $\delta = 120$ nm in the $n = 5$ mode and with a trap-surface separation of $\Delta = 0.6$ μm. The inset of figure 6.8 shows a detailed plot of how the different cantilevers cause atom-cloud excitations of varying frequencies and magnitudes. The varying amplitudes of the periodic excitation are due the relative amplitude of the cantilever's driving, given by:

$$\tilde{U}_o = 4 \frac{C_4}{\hbar \omega_n \Delta^4} \delta, \tag{6.41}$$

which scales with the trap frequency. Figure 6.8 therefore highlights a secondary effect; the rate of excitation and the amplitude of excitation cancel on timescales $\gg \tau_n$, resulting in the same behaviour for the different cantilever lengths and frequencies.

Web-Limited Heating

As described in the chapter 3, sinusoidal spatio-temporal potentials excite non-KAM chaotic motion in resonantly-driven atoms. This can be seen indirectly from the maximum excitation of the atoms or, more explicitly, by periodically imaging the phase-space distribution of the atoms. However, in order to see these effects the atom cloud must travel far along the cantilever but still be excited by it. This requires:

$$\frac{A_R}{k_n} < \min[x_o, L - x_o], \tag{6.42}$$

where A_R is the first zero in the Bessel function of order R. The requirement on the left-hand side of equation (6.42) is the spatial extent of the stochastic web. Therefore, keeping $x_o \leq L/2$ will ensure that the atoms will spend most of their time in the sinusoidal region of the flexing cantilever. The inequality in equation (6.42) will therefore be fulfilled so long as $n \gtrsim R + 2$, i.e. for $R = 1$, n need only be greater than 3. The maximum scaled energy
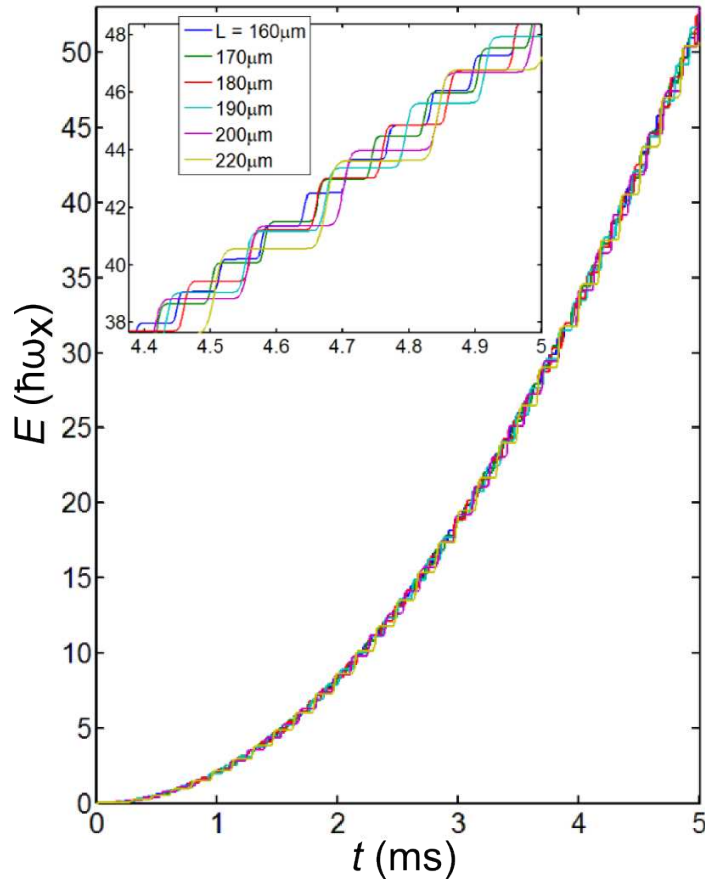
Figure 6.8: Energy versus time calculated for harmonically-trapped atoms held above cantilevers of varying lengths (see legend). Inset: detailed view showing that the excitation rate is almost independent of L, because $\omega_n \sim 1/L^2$, and amplitude variation, $\tilde{U}_o \sim 1/\omega_n \sim L^2$, cancel on long timescales. Parameters given in the text.

that atoms can then be excited to is derived in section 3.2.3, substituting in equation (6.25) for the frequency then gives:

$$\tilde{E}_{ring} = \frac{mA_R^2}{2\hbar}B_c.$$

(6.43)

For the SiN cantilever used so far, $E_{ring} \sim 10^5$ and exciting atoms to this value would be computationally and experimentally prohibitive. We can, instead, use a soft, thin cantilever with a low Young's modulus, high density and low L_z to reduce B_c, which is the only parameter that we are free to vary in equation (6.43). Exactly how this would be achieved isn't obvious though producing a cantilever from composite materials has allowed parameters to be tuned successfully [105–107].
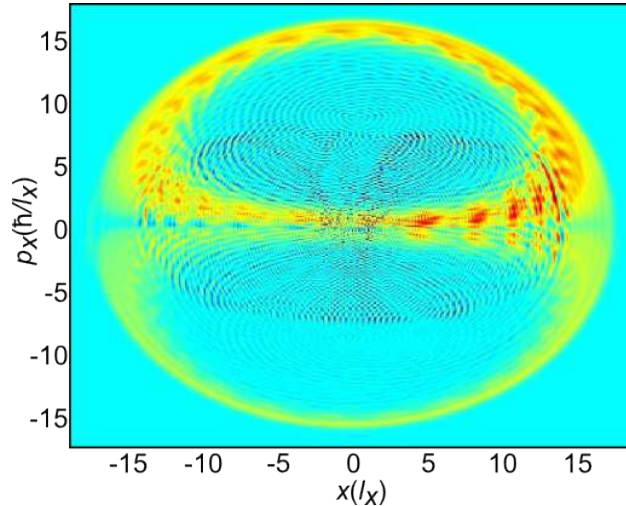
Figure 6.9: Poincaré section calculated for atoms resonantly driven ($R = 1$) by the $n = 12$ mode of a soft cantilever. The cantilever constant $B_c = 10^{-8}$ ms^{-1} producing $\rho_{ring} = 15.5$ and $E_{ring} = 120\hbar\omega_x$. No approximate potentials were used, showing that complete stochastic webs can be created from the cantilever-atom interaction.

Figure 6.9 shows a Poincaré section (as defined in the chapter 3) of atoms excited by a 'soft' cantilever with $B_c = 10^{-8}$ ms^{-1}. For which $E_{ring} = 120\hbar\omega_x$ and $\rho_{ring} = 15.5$, which corresponds to the radius of the phase-space in which the atoms are confined. This stochastic web was produced using the full Casimir-Polder potential and cantilever flexing potential, with no approximations, showing that stochastic webs can be produced by the interaction of a

103

driven cantilever and harmonically trapped atoms. This shows that, whilst any coupling of these two systems allows for energy transfer from the relatively high temperature cantilever to the cold atoms, the profile of the flexing cantilever can be used to directly control this coupling.

6.4   Conclusion

Following our investigation of stationary surfaces in chapter 5, we considered a recent experiment using an oscillating cantilever to couple a condensate and a surface via the Casimir-Polder attraction. The large loss rates found in the experiment were attributed by the investigators to surface contamination due to previously lost atoms coating the cantilever. However, the results presented above challenge this explanation, as a change in the atom-surface attraction would produce a measurable shift in the resonant frequency of the trap: which was not seen in the experiment. A more likely explanation is either a miscalculation of the surface-trap separation or an underestimate of the driving force of the cantilever on the atoms.

An alternative experimental set up was then proposed, in which a different orientation of the condensate relative to the cantilever was used. This 'parallel' set up was designed to cause the trapped atoms to be resonantly driven along the cantilever. This allowed the previously resonant trap frequency, perpendicular to the cantilever, to be greatly increased allowing a much smaller separation between the trapped atoms and the cantilever. Due to the 4th and 5th order power laws of the Casimir-Polder attraction, this decreased distance produced much greater coupling. Conversely, even the very small oscillation of the cantilever due to thermal phonons could drive condensate motion. Further, the strength of the coupling was shown to be large enough to overcome the environment-cantilever coupling, and could therefore work to passively cool the cantilever. This regime, impossible to achieve with the perpendicular experimental arrangement, could, in principle, be used to perform state readout or manipulation of the cantilever due to interaction with the atom cloud as the decohering effect of the thermal phonons can be overcome.

Lastly, we showed that the shape of the flexing cantilever can cause non-KAM chaotic motion in the driven atoms. Also, due to the wavevector-frequency relation of the cantilever, its parameters directly control the extent to which this excitation occurs.

Chapter 7

Finite Temperature BECs: In-Situ Densities

7.1 Introduction

The previous chapters have investigated a zero temperature gas of atoms, in which all the atoms are in the groundstate, often referred to as the condensate or condensate mode. Time dependent potentials were then used to excite atoms in this groundstate to higher energy, non-equilibrium states.

If $T_c > T > 0$ not all the atoms will be in the condensate groundstate, instead they will be distributed over a range of modes. However, we will assume that the temperature is still below the critical temperature, T_c (as explained earlier) and that the groundstate is still macroscopically occupied. The following finite temperature description of a trapped atomic gas can be found in a large number of many-body physics references (for example [108] provides a relatively straightforward explanation). Here, we shall only highlight the main results and, in keeping with the previous chapters, semiclassical notation will be used. As such, the semiclassical formalism of replacing non-commuting operators with commuting complex variables, will be used.

For temperatures greater than 0, the atoms can no longer be described by a single, mean-field, wavefunction. Instead we shall use:

$$\psi = \psi_0 + \sum_{i>0} \psi_i = \psi_0 + \delta\psi, \qquad (7.1)$$

where the condensate mode is given the subscript 0 and all excited modes,

$i > 0$, are collectively described by $\delta\psi$. Using the effective potential interaction given in the Gross-Pitaevskii equation, the atomic collisional term is now:

$$g|\psi|^2 = g\left(|\psi_0|^2 + \psi^*\delta\psi + \psi\delta\psi^* + |\delta\psi|^2\right). \tag{7.2}$$

The Hamiltonians for the condensate and the excited atoms are then:

$$\left[\frac{-\hbar^2}{2m}\nabla^2 + U + gn_0 + 2gn_{th}\right]\psi_0 = \mu\psi_0 \tag{7.3}$$

and

$$\left[\frac{-\hbar^2}{2m}\nabla^2 + U + 2gn_0 + 2gn_{th}\right]\psi_i = \epsilon_i\psi_i, \tag{7.4}$$

where U is the total external potential used to trap and excite the cloud and ϵ_i is the energy of the ith excited level. The factors of 2 appear in the interaction terms as there are two asymmetric interactions between condensate-thermal atoms and thermal-thermal atoms. Figure 7.1 shows these diagrammatically, a) is a Feynman diagram of an excited particle (wavy line) colliding with a condensate atom (straight line) via the s-wave scattering interaction (dashed line). After the collision the particles are unchanged, which is known as the 'Hartree' interaction. Figure 7.1b) shows a similar diagram with the same particles exchanged after the collision, which is known as the 'Fock' interaction. In a similar manner, an excited particle in the ith level may collide with a particle in the jth level and undergo either type of interaction. Considering that the total number of excited levels can be very large, the ith-i^{th} level interactions can be omitted.

Equations (7.3) and (7.4) are the "Hartree-Fock" (HF) equations as they only contain these two interactions. Higher order terms, including non-Hermitian or complex densities, have been omitted to form a coupled set of semiclassical equations.

So far, we haven't defined the energy spectrum, ϵ_i, of the excited atoms. Whilst this should include all possible real and virtual excitations (representing quantum fluctuations), by using the Hartree-Fock approximation and assuming that the cloud is initially at equilibrium, the only excitations we will consider will be those due to the thermal occupation of higher energy states. Therefore, by minimising the total energy functional:

106

a) Hartree
Interaction
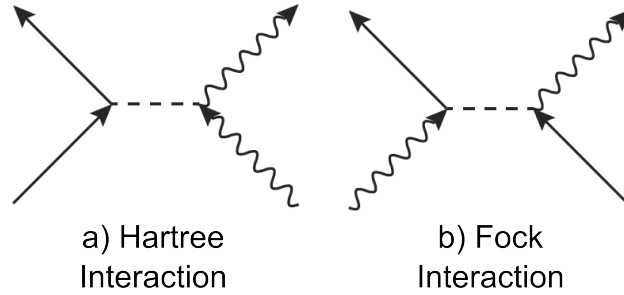
b) Fock
Interaction

Figure 7.1: Feynman diagrams of a) Hartree interaction between a condensate (straight line) and thermal (wavy line) atom, mediated by s-wave scattering (dashed line), b) Fock interaction, causing the condensate and thermal atoms to be exchanged after the interaction.

$$E_{tot}[\psi_i] = \int \left[\mu |\psi_0|^2 + \sum_{i>0} |\psi_i|^2 \epsilon_i \right] d\mathbf{r} \qquad (7.5)$$

under constant entropy and atom number, the thermal distribution is given by the Bose-Einstein distribution [109]:

$$f(\epsilon_i) = \frac{1}{e^{\frac{\epsilon_i - \mu}{k_B T}} - 1}. \qquad (7.6)$$

Using this distribution and the Hartree-Fock equations, the final step is to find the condensate and thermal cloud densities. Due to the coupling of the two HF equations, this can't be carried out analytically. However, as shown shortly, this can be done with a few reasonable approximations.

7.2 Measuring Thermodynamic Properties of a BEC

Whilst Bose-Einstein condensates have been routinely produced for some years [7], the methods used for understanding the BECs produced have progressed more slowly. Currently, nearly all the thermodynamic properties of the BEC (namely atom number, condensate fraction, chemical potential and temperature) are extrapolated from the density distribution of the atom

cloud. Typically this is carried out by using an optical absorption method as described in the previous reference.

For simplicity, two dimensions of the cloud are often 'integrated out' by summing the absorption data over these directions. Then, so long as the trap frequency is known in the remaining direction, the thermodynamic parameters (primarily the temperature, T, and chemical potential, μ) can be found by fitting an analytical density distribution to the experimentally found density. We shall now list three different analytical approximations of the Hartree-Fock equations of increasing complexity and decreasing approximation.

7.2.1   Ideal Gas Description

We begin with the simplest and most often used description of a finite temperature cloud of atoms. The ideal gas or "bi-modal" approximation ignores all interactions between atoms except in the case of condensate-condensate collisions. This requires that the condensate is very accurately described by the Thomas-Fermi distribution, i.e. $\mu \gg \hbar\omega_{x,y,z}$ which requires a very cold gas producing a very large condensate fraction. Simultaneously, the thermal atoms must be highly energetic so their kinetic energy is much larger than that of the repulsion by the very dense condensate so that the interaction can be neglected. Lastly, the cloud is required to be high temperature so that the majority of the thermal atoms have energies much larger than μ so that the Maxwell-Boltzmann approximation of the Bose-Einstein distribution can be used which ignores Bose-enhancement, i.e.:

$$f(\epsilon_i) = \frac{1}{e^{\frac{\epsilon_i - \mu}{k_B T}} - 1} \approx e^{\frac{-\epsilon_i + \mu}{k_B T}}. \tag{7.7}$$

The inconsistency of these requirements means they cannot be upheld and so inaccuracies are inherent in this description.

The spatial density for the thermal cloud is then found by substituting:

$$\epsilon = \frac{\hbar^2 k^2}{2m} + U \tag{7.8}$$

into the Maxwell-Boltzmann equation, where we have used a continuum approach for the energy levels ϵ_i. Then, by spherically integrating over all momentum k, we find the spatial density:

$$n_{th}(x, r) = \left(\frac{m k_B T}{2 \pi \hbar^2} \right)^{3/2} e^{\frac{\mu - U}{k_B T}}. \tag{7.9}$$

Then, using the trapping potential:

$$U = \frac{m}{2} \left(\omega_r^2 r^2 + \omega_x^2 x^2 \right), \tag{7.10}$$

where $\omega_r = \sqrt{\omega_y \omega_z}$ is the cylindrically symmetric trap frequency, the line density of the thermal cloud can be found by radially integrating equation (7.9) to produce:

$$n_{th}(x) = \sqrt{\frac{m}{2\pi}} \frac{(k_B T)^{5/2}}{\hbar^3 \omega_y \omega_z} e^{\frac{2\mu - m\omega_x^2 x^2}{2k_B T}}. \tag{7.11}$$

The condensate density is then found using the Thomas-Fermi approximation [109]. This takes the Hartree-Fock equation for the condensate and assumes the groundstate atoms are sufficiently low energy that they posses no kinetic energy, leaving the trap potential, U, and self-interaction potential, gn_0, to dominate the condensate mode. Then by multiplying equation 7.3 through by ψ_0^*, and using $n_0 = |\psi_0|^2$, it is trivial to solve for the Thomas-Fermi condensate density:

$$n_0 = \frac{1}{g}(\mu - U)\,\delta(U < \mu). \tag{7.12}$$

The line density can then be found by carrying out the same radial integration as used above for the thermal cloud, producing:

$$n_0(x) = \frac{\pi}{gm\omega_y\omega_z} \left(\mu - \frac{m\omega_x^2}{2} x^2 \right)^2 \delta(m\omega_x^2 x^2 < 2\mu). \tag{7.13}$$

The total line density is then: $n_{tot}(x) = n_0(x) + n_{th}(x)$.

The temperature and chemical potential are found by altering T and μ in equations (7.11) and (7.13) until the experimentally found density and the theoretical prediction show the strongest agreement. This can be done by using a simple R^2 fit or by more complex means, which take into account experimental uncertainty in the absorption measurements, such as the χ^2 method. A description for both of these methods can be found in [110].

Once these are found the condensate fraction can be calculated by a final spatial integration of equations (7.11) and (7.13) to find the total number of thermal atoms:

$$N_{th} = \left(\frac{k_B T}{\hbar \omega_{ho}} \right)^3 \tag{7.14}$$

and the total number of condensate atoms:

$$N_0 = \left(\frac{2\mu}{\hbar \omega_{ho}} \right)^{5/2} \frac{a_{ho}}{15 a_s}, \tag{7.15}$$

where $\omega_{ho} = (\omega_x \omega_y \omega_z)^{1/3}$ is the spherically symmetric trap frequency and $a_{ho} = \sqrt{\hbar/m\omega_{ho}}$.

7.2.2   Semi-Ideal Thermal Cloud

As discussed above, the ideal-gas model ignores many terms in the Hartree-Fock equations as well as Bose-enhancement. Therefore, a much more accurate description can be found by including more terms in the coupled Hartree-Fock equations as well as the full form of the Bose-Einstein distribution. These equations are not straightforward to compute as they must be solved entirely self-consistently. Therefore some approximations still have to be made, though more consistently than those used in the ideal-gas model.

The primary assumption is that the thermal cloud is of sufficiently low density that both n_{th} terms in the Hartree-Fock equations can be ignored. We can then use the Thomas-Fermi approximation as we did previously. The thermal cloud will then be described by the Bose-Einstein distribution and the repulsion from the condensate will be taken into account in the total potential experienced by the thermal atoms. This description is known as the semi-ideal model, as although all collisions with the condensate are being taken into account, we are still ignoring thermal atom interactions (i.e. the thermal cloud is still treated as an ideal gas) [111]. The following derivation closely follows that found in [112]

As stated earlier, the condensate will be described using the Thomas-Fermi approximation as discussed above. However, the thermal cloud will require a little more intensive treatment. At equilibrium, the thermal cloud is given by the Bose-Einstein distribution:

$$n_{th}(\epsilon) = \frac{\rho(\epsilon)d\epsilon}{e^{\frac{\epsilon - \mu}{k_B T}} - 1}, \tag{7.16}$$

where we are assuming that enough thermal modes are occupied that we can treat ϵ as continuous and $\rho(\epsilon)$ is the density of states. We shall also use cylindrical symmetry to reduce the system to just two dimensions. Since we will only be calculating the line density of the cloud along x, we can use $r = \sqrt{y^2 + z^2}$ and $\omega_r = \sqrt{\omega_y \omega_z}$.

If we take:

$$\epsilon(k, x, r) = \frac{\hbar^2 k^2}{2m} + \frac{m}{2}\left(\omega_r^2 r^2 + \omega_x^2 x^2\right) + 2gn_o(x, r), \qquad (7.17)$$

and $\rho(k, x, r) = 2\pi k^2 dk\, 2\pi r dr\, dx$. We can then calculate the line density of the thermal cloud by integrating over all momentum and extraneous spatial dimensions (y and z). Using the method outlined in appendix C, we obtain:

$$n_{th}(x) = \sqrt{\frac{m}{2\pi}} \frac{(k_B T)^{5/2}}{\hbar^3 \omega_y \omega_z} \begin{cases} \sum_{l=1}^{\infty}\left[2 - e^{\frac{l}{k_B T}\left(\frac{m\omega_x^2}{2}x^2 - \mu\right)}\right]l^{-5/2} & |x| < x_{TF} \\[2mm] \sum_{l=1}^{\infty} e^{\frac{l}{k_B T}\left(\mu - \frac{m\omega_x^2}{2}x^2\right)}l^{-5/2} & |x| > x_{TF}. \end{cases}$$

We can see that this result could give large deviations from the Maxwell-Boltzmann relation used in the bi-modal fitting method, as only in the limit $k_B T \gg \mu$ do the summations in the above equations converge (using just the $l = 1$ terms), resulting in the Gaussian distribution assumed in the simpler model.

The final spatial dimension can then be integrated over to find the number of thermal atoms:

$$\begin{aligned}
N_{th} &= 2\left(\frac{k_B T}{\hbar \omega_{ho}}\right)^3 \sum_{l=1}^{\infty} l^{-5/2}\left(\int_0^{x_{TF}}\left[2 - e^{\frac{l}{k_B T}\left(\frac{m\omega_x^2}{2}x^2 - \mu\right)}\right]dx + \int_{x_{TF}}^{\infty} e^{\frac{l}{k_B T}\left(\mu - \frac{m\omega_x^2}{2}x^2\right)}dx\right) \\
&= 4\left(\frac{k_B T}{\hbar \omega_{ho}}\right)^3 \sqrt{\frac{\mu}{\pi k_B T}}\zeta(5/2) + \\
&\quad \left(\frac{k_B T}{\hbar \omega_{ho}}\right)^3 \sum_{l=1}^{\infty} l^{-3}\left[e^{\frac{l\mu}{k_B T}}\mathrm{erfc}\left(\sqrt{\frac{l\mu}{k_B T}}\right) - e^{-\frac{l\mu}{k_B T}}\mathrm{erfi}\left(\sqrt{\frac{l\mu}{k_B T}}\right)\right], \quad (7.18)
\end{aligned}$$

where $\zeta(5/2) \approx 1.3415$ is the Riemann zeta function and $\mathrm{erfi}(x)$ and $\mathrm{erfc}(x)$ are the imaginary and complementary error functions, respectively.

7.2.3 Solution of the Hartree-Fock Equations

Whilst the semi-ideal model outlined above will be accurate in the low temperature regime (where n_{th} is very low), at temperatures close to the critical temperature, T_c, when $n_{th} \gtrsim n_0$, it will lead to large inaccuracies. Therefore, to provide a more complete picture, the repulsion caused by the thermal cloud density can be included numerically by adding in the thermal cloud density term into equations (7.16) and (7.2.2), via:

$$n_0(x,r) = \max\left\{\frac{1}{g}\left[\mu - \frac{m}{2}\left(\omega_r^2 r^2 + \omega_x^2 x^2\right) - 2gn_{th}(x,r)\right], 0\right\} \quad (7.19)$$

$$n_{th}(x,r) = \left(\frac{mk_BT}{2\pi\hbar^2}\right)^{3/2} \sum_{l=1}^{\infty} \frac{Z_{full}^l}{l^{3/2}} \quad (7.20)$$

where:

$$Z_{full} = \exp\left[-\left(\frac{m}{2}\left(\omega_r^2 r^2 + \omega_x^2 x^2\right) + 2gn_0(x,r) + 2gn_{th}(x,r) - \mu\right)/k_BT\right]. \quad (7.21)$$

An iterative scheme can then be used to solve equations (7.19) and (7.20) and the line densities can be calculated via numerical radial integration.

Whilst this is a simple and intuitive method to include the effects of thermal cloud repulsion, it requires considerably larger computational resources than the two models given above. This is due to the requirement that a 2D density (or 3D density, if there is no useful symmetry to exploit) has to be calculated numerous times in order to ensure that both the sum over Gaussian terms and the self-repulsion have converged.

However, we propose a simpler scheme wherein the summations and the iterations required are solved just once and then interpolated to give the fully interactive densities. Firstly, we uncouple the two equations by substituting the full Hartree-Fock TF condensate density given in equation (7.19) into equation (7.20) to create an equation that only relies on the thermal cloud. Then, by noting that the thermal cloud density appears on both sides of equation (7.20), we can create an analogous transcendental equation:

$$X = a \sum_{l=1}^{\infty} \frac{e^{-l|b+X|}}{l^{3/2}}, \quad (7.22)$$

where:

$$a = \frac{2a_s}{\hbar} \sqrt{\frac{2k_B T m}{\pi}} \tag{7.23}$$

and

$$b = \frac{\frac{m}{2} \left(\omega_r^2 r^2 + \omega_x^2 x^2 \right) - \mu}{k_B T}. \tag{7.24}$$

The absolute exponent in equation (7.22) allows the thermal cloud to be calculated in both the condensate and non-condensate regions. The self-interacting thermal cloud can then be found using:

$$n_{th}(x,r) = \frac{k_B T}{2g} X \left(a[T], b[r,x,\mu,T] \right). \tag{7.25}$$

This means that the thermal density has essentially become a 2D parameter problem (a and b). Therefore, if we solve equation(7.22) over a range of a and b, any density can be found by interpolating equations (7.23) and (7.24) over the required ranges of x and r and for specified T and μ.

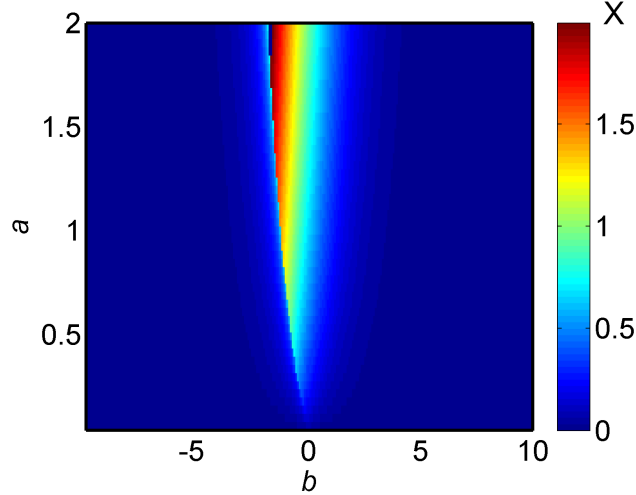Figure 7.2: Colour map showing the solutions to the transcendental equation (7.22) for a range of a and b. X is relatively small and smoothly varying over most values a and b. However, the sharp drop for some negative b requires careful interpolation.

Figure 7.2 shows, the solutions to the transcendental equation (7.22), X, found numerically, over a range of $0 < a < 2$ and $-10 < b < 10$. This

reveals that X is relatively small and smoothly varying over most values of a and b. For some negative b there is a sharp drop which will require careful interpolation. Note that there are typically two solutions to equation (7.22). However, for the purposes of finding the thermal cloud density, we require only the lowest value solution.

7.3   Comparison of Methods
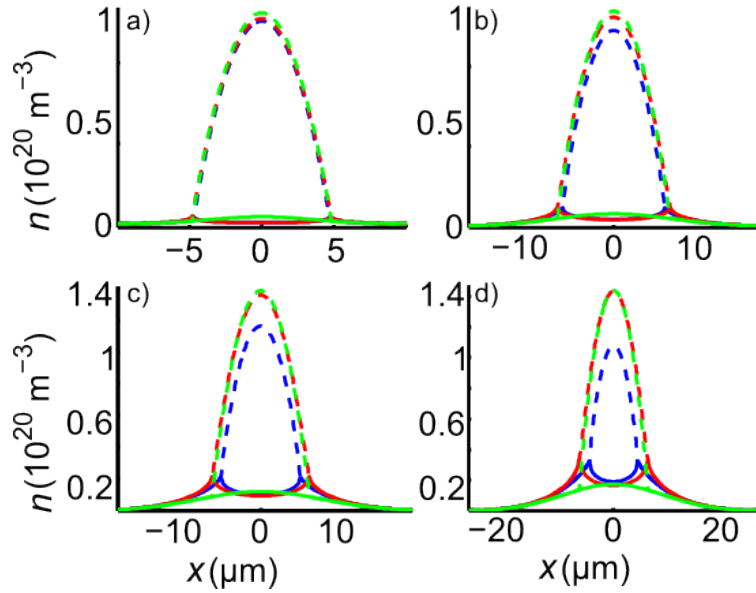
Figure 7.3: Comparison of atom densities calculated for a cylindrical trap of $\omega_r = 2\pi\ 200$ Hz, $\omega_x = 2\pi\ 100$ Hz, taking $\mu = 5\hbar\omega_r$, with $T =$ a) 50, b) 100, c) 150 and d) 200 nK, along the line $(x, r = 0)$. Total (dashed lines) and thermal cloud (solid lines) densities for the ideal gas (green), semi-ideal (red) and HF (blue) models.

Figure 7.3 shows the total (dashed lines) and thermal cloud (solid lines) densities for the ideal gas (green), semi-ideal (red) and HF (blue) models, in a cylindrical trap with $\omega_r = 2\pi\ 200$ Hz, $\omega_x = 2\pi\ 100$ Hz and $\mu = 5\hbar\omega_r$ with $T =$ a) 50, b) 100, c) 150 and d) 200 nK, along the line $(r = 0, x)$. The ideal and semi-ideal densities appear to agree well, which is largely due to the identical TF condensates used in both models. However, at higher temperatures (as

shown in c) and d)) they disagree at the edge of the condensate, $x \approx \pm 5$ μm, because the thermal cloud is repulsed by the condensate in the semi-ideal model, whilst maintaining its Gaussian shape in the ideal model. However, figure 7.3 reveals that, even at the relatively low temperature of 100 nK, the Hartree-Fock density differs from the ideal and semi-ideal models. This is because the presence of any thermal cloud partially depletes the condensate, reducing the total density across the entire distribution, but most notably at the peak ($x = 0$). This depletion of the condensate also gives rise to a smaller condensate width. In the case of the ideal and semi-ideal models, the condensate maintains the same width for all temperatures as the chemical potential is kept constant. This is not the case for the Hartree-Fock result, in which the BEC becomes narrower with increasing temperature. This effect will be discussed in detail in the next section.

Lastly, figure 7.3 shows that at large distances from the centre of the trap, $|x| \gtrsim 15$ μm, all three models agree well for all temperatures. These "Maxwell-Boltzmann tails" are due to the dominance of the thermal distribution of atoms in the trap, with no perturbing effects such as atomic repulsion or Bose-enhancement. In this region the relative change in the density, $\frac{1}{n}\frac{dn}{dx}$ can be used to extract the temperature:

$$T \approx -\left\langle \frac{m\omega_x^2 x}{k_B} \left[\frac{1}{n}\frac{dn}{dx}\right]^{-1} \right\rangle_x , \qquad (7.26)$$

where n can be the volume, area or line density, as the Gaussian form makes the density entirely separable.

The limit of this region can be quantified, as it requires that the first term of the summation in equation (7.22) be much larger than the rest of the sum. For this to occur, we require:

$$e^{-\left(\frac{U-\mu}{k_B T}\right)} \gg e^{-2\left(\frac{U-\mu}{k_B T}\right)}/2^{3/2}. \qquad (7.27)$$

Then, using the bi-modal description of the thermal density, it is straightforward to show that the region in which all the models agree is given by:

$$-\frac{x}{n}\frac{dn}{dx} \gg 3\log(2). \qquad (7.28)$$

For the parameters given above, the left hand side of this inequality is $\approx$ $5 \times 3\log(2)$ at the distance $|x| = 15$ μm and so agrees with the results in figure 7.3. Equations (7.26) and (7.28) are useful for extracting the temperature

from experimental absorption images of a cloud, largely because they depend on the relative gradient of the cloud. This removes the necessity of finding the absolute density from absorption images (using complex relations of imaging beam power, absorption rates and saturation densities) and so allows the temperature to be extracted from "raw" data without knowing the chemical potential or any information other than a single trap frequency.

7.4 Thermal Suppression of the Condensate

As discussed above, in the Hartree-Fock model, the presence of the thermal cloud acts to deplete the condensate due to accurately taking into account their mutual repulsion. For both the semi-ideal and Hartree-Fock thermal clouds, the peak thermal density is found when the exponent in equation (7.22) goes to zero, which occurs at the edge of the condensate (the point of lowest effective potential). At this point we can find an analytical solution to the transcendental equation (7.22), but only for the unwanted, larger valued, solution. In the limit of small T, though, the two solutions become approximately equal, which enables us to calculate the peak thermal cloud density:

$$n_{th,0} \approx \left(\frac{mk_BT}{2\pi\hbar^2} \right)^{3/2} \zeta\left(3/2\right), \qquad (7.29)$$

where $\zeta(3/2) = 2.612$, is the Riemann zeta function. Then, by substituting this into the TF condensate relation and setting the density equal to zero, we can obtain a value for the radius of the condensate under the effects of a thermal cloud:

$$x_{HF} = \sqrt{\frac{2(\mu - 2gn_{th,0})}{m\omega_x^2}}, \qquad (7.30)$$

where we have defined x_{HF} as the Hartree-Fock radius of the condensate.

Figure 7.4 shows the radius, x_c, of a condensate in the trap described above, calculated versus temperature. The total atom number, $N_{tot} = N_c + N_{th} = 20 \times 10^3$, was kept constant by varying the chemical potential. For $T/T_c \gtrsim 0.5$ there is a sizeable shift from the TF condensate radius, shown by the numerical solution of equation (7.22) (solid blue line). The analytic
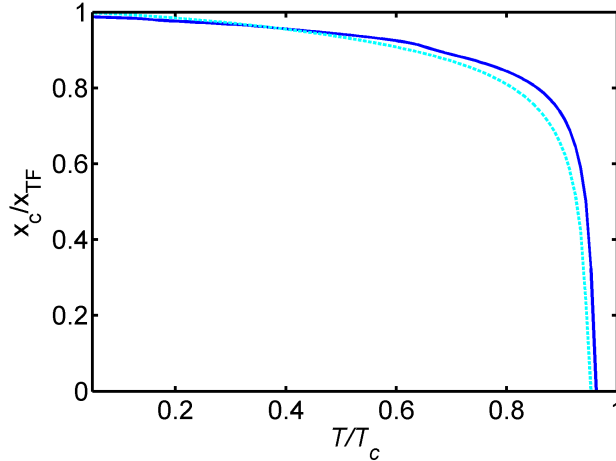
Figure 7.4: Condensate radius versus temperature for a constant atom number (parameters given in text). The full numerical solution of equation (7.22) (solid blue curve) agrees well with the analytic approximation (light blue dashed curve). Whilst the difference between the two curves is only sizeable for $T/T_c \gtrsim 0.5$, this effect has been seen in experiment [114].

approximation (light blue dashed line), given by equations (7.29) and (7.30), agrees well, though it over-estimates the thermal 'squeezing' around T_c.

At low temperatures this effect may be small, but it is still large enough for temperature dependant condensate compression to have been previously been observed experimentally [114]. Similarly, attempts to calculate and quantify the compression have previously been made [115]. However, to our knowledge, this is the first time that a solution has been found which takes into account all the relevant scattering processes in the HF equations and has a reasonable analytic approximation.

An interesting feature shown in figure 7.4, is the complete depletion of the condensate ($x_c = 0$) for temperatures $T \sim 0.95\,T_c$, due to the thermal cloud suppressing the condensate. The value of T_c was found by setting $\mu = 0$ (i.e the point at which the groundstate becomes energetically accessible) and calculating the total number of atoms for a given temperature.

However, figure 7.4 reveals that the assumption that condensation occurs at $\mu = 0$ is no longer valid. Instead, equation (7.30) predicts that condensation occurs when the chemical potential reaches:

$$\mu_c = 2gn_{th,0}. \tag{7.31}$$

Figure 7.5 shows the chemical potential required to allow $x_{HF} > 0$, found numerically (solid dark blue curve) and via the analytical approximation (dashed, light blue curve) given in equation (7.31). Again, the approximation appears accurate for low temperatures and only diverges significantly for very large temperatures. Physically, this requirement of a larger chemical potential to begin condensation is explained by the self-repulsion of the thermal cloud ensuring that the total effective potential doesn't drop to below the chemical potential. Therefore no atom can have an energy low enough to enter the condensate mode. This is an interesting effect that is yet to be observed experimentally. However, detailed analysis of this effect requires an independent method to calculate the chemical potential, as simply fitting the data to the HF model does, of course, assume that the effect occurs.
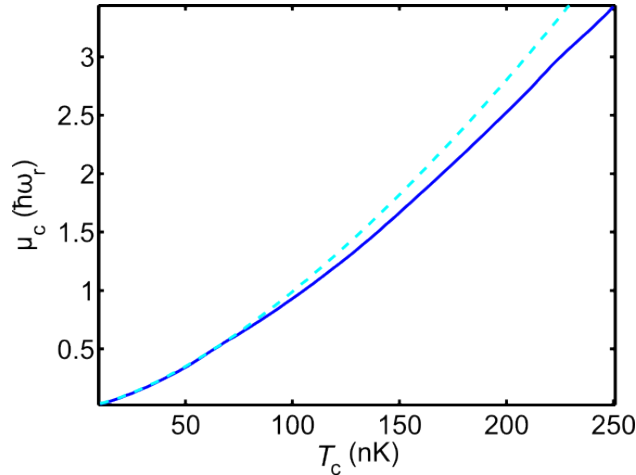
Figure 7.5: Chemical potential required for the onset of Bose-Einstein condensation in the presence of thermal-thermal interactions, found numerically (blue curve) and via the analytical approximation (dashed, light blue curve). This reveals that the atom cloud phase-density, suppressed due to atomic repulsion, requires a larger chemical potential in order for the cloud to begin populating the groundstate.

Alternatively, the effects of thermal cloud repulsion can be seen via sizeable shift in the critical temperature. Figure 7.6 shows the critical temperature calculated for a given atom number for the ideal or semi-ideal model
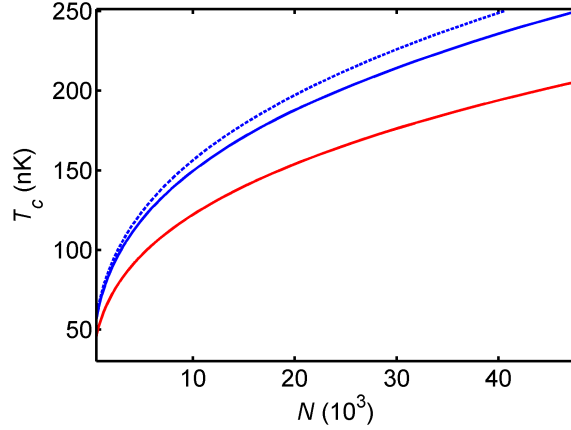
Figure 7.6: Critical temperature calculated for a gas of ^{87}Rb atoms in the trap discussed above. The curves result from the ideal gas model (red, identical to the semi-ideal model) and HF model by setting $\mu = 0$ (dashed blue) and the HF model with finite μ (solid blue). The inclusion of self-interaction in the HF models requires a larger chemical potential, for a given atom number and temperature, leading to a decreased critical temperature.

(red), found by setting $\mu = 0$ and calculating the total number of atoms for a given temperature. Alternatively, figure 7.6 shows the critical temperature for the HF model (blue), calculated by setting $\mu = 0$ (dashed line) and also by using the finite chemical potential required for condensation as shown in figure 7.5. The self-interaction of the thermal cloud in the HF models acts to increase the critical temperature by a large degree. This can be explained physically, as a cloud that experiences inter-atomic repulsion requires an increased chemical potential in order to produce a cloud of a given number of atoms. This pushes the chemical potential from negative to zero much faster with increasing atom number. This effect is slightly offset by the requirement of a larger condensation chemical potential, hence lower critical temperatures for the finite value μ results (dashed line) than the $\mu = 0$ Hartree-Fock results (solid line).

7.5   Conclusion

We have presented three models to described a gas of atoms at finite temperature. The ideal gas formula was shown to be simple to calculate, as it

119

ignores any coupling between the condensate and thermal cloud. However, due to conflicting approximations it is known to have sizeable inaccuracies. The semi-ideal model, which takes into account the thermal cloud interaction with the condensate was then derived. Whilst more complex than the ideal gas description, its analytical nature and increased accuracy makes it an attractive alternative for fitting of experimental densities.

Lastly, the Hartree-Fock model was described. Whilst needing more complex numerical techniques to solve, a simple method was shown that requires the solution of one transcendental equation over a range of two dimensionless parameters. Using this 2D array, the fully interacting thermal cloud and condensate can be calculated. Further, the results of the Hartree-Fock densities showed a sizeable deviation in the critical temperature and condensate width for temperatures, $T \gtrsim 0.5 T_c$.

This was accompanied by a suppression of both the thermal cloud and condensate density. An analytical approximation for the peak thermal cloud height was then used to quantify the condensate width suppression. The results revealed a shift in the chemical potential needed for the onset of condensation, to our knowledge a previously unseen phenomenon.

Chapter 8

Finite Temperature BECs: Quasi-1D Densities & Landau Damping

8.1 Quasi-1D Condensate

So far, in order to describe the condensate density we have used the Thomas-Fermi approximation. In addition, as in the last chapter, we have assumed a 3D trapping geometry, which requires the chemical potential to be much greater than the harmonic trap level spacing in all directions. Alternatively, as in chapter 5, we have used reduced dimensional condensates in 2D and 1D geometries, which require the chemical potential to be less than or equal to the groundstate trap energy in one or two directions, respectively. However, in this chapter, we will analyse an experiment in which the chemical potential typically sits inbetween the 1D and 3D requirements, and hence, shall be referred to as quasi-1D.

The experiment is described in detail in [112] and so we only describe the relevant details here. The trap is formed from a "noisy" trap potential created by a deviation in the wires used to create the trapping potential. This produces a tightly confined cylindrically symmetric trap that contains a small "dimple" at its centre.

Figure 8.1 shows the origin of this potential. Primarily created by a Ioffe-Pritchard trap constructed from a z-wire arrangement (red), as shown in figure 8.1 a), the current I, creates a magnetic field which is cancelled by the
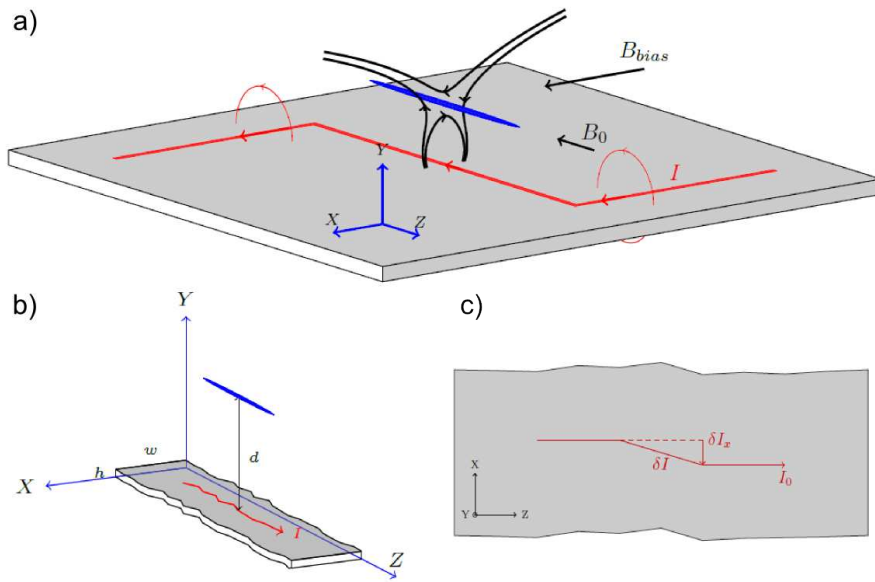
Figure 8.1: a) Schematic of a Ioffe-Pritchard trap created with a z-wire configuration. The DC current, I, produces a magnetic field which is cancelled by the addition of the bias field, B_{bias}, to create a trap potential (black curves). The presence of the field, B_0, increases the magnitude of the field at the trap minimum (as explained in chapter 1). b) schematic of the central z-wire section showing deviations in the wire, c) shows the presence of current streamline deviations, which cause fluctuations in the current, δI_x. This creates additional magnetic field components, $\delta B_z(z)$, which greatly alters the trapping potential. Figure adapted from [116].

bias field, B_{bias}, some distance above the wire, thus creating a quadrapole potential (black curves). The addition of the field B_0 increases the magnitude of the field at the potential minimum (as explained in chapter 1). Figure 8.1 b) shows the central section of the z-wire, which exhibits deviations from a straight line, c) then shows the resulting fluctuation in the current, δI_x, which creates spatially varying magnetic field fluctuations, $\delta B_z(z)$. This shifts the position at which B_{bias} negates the field from the wire and, hence, causes large deviations in the potential felt by the trapped atoms.

From experimental analysis [112], it is shown that the final potential can be roughly approximated by a harmonic trap with a dimple at its centre. The potential can be described analytically by:

$$U_{trap} = \frac{m}{2} \left(\omega_r^2 r^2 + \omega_o^2 z^2 + \delta(|z| < z_d)\omega_d^2 z^2 + \delta(|z| > z_d)U_d \right), \qquad (8.1)$$

where $\omega_r = 2\pi\ 1400$ Hz and $\omega_o = 2\pi\ 3$ Hz are the primary trap frequencies. The central dimple has a total trap frequency $\omega_z = \sqrt{\omega_o^2 + \omega_z^2} = 2\pi$ 10 Hz and width, $z_d = 100\ \mu$m. The energy offset, U_d, ensures that at the bottom of the dimple, $U(r = z = 0) = 0$.

Figure 8.2 shows the experimentally found trap potential (solid blue curve) and the smooth approximation (dashed, light blue curve). Whilst the experimentally found potential appears particularly "noisy", in that it contains a great deal of anharmonicity and asymmetry, the smooth approximation appears to give overall good agreement in the region $|z| < 200\ \mu$m, where the atoms are expected to be situated. The dimple in the centre of the trap is expected to hold the condensate, resulting in the thermal cloud being pushed out into the lower frequency regions of the trap.

Due to the depth of the dimple, $U_d \approx 3\hbar\omega_r$, even if the condensate were to entirely fill it, the requirement that $\mu \gg \hbar\omega_r$ would not be entirely fulfilled and so we would not have a 3D condensate. Instead, the experiments [112] routinely created condensates with $\mu \approx 2\hbar\omega_r$, which cannot be described by any Thomas-Fermi approximation and instead have to be modelled by numerical means. Similarly, the experiment produced atom clouds with a range of temperatures. To describe and simulate their behaviour, we therefore need a numerical scheme that will take into account thermal atom-condensate interaction in this dimensional cross-over regime.
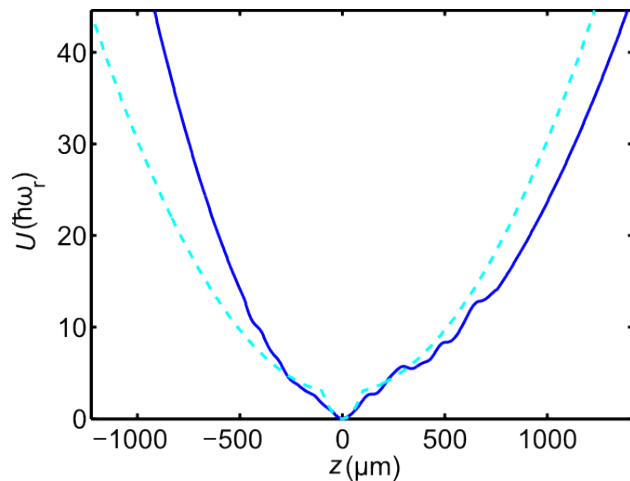
Figure 8.2: Experimentally measured "noisy" trap potential (solid blue curve) with smooth dimple approximation (dashed light blue curve), which approximately fits the central region ($|z| < 200$ μm) through the line $(z, r = 0)$ [112]. The condensate is expected to sit in the dimple with the thermal cloud pushed into the lower frequency wings.

8.1.1 The SPGPE

In order to accurately model the finite temperature condensate, we used the Stochastic Projected Gross Pitaevskii equation (SPGPE). This is an addition to the PGPE described in chapter 2. For a full derivation and description of the SPGPE, as well as many examples of its use, see [16]. Here, we focus on explaining the various terms in the SPGPE and describing their physical meaning.

Firstly, the PGPE is used to calculate a spatially varying, pseudo-chemical potential:

$$\mu_c(\mathbf{x}, t)\psi = \mathcal{P}\left[-\frac{\hbar^2}{2m}\nabla^2 + U + g|\psi|^2\right]\psi, \qquad (8.2)$$

where U is the total external potential felt by the condensate. Equation (8.2) is then used in the SPGPE:

$$i\hbar\frac{d\psi}{dt} = \mu_c(\mathbf{x}, t)\psi + iR_\gamma\left[\mu - \mu_c(\mathbf{x}, t)\right]\psi + \frac{dW}{dt}. \qquad (8.3)$$

Specifically, the first term on the right hand side describes the evolution

124

of the wavefunction in an identical manner to the PGPE. The second term on the right is a spatially varying complex quantity that allows the magnitude of the wavefunction to be altered in time. This attempts to match the local chemical potential, μ_c, with the global chemical potential, μ, over all space. The rate at which this occurs is given by:

$$R_\gamma = \frac{4ma_s^2 k_B T}{\pi \hbar^2} \gamma, \tag{8.4}$$

where γ is a small numerical factor calculated via equation (172) of [16]. The final term in equation (8.3) is randomly generated, complex, spatial noise, described by:

$$\langle dW^*(\mathbf{x}, t) dW(\mathbf{x}', t) \rangle = 2\hbar k_B T R_\gamma \delta(\mathbf{x}, \mathbf{x}') dt. \tag{8.5}$$

This acts to simulate the bombardment of the condensate by the thermal cloud. Its complex nature will also alter the magnitude of the wavefunction, incoherently adding or detracting from the condensate.

Due to the addition of the incoherent excitations in the condensate, the wavefunction, ψ, does not just describe the condensate but also includes all thermal atoms up to the energy cut off, ϵ_{cut}, described in chapter 2. Consequently, the ensemble described by the wavefunction shall be called the "coherent region" and so $|\psi|^2 = n_c$, the coherent field atom density, which $\neq n_0$.

The inclusion of some thermal atoms in the coherent field wavefunction must also be taken into account when calculating the density of the remaining thermal atoms. This is done via the limits of the momentum integration, to ensure that the minimum energy of the thermal atoms is $> \epsilon_{cut}$:

$$n_{th}(\mathbf{x}) = \frac{1}{2\pi^2} \int_{k_{cut}}^{\infty} \frac{k^2 dk}{e^{\frac{E(k,\mathbf{x}) - \mu}{k_B T}} - 1}, \tag{8.6}$$

where $k_{cut}(\mathbf{x}) = \sqrt{2m[\epsilon_{cut} - U_{trap}(\mathbf{x})]}/\hbar \, \delta(\epsilon_{cut} > U_{trap}(\mathbf{x}))$ and

$$E(k, \mathbf{x}) = \frac{\hbar^2 k^2}{2m} + U_{trap}(\mathbf{x}) + 2g\left[n_c(\mathbf{x}) + n_{th}(\mathbf{x})\right]. \tag{8.7}$$

The integral in equation (8.6) then produces an incomplete polylogarithm which requires a numerical factor to be added to the polylogarithms, which is fully explained in [16].

Self-interaction of the thermal cloud can be added in using an iterative scheme. The total external potential felt by the condensate is then given by: $U = U_{trap} + 2gn_{th}$. By including all self and condensate interactions for the thermal cloud we have created a numerical analogue of the full Hartree-Fock equations described in the last chapter. Lastly, in order to match the results of the experiment, U_{trap}, was taken to be the experimentally noisy potential rather than the smooth dimple approximation.

8.1.2 Fitting to Experimental Data

The temperature and chemical potential corresponding to various experimentally measured densities were then calculated by fitting the total density resulting from the SPGPE. The numerically determined densities have to be averaged for some time in order to smooth out the noise added by the final term of equation (8.3). These are then numerically integrated over the radial direction to create line densities. We then find the best fitting densities by using the χ^2 values, given by [110]:

$$\chi^2(T, \mu) = \sum_i \frac{[n_{exp}(x_i) - n_{SPGPE}(T, \mu, x_i)]^2}{\sigma_{exp}^2(x_i)}, \tag{8.8}$$

where σ_{exp} is the uncertainty in each data point, full details of which can be found in [112]. The temperatures and chemical potentials that give the smallest χ^2 value are then assumed to be the temperature and chemical potential of the cloud.

Figure 8.3 shows the experimentally measured line density (black points) and the total SPGPE density (dark blue line) that best fits the experimental data. This reveals that the cloud has a relatively large temperature, $T = 188$ nK ($\sim 70\%$ of the ideal gas critical temperature, 280 nK), and low chemical potential, $\mu = 1.05\hbar\omega_r$, which confirmed the condensate is in the quasi-1D regime and explains the large degree of noise in the experimental data points. Note the effect of the anharmonic region ($z \sim 200$ μm), which causes noticeable density fluctuations in the thermal cloud (red dashed curve). However, the high density condensate (light blue curve) still appears to retain a harmonic, inverse parabola, shape indicating that it is not greatly affected by the trap anharmonicities.

Additionally, as discussed in the previous chapter, self-interaction in the thermal cloud and the repulsion of the thermal cloud on the condensate
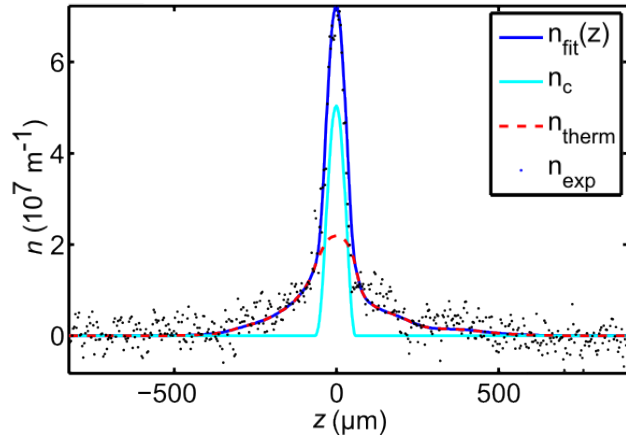
Figure 8.3: Experimentally measured line densities (black points, [112]) and best fit to the SPGPE calculations (dark blue curve) revealing the temperature, $T = 188$ nK, and chemical potential, $\mu = 1.05\hbar\omega_r$, confirming the cloud to be in the quasi-1D parameter regime. Note the effect of the trapping anharmonicities, which create density fluctuations in the thermal cloud (red dashed curve) in the region $z \sim 200$ μm. Conversely, the condensate still retains a harmonic, inverted parabola shape (light blue).

should only shift the found temperature and chemical potential by a small amount (less than 10%) and so we can omit this added complication from the fitting method.

Figure 8.4 shows a) the temperature and b) the chemical potential found with c) χ^2 values for atom clouds held for a range of times up to one second after the RF knife is switched off at $t = 9.4$ s. The increase in T shows heating from various sources, and gives an average heating rate of 80 nK/s, very similar to the measured 100 nK/s rate reported in [112]. The decreasing μ in figure 8.4 shows a large loss of condensate atoms as the atoms both heat up and leave the trap. Figure 8.4 c) shows the decreasing χ^2 over time, which is due to greater noise-to-signal ratios from an increase in thermal fluctuations and a decrease in atoms.

Lastly, from the parameters found in figure 8.4, the atom cloud created in the experiment are simultaneously in the quasi-1D regime (as $\mu > \hbar\omega_r$ at all times) and have a sizeable thermal component as T can vary over a range of nearly 100 nK around the critical temperature.

8.2 Condensate Shaking and Landau Damping

In the previous section we showed that the SPGPE can accurately model the quasi-1D regime and include all the relevant scattering events that are included in the Hartree-Fock model. This allowed us to calculate the experimental heating rate for a gas of atoms held in a magnetic trap.

The second part of the experiment in [112] was the excitation and damping of a centre of mass oscillation in the quasi-1D geometry. Firstly, the centre of mass excitation was carried out by shaking the trap in resonance with the dimple frequency, ($\omega_z = 2\pi$ 10 Hz). This resonance caused the condensate to oscillate with a sizeable amplitude (≈ 15 μm). During this excitation, the thermal cloud, which primarily inhabits the weakly trapped region ($\omega_o = 2\pi$ 3 Hz), remained relatively still due to the lack of resonance. This then allows the condensate to oscillate back and forth, through a stationary thermal cloud.

In order to simulate the atom cloud dynamics with the SPGPE, an additional term was added to the coherent field potential to simulate the shaking of the trap:
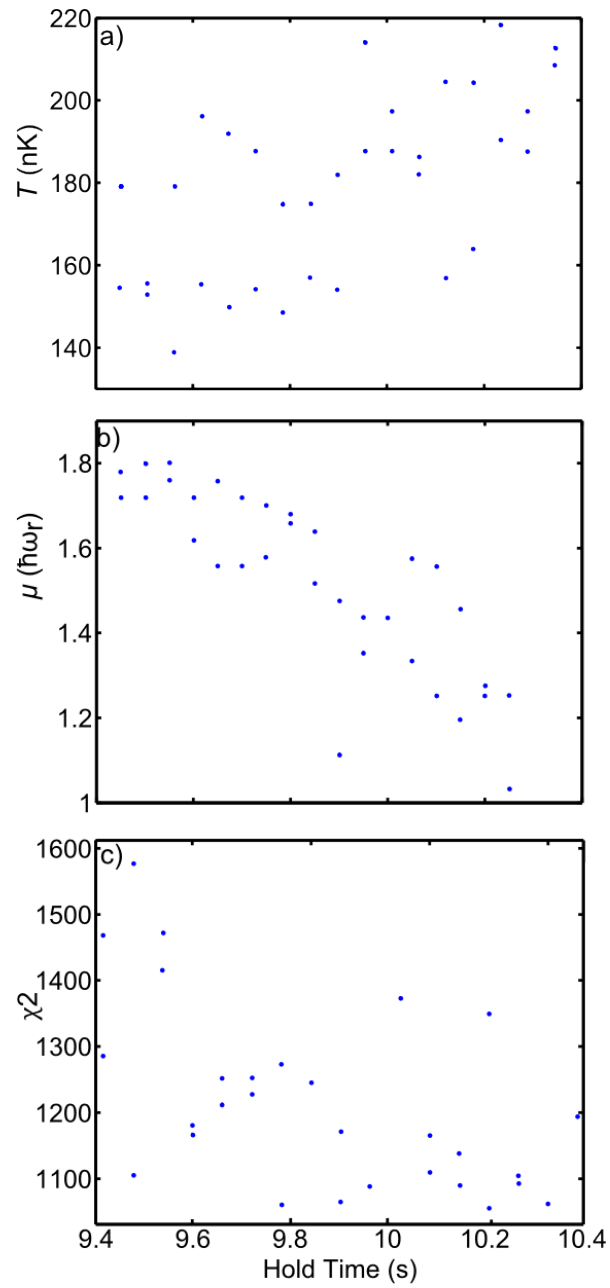
Figure 8.4: a) Temperature, b) chemical potential and c) χ^2 values calculated for clouds held for a range of times after the RF knife is switched off at $t = 9.4$ s. The increase in T with increasing time shows heating from various sources and the decreasing μ reveals a sizeable loss of the condensate. The decreasing χ^2 is due to greater signal-to-noise ratios from decreasing atom densities and increasing thermal fluctuations.

$$U = U_{trap} + 2gn_{th} + \frac{m\omega_z^2 \delta_s}{2} z \sin(\omega_s t)\, \delta(t < \tau_s), \qquad (8.9)$$

where $\omega_s = \omega_z$ is the shaking frequency, $\tau_s = 2\tau_z$ is the shaking period and $\delta_s = 4.67$ μm is the shaking amplitude, found to give the correct centre of mass oscillation for the mean temperature and chemical potential shown in figure 8.4.

The delta function ensures that this perturbation is applied for only two oscillation periods. After this the cloud was allowed to freely evolve and re-equilibrate.
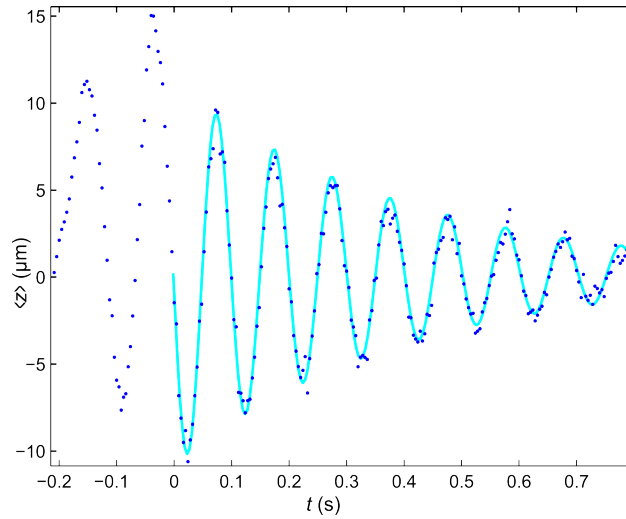
Figure 8.5: Centre of mass oscillation calculated for a cloud of 20,000 atoms at $T = 250$ nK, found using the SPGPE (dark blue points). The shaking potential gives a centre of mass amplitude of 15 μm with a resulting exponential decay rate of $\gamma_d = 2.5$/s (light blue curve) found by fitting equation (8.10).

Figure 8.5 shows the centre of mass of a high temperature ($T = 250$ nK) cloud, driven by the shaking potential for two oscillation periods and then allowed to freely evolve and re-equilibrate. The rate of this equilibration is found by fitting the free oscillation to the function:

$$\langle z \rangle_{fit} = z_o e^{-\gamma_d t} \sin(\omega_z t), \qquad (8.10)$$

130

where z_o is the initial amplitude of the oscillation and γ_d is the exponential rate of decay. This excitation and damping was then repeated for a range of temperatures and chemical potentials.
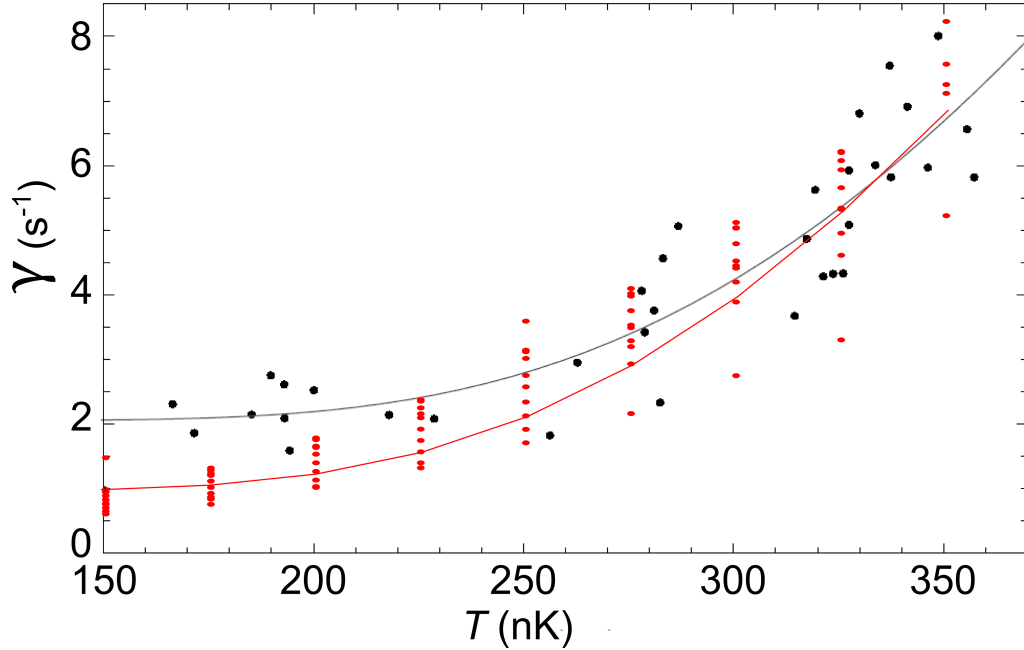
Figure 8.6: Damping rates for a range of temperatures and chemical potentials (as described in the text), for experimental densities (black points) and SPGPE results (red points). Curves give the best fit for the modified Landau damping equation given in section 8.2.1.

Figure 8.6 shows the damping rates found experimentally (black points) and from the SPGPE results (red points) for a range of temperatures $T = 150$ to 350 nK and chemical potentials of 1 to 2 $\hbar\omega_r$ (shown as a vertical distribution of points, with decreasing chemical potential from bottom to top). The theoretical curves show the best fit for the modified Landau damping equation given in section 8.2.1. In general the two data sets (experimental and simulated) show strong correlation, especially at higher temperatures. However, at low temperatures the simulation results predict a damping rate that tends towards zero as T decreases. By contrast, the experimental results show the damping dropping to a constant rate of ≈ 2/s. It is reasonable to assume that the same causes of the 80 nK heating rate, shown in the previ-

131

ous section, would also cause additional damping that would be independent of the temperature of the trapped atoms, which would explain the larger damping at low temperatures.

This additional heating could be included in the SPGPE model by slowly increasing the temperature and decreasing the chemical potential (in order to conserve atom number). However, as the thermal cloud is always treated as being at or near equilibrium this would to first approximation simply cause a temperature shift to results given above. A more detailed analysis would require a non-equilibrium description of the thermal cloud and a detailed description of the source of the heating.

8.2.1 Damping in a Confined Trap

We now give a brief explanation of the Landau damping model described in [112]. If we consider the condensate as a superposition of N_0 atoms in the groundstate, $n = 0$, and there are N_q atoms in a collective excitation state, with energy $\epsilon_q = \hbar\omega_q$. Then if we approximate $\epsilon_0 = 0$, the total energy of the oscillation is simply, $E_q = N_q\hbar\omega_q$.

The rate at which the collective oscillation loses energy is then:

$$\frac{dE_q}{dt} = -\hbar\omega_q \left(W^{(a)} - W^{(e)}\right), \tag{8.11}$$

where $W^{(a)}$ is the rate at which excited atoms decay into the groundstate and $W^{(e)}$ is the rate of the reverse (excitation) process.

To find these rates we must consider the nature of the collisions in the gas. In the experiment [112], this primarily occurs between the oscillating condensate and the stationary thermal atoms. Therefore, damping of the coherent motion will take place when an excited atom collides with an atom of the thermal bath and decays into the groundstate. From first order time-dependant perturbation theory, the rate of these collisions is given by:

$$W^{(a)} = \sum_{ik} \frac{2\pi}{\hbar} |A_{qi,0k}|^2 N_q N_i \, \delta(\epsilon_k - \epsilon_i - \hbar\omega_q), \tag{8.12}$$

where $A_{qi,0k}$ is the transition matrix element, given by the overlap integral of all possible collisions between atoms in levels q and i producing atoms in the groundstate 0 and some thermal state k (see equation (8.4) of [112] for more details). The delta function ensures that this collision conserves energy.

Again, as we are assuming the thermal cloud to be in equilibrium, the population of the incoming thermal atoms, N_i, is given by the Bose-Einstein distribution:

$$N_i = f(\epsilon_i) = \frac{1}{e^{\frac{\epsilon_i - \mu}{k_B T}} - 1}, \tag{8.13}$$

where the density of states is taken to be unity as degenerate states will be taken into account in the sum in equation (8.12).

Of course the reverse process can also occur, where a collision with the thermal atom excites an atom from the groundstate to the excited state. The rate of which is given by a similar expression to that in equation (8.12):

$$W^{(e)} = \sum_{ik} \frac{2\pi}{\hbar} |A_{ik}|^2 (N_q - 1) N_k \, \delta(\epsilon_k - \epsilon_i - \hbar\omega_q). \tag{8.14}$$

Then substituting the rates, $W^{(a)}$ and $W^{(e)}$, into equation (8.11), we obtain:

$$\frac{dE_q}{dt} = -2\pi\omega_q \sum_{ik} |A_{ik}|^2 N_q [f(\epsilon_i) - f(\epsilon_k)] \, \delta(\epsilon_k - \epsilon_i - \hbar\omega_q), \tag{8.15}$$

where we have approximated $N_q - 1 \approx N_q$ because the number of atoms initially in the coherent oscillation will be large.

The rate of energy loss and the damping of the collective oscillation are then related by:

$$\frac{dE_q}{dt} = -2E_q \gamma_d, \tag{8.16}$$

where the factor of 2 appears because, $E_q \sim \langle z \rangle^2$. Combining equations (8.15) and (8.16) produces the damping rate equation:

$$\gamma_d = \pi\omega_q \sum_{ik} |A_{ik}|^2 \frac{\partial f(\epsilon)}{\partial \epsilon}\bigg|_{\epsilon_i = 0} \delta(\epsilon_k - \epsilon_i - \hbar\omega_q), \tag{8.17}$$

where we have approximated $[f(\epsilon_i) - f(\epsilon_k)]/\hbar\omega_q$ as a differential, since $\hbar\omega_q \gg k_B T$.

Note that equation (8.17) is entirely general for any excitation in a Bose-Einstein condensate coupled a thermal gas. We have not needed to state the geometry, or even the nature of the excitation, or the value of ω_q.

133

To proceed, however, we shall make some assumptions. Firstly, for the experiments carried out in [112], $k_B T \gg \mu$. From this it can be shown that equation (8.17) can be approximated by [117–119]:

$$\gamma_d = \frac{3\pi}{8} \frac{k_B T a_s k_q}{\hbar},\tag{8.18}$$

where $k_q = \sqrt{2m\epsilon_q}/\hbar$ is the wavevector of the collective oscillation.

However, this expression predicts that the damping rates seen in figure 8.6 should be $\sim 50/s$ - $150/s$. Looking at the measured damping rates (black points) in figure 8.6 it is clear that there is a large difference between this prediction and that found in both the experiment and the SPGPE numerical simulations. The authors of [112] state that this is due to the momentum conservation that is used to calculate A_{ik} in equation (8.12) [117–119]. In order to calculate the overlap integral of all states involved in the collisions, the atoms are treated as plane waves with a discrete set of wavevectors in a homogeneous box of width L. These wavevectors are then approximated by a continuous spectrum in order to produce the simple analytical result in equation (8.18). In order to do this, the thermal cloud is assumed to be an infinite bath of atoms of constant density, by taking $L \to \infty$. As shown earlier in section (8.1.2), this is simply not the case as the thermal cloud very quickly changes in density, especially in the region around the condensate, in which most of the collisions will occur.

Secondly, this infinite bath approximation doesn't take into account the inhomogeneous nature of the trap. The large aspect ratio of the trap (approximately 1:140) results in a thermal cloud that can be approximated as a thermal continuum in the loosely trapped direction (as $k_B T \gg \hbar\omega_z$) but cannot easily be treated in the tighter directions (where $k_B T \sim \hbar\omega_r$).

Taking this into account, the authors of [112] produced a simple approximation which uses the first, lowest energy, term in equation (8.17) and approximates the energy of the thermal particles involved in this collision as:

$$\epsilon_i = \frac{1}{2m}\left[\left(mc - \frac{\hbar k_q}{2}\right)^2 + \left(\frac{\hbar\pi}{l_r}\right)^2\right]^2,\tag{8.19}$$

where $c = \sqrt{\mu/m}$ is the speed of sound in the gas and $l_r = \sqrt{\hbar/m\omega_r}$ is the radial oscillator length. For the experiment, $\epsilon_i = 2\pi\hbar\,10$ kHz.

This simple approximation produces a temperature-dependent damping relation:

134

$$\gamma_d = a + \frac{b}{T} \sinh^{-2} \left(\frac{\epsilon_i - \mu}{k_B T} \right) \tag{8.20}$$

where a, b and ϵ_i are parameters that were found by fitting the damping rates given in figure 8.6. The first term, a, is used to offset the finite damping that appears in the experiment at low temperatures, b is used to estimate the transition matrix elements, A_{ik}, and the value of ϵ_i gives a measure of the agreement between the quantised theory used to produce equation (8.19) and the experimentally measured damping rates.

Figure 8.6 shows the curves of best fit for equation (8.20). Experimentally, the value of $\epsilon_i = 2\pi\hbar$ 40 kHz (black curve), is only a factor of 4 away from the approximate theoretical value, whilst the SPGPE simulation results (blue curve) give $\epsilon_i = 2\pi\hbar$ 20 kHz, very similar to the predicted value, with only a factor of 2 difference. However, the functional forms of both theory curves show remarkable agreement with the data.

8.3   Conclusion

In this chapter we have used the SPGPE to numerically produce equilibrium density distributions in a quasi-1D regime where analytical descriptions can't be used. This allowed a complete Hartree-Fock model to be used to take into account condensate-condensate, thermal-thermal and thermal-condensate collisions. The equilibrium densities were then used to find the temperature and chemical potential for a range of experimentally measured atom density profiles that were obtained as the cloud was heated by various incoherent sources.

The SPGPE was then used to model dynamical behaviour in the condensate. Using the nature of the dimple trap, the condensate was driven into a centre of mass oscillation by a shaking of the trapping potential that was resonant with the dimple frequency. This allowed the condensate to oscillate through a non-driven, equilibrium thermal cloud. Collisions between the two then caused a damping of this motion.

The SPGPE gave similar decay rate values to those found experimentally, especially for higher temperature clouds where incoherent heating in the experiment had a smaller effect. These rates were shown to disagree with those predicted by Landau damping in a homogenous gas. However, it was shown that by using a theory that included quantised momentum states in

the tightly confined direction for the thermal gas, a much improved model for the damping could be created. Using this simple model, the experimental and numerical results were shown to be only a factor of 4 and 2, respectively, from the predicted values for the damping rates, with good agreement between the measured and calculated functional variation with temperature.

These results show that the SPGPE is a relatively simple addition to the PGPE used previously, which allows for the accurate simulation of finite temperature effects and equilibration in ultra-cold gasses.

Chapter 9

Summary and Outlook

9.1 Atom Dynamics in Optical Lattices

There has been much investigation of the interaction of atomic clouds in spatio-temporal potentials such as optical lattices. This has lead to great understanding of atom dynamics as they undergo Bloch oscillation, chaotic motion, and transport through complex potential landscapes [22, 25–33].

In chapter 3, we take previously known non-KAM (or "non-standard") chaos theory from semiconductor physics and apply this to a far cleaner system comprising an atom cloud held in a harmonic trap under the influence of a moving optical lattice that produces a travelling wave potential. We show that the classical theory agrees well with our semi-classical Projected Gross-Pitaevskii Equation (PGPE) model of the atom evolution.

We then show that the theory allows accurate control the excitation of the atoms by varying the wavelength of the travelling wave potential. This control endures even in the presence of atom-atom interactions with provide a complex, anharmonic potential.

In chapter 4, we then find that we can use this control to excite non-interacting groundstate atoms into any single quantum harmonic oscillator (QHO) state and can, similarly, controllably de-excite atoms from any single state back to the groundstate. Whilst this type of excitation has previously been shown experimentally, it required a complex experimental procedure using a non-harmonic trap and a complex numerically optimised shaking of the potential to excite atoms into only the first excited state with limited success.

However. our single level technique is shown to break down for the controlled creation of superpositions, wherein we attempt to occupy multiple different QHO states. Instead, we use a genetic algorithm to find the optimal set of optical lattice parameters to create a required superposition. Using this method, we show that it is possible to create superpositions of QHO states such as coherent states and even cat-states in the form of a superposition of two coherent states. However, it remains an open question as to whether this is a true many-body cat state or simple a superposition of single particle states. If it is the former, then this method would be the first to allow the controlled creation of a macro-scopically occupied cat state.

The level of control allowed in this system opens up a great plethora of new avenues of investigation. Chiefly, this controllable atom excitation and de-excitation allows for a great many quantum computational operations to be carried out such as entangled state generation, state-storage, atom transport and super-fast quantum gates [126–129]. More simply, there could also be the possibility of using this method to cool thermal ensembles of atoms down to condensate temperatures [130] or even applications in areas such as laser-pulse shaping to control reactions in quantum chemistry [131].

9.2 Coupling Atoms to Surfaces

The interaction between atom clouds and the structures that are used to hold them is an increasingly studied area as the creation and exploitation of cold atom gases increases. Whilst the theoretical understanding of the intrinsic Casimir-Polder force that couples the trapped atoms and the nearby surface atoms appears to be well known [70, 72, 74] the experiments that have investigated the interaction have been limited to qualitatively showing the existence of the interaction and its negative effect on the lifetime of the atom cloud [72, 74, 86].

In chapter 5 we quantitatively analyse the lifetime of atom clouds held in 1D and 2D harmonic traps near three different materials (silicon, silicon-nitride membranes and graphene). We show that the lifetime is dominated by the trap-surface separation and the trapping frequency in the direction of the surface. Due to three-body losses, we find that both the material of the surface and the initial number of atoms has relatively little (though still quantifiable) effect on the lifetime. Secondly, 2D harmonic traps (wherein the atoms are confined to the QHO groundstate in the surface direction of

the trap) were shown to allow much closer surface-trap separations because the more tightly confined 1D traps (wherein two of the three dimensions are confined to the QHO groundstate) showed larger three-body losses.

The results we present also show that there is no "optimum" trap geometry or surface separation for an atom cloud. Instead, it appears that for any surface separation there is a trap frequency that will allow a given lifetime. However, for current harmonic traps (typically limited to tens of kHz), we show that atoms clouds can have experimentally useful lifetimes of tens of milliseconds for atom surface distances of only hundreds of nano-metres.

These results show that a great range of further experiments are possible, which allow atoms to be held very close to surfaces which would greatly increase the resolution (and so the applicability) of cold atom microscopy. This also allows for further reduction in both the size of cold atom experimental apparatus which would also likely present a reduction in the power consumption of these devices. These are both useful advantages when attempting to take a table-top experiment and produce a mobile, rucksack sized sensing device, as is currently being considered.

Building on these stationary results, in chapter 6, we examine an experiment wherein a cold atom cloud is held near a microscopic cantilever that is driven into oscillation via a piezo-electric crystal [72]. By matching the cantilever oscillation frequency with the frequency of the atom trap in the direction of the surface, the experimentalists show that Casimir-Polder interaction can dynamically couple the two systems. However, they also show that as with stationary surfaces, the atoms have lifetimes greatly limited by the proximity of the attractive surface. They go on to show that the loss of atoms from the trap leads to contamination of the surface and a greatly increased Casimir-Polder attraction, leading to even greater atom losses. This effect has led the experimentalists to consider alternative coupling methods for cold atoms and microscopic devices [70].

Using our previous near-surface results, we show that the interaction between a cantilever and the atoms can be sufficient to allow strong dynamical coupling whilst also affording very long lifetime. We achieve this taking the same system as that investigated in the the previous experiment and rotate the atom trap relative to the cantilever. This allows us to resonantly couple the cantilever motion and the parallel motion of the atoms along the length of the cantilever. The trap frequency in the direction of the surface then no longer needs to be resonant with the cantilever motion and so can be greatly increased, allowing for a reduced cantilever-trap separation

and so greatly increased Casimir-Polder coupling.

We show that this simple alteration of the experiment design increases the coupling to the extent that the nanometre-scale thermal oscillations of the cantilever (i.e. oscillations due to thermal phonons at room temperature, without the additional driving of the piezo-electric crystal) is enough to drive large scale excitation of the trapped atoms. We go on to show that the energy increase in the atoms, in this un-driven, energetically constant, system is large enough to begin cooling the cantilever.

We stop short of showing the effects of cooling cantilever as the non-equilibrium oscillation of the cantilever requires a more complex model than the classical damped, driven oscillator model that we have considered and, as such, this remains open for further investigation. The aim would be to consider methods which allow the near complete cooling of the cantilever to its quantum-mechanical groundstate, which, we have shown, could be possible. If this were realised then the atom cloud could be used as an intermediary device to control the quantum state of the cantilever, which would then be one of the largest macroscopic devices to be placed into a defined quantum state.

9.3 Describing Finite Temperature Gases

The next topic we investigate is the semi-classical phase-space density distribution of finite temperature clouds of bosonic atoms. Whilst there are a great deal of theoretical methods to describe the distribution of these atomic ensembles [16], the complexity of many of them leaves them relatively unused in typical cold atom experiments. Instead experimentalists often limit their description of a trapped finite temperature gas of atoms to just the simplest ideal gas model.

In chapter 7, we discuss how this simple model will contain sizeable errors due to the contradictory approximations used in its application. We then go onto describe the relatively unknown semi-ideal gas model [111]. We show that as this takes into account the bosonic nature of the atoms as well as approximating the interaction between excited atoms and those in the cold, dense, groundstate, the previous contradictory assumptions are no longer needed, leading to a more accurate description of these experimentally realistic atom clouds.

Building on this work, we take the Hartree-Fock equations which include

all the necessary interactions between a thermal ensemble of atoms and we show that we can solve for the spatial distribution of the entire atom cloud. This requires numerically solving a general transcendental equation, which then allows a cloud at any experimentally reasonable temperature and occupation to be well described. We show that the results of this method show an interesting effect, in that when cooling a high temperature cloud down to condensate temperatures, the position of the condensate phase-transition (μ changing from negative to positive) is positively shifted (i.e. μ must become finitely positive) due to the repulsive nature of the atom-atom interactions. Although the exact magnitude of this shift requires the numerical solution of the previously mentioned transcendental equation, we can make a reasonable approximation which allows this shift to be given analytically. Whilst similar to previous ideal gas corrections, this shift is the first to be calculated that takes into account the trapping geometry, finite temperature as well as the atom-atom collisional interactions.

As of June 2015, this theoretical description of finite temperature atom clouds is currently in the process of being experimentally tested by the group of Lucia Hackermueller at the University of Nottingham. In the event of it being confirmed, this relatively simple, yet detailed, model will allow the thermodynamic parameters (chiefly temperature, chemical potential, total atom number and condensate occupation) of experimentally observed atom clouds to be found with much greater accuracy. By better knowing the state of an atom cloud, this model should allow for much greater optimisation of experimental cooling processes, leading to larger final atom numbers, lower temperatures and larger condensate occupations. This in turn should decrease experimental error and uncertainty due to thermal fluctuations and broadening often seen in cold atom experiments.

Lastly, in chapters 7 and 8, we consider a recent experiment in which a finite temperature atom cloud is produced in a trapping potential with a large aspect ratio (but which is not so extreme as to cause the cloud to exhibit 1D behaviour) and a central harmonic dimple which contains the coldest atoms [112]. The cloud is then excited by periodically shaking the potential in resonance with the dimple frequency. This then causes the cold atoms (assumed to be in the condensate mode) to oscillate with a sizeable amplitude, whilst the hotter thermal atoms which reside outside the dimple show little excitation. Once the shaking is halted the oscillation of the cold atoms is then seen to exponentially diminish. The experimentalists theorize that this occurs due to collisions between the moving condensate and the

stationary thermal atoms. They then show that the rate of this exponential damping differs from that expected of a typical 3D distribution of atoms [113], and so they use an altered theory to take into account the reduced dimensionality of the experiment. Their new theory is then shown to agree with the experimental results.

In chapter 8, in order to verify this theory, we use a finite temperature extension of our simpler PGPE model (known as the Stochastic PGPE model) which has previously been used with some success [16]. Firstly, we are able to show that, although the system cannot accurately be described by a 3D model, the SPGPE is able to produce spatial distributions of atoms in this dimple trap, which match those found experimentally, thereby validating the experimentally found values of temperature and chemical potential. Next, we are able to reproduce the excitation of the atoms due to the resonant shaking of the trap. This allows us to find similar damping rates of the condensate motion after the same periodic shaking. However, for low temperatures we find a divergence of the simulated and experimental data. This is explained due to a finite heating rate in the experiment which would cause an initially cold cloud to heat during the experiment, which would skew the low temperature data.

By producing results which closely match both the spatial density distribution of finite temperature atom clouds in this quasi-1D, anharmonic experimental system and also re-creating the same results as those expected by the quasi-1D damping theory, we have shown that the SPGPE is a suitable model to re-create experimental results in this non-typical system. Secondly the validation of the quasi-1D theory opens the possibility of studying further inter-atom dynamics in these previously unstudied trapping geometries.

Appendices

Appendix A

Gauss-Hermite Quadrature

A.1 Numerical Techniques Using Gauss-Hermite Quadrature

The interaction integral in the PGPE (2.18) must be solved every time step and hence could be very computationally costly. However, using Gauss-Hermite quadrature (GHQ), the integrand only needs to be summed over very few points to be accurately evaluated, allowing for a efficient evaluation of the integration.

GHQ solves integrals of the form:

$$I = \int_{-\infty}^{\infty} f(x)e^{-x^2}\,dx, \tag{A.1}$$

where $f(x)$ is a polynomial of order p. It does this using a weighted sum over the integrand evaluated at N specific points:

$$I = \sum_{i=1}^{N} w_i f(x_i), \tag{A.2}$$

where w_i are the weights for each point x_i. The integral will be entirely accurate if the order of the quadrature, m satisfies $m \geq (p+1)/2$.

The weights are given by the formula:

$$w_i = \frac{2^{m-1}m!\sqrt{\pi}}{m^2\left(H_{m-1}(x_i)\right)^2} \tag{A.3}$$

and the points (sometimes referred to as abscissae), x_i are the roots to the mth order Hermite polynomial $H_m(x)$. The full derivation of the weights and the points is not needed here. However, a good description can be found in [120].

The integrals we wish to evaluate don't immediately have the required Gaussian factor in the integrand, as they are of the form:

$$I = \int_{-\infty}^{\infty} H_n(x)H_{n'}(x)H_{n''}(x)H_{n'''}(x)e^{-2x^2}dx. \tag{A.4}$$

Therefore, we must use the co-ordinate transform $x_i \to x_i/\sqrt{2}$ along with $w_i \to \sqrt{2}w_i$. Note that we can also see that the maximum order integration will be 4 times the largest order mode, n. There is also the added complication of the requirement to carry out this integration in 3 dimensions, which can be done by the following series of matrix/tensor multiplications:

$$\begin{aligned} P &= \sum_{\alpha,\beta,\gamma} C_{\alpha,\beta,\gamma} h_\alpha H_\alpha(x_i) h_\beta H_\beta(y_j) h_\gamma H_\gamma(z_k) \\ &= \sum_{\alpha} h_\alpha H_\alpha(x_i) \sum_{\beta} h_\beta H_\beta(y_j) \sum_{\gamma} C_{\alpha,\beta,\gamma} h_\gamma H_\gamma(z_k), \end{aligned} \tag{A.5}$$

where i, j and k are the abscissae indicies in the x, y and z directions respectively. Defining:

$$Q = P|P|^2, \tag{A.6}$$

we finally obtain:

$$\begin{aligned} M_n &= \sum_{i,j,k} Q(x_i, y_j, z_k) h_\alpha H_\alpha(x_i) w_i h_\beta H_\beta(y_j) w_j h_\gamma H_\gamma(z_k) w_k \\ &= \sum_{i} w_i h_\alpha H_\alpha(x_i) \sum_{j} w_j h_\beta H_\beta(y_j) \sum_{k} w_k Q(x_i, y_j, z_k) h_\gamma H_\gamma(z_k). \end{aligned} \tag{A.7}$$

Additional Perturbations

Additional spatio-temporal perturbations can be included in the PGPE using a similar GHQ integral. If $U_{pert} = f(t)g(x)$ then:

$$S_n = \sum_{n'} C_{n'} \int_{-\infty}^{\infty} \phi_{n'}(x)\phi_n(x)g(x)dx$$

$$= \sum_{n'} C_{n'} \sum_i w_i h_n H_n(x_i) h_{n'} H_{n'}(x_i)g(x_i), \qquad (A.8)$$

where w_i and x_i are as described without needing any additional alteration as the integrand contains the Gaussian required for GHQ.

A.1.1 Avoiding Double Bit Precision Limits

The following is a computational solution to issues arising from using very large order basis states. This is not typically an issue, as the limit imposed by E_{cut} is often enough to ensure that all necessary numerical operations on the basis states can be carried out without issue. However, harmonic traps with extreme aspect ratios can often require large numbers of modes and high order modes. In this case, additional measures must be taken to calculate the integrand of equation (2.18) correctly.

The largest root of an nth order Hermite polynomial, $H_n(x)$ goes as $\sqrt{2n}$. As these roots are the abscissae, x_i, used in GHQ, $H_n(x_i)$ can often become much larger than the 10^{308} limit of the double precision number format. As this is often the largest format readily available in interpreted mathematical programming packages such as MathWork's MATLAB, this leads to an upper limit on the order of GHQ integrals that can be calculated.

There are a number of ways around this. Firstly, if a normalised Hermite polynomial is needed (henceforth referred to as hH_n), this can be found by multiplying the polynomial by the normalisation factor:

$$h_n = (\pi^{\frac{1}{2}} 2^n n!)^{-\frac{1}{2}}. \qquad (A.9)$$

As Hermite polynomials are often calculated via the recursion relation:

$$H_0 = 1; \ H_1(x) = 2x, \qquad (A.10)$$

$$H_{n+1}(x) = 2xH_n(x) - 2nH_{n-1}(x), \qquad (A.11)$$

the normalisation can be added inside the same recursive calculation. This is achieved by multiplying the latest term by the required normalisation

factor and storing it, before multiplying all previously calculated terms by the same normalisation factor. To begin this process, we note that:

$$hH_0 = \frac{1}{\pi^{\frac{1}{4}}}; \ hH_1(x) = \frac{2x}{\sqrt{2n}\pi^{\frac{1}{4}}}, \text{where } n = 1. \quad (A.12)$$

Therefore, after hH_0 has been saved it must be multiplied by the $\sqrt{2n}, n = 1$ term in order to calculate the 2nd and higher order polynomials, via:

$$hH_{n+1}(x) = \frac{2xhH_n(x) - 2nhH_{n-1}(x)}{\sqrt{2(n+1)}}. \quad (A.13)$$

Continuing, once the $hH_{n+1}(x)$ term has been stored, the previous terms must be re-normalised:

$$hH_{0:n}(x) \rightarrow \frac{hH_{0:n}(x)}{\sqrt{2(n+1)}}, \quad (A.14)$$

where the $0{:}n$ subscript denotes that all previous terms must have the same re-normalisation. This algorithm works as the $1/\pi^{\frac{1}{4}}$ constant included in the calculation of hH_0 and $hH_1(x)$ will ensure that all following terms are multiplied by the same constant and the $1/\sqrt{2n}$ term will recursively create $1/\sqrt{2^n n!}$, as required.

However, this will only allow the calculation of a few higher order Hermite polynomials before the same 10^{308} ceiling is hit. The solution to this issue is to instead calculate the natural logarithm of the Hermite polynomial (though the logarithm of any other sufficiently large base may be used). This can still be calculated using a recursion relation, the first two terms of which are:

$$\log(hH_0) = -\frac{1}{4}\log(\pi); \quad (A.15)$$

and

$$\log(hH_1) = -\frac{1}{4}\log(\pi) + \log(2x) - \frac{1}{2}\log(2n), \text{where } n = 1. \quad (A.16)$$

Again,

$$\log(hH_0) \rightarrow \log(hH_o) - \frac{1}{2}\log(2n), \text{where } n = 1. \quad (A.17)$$

However, the higher order terms are made more difficult due to the additive nature of the n and $n-1$ terms. Therefore, at least one exponential

must be used to return a non-logarithmic value. The solution is to ensure that this is as small a number as possible. There may be many different ways of carrying this out, though the following seems the simplest and most convenient.

Let

$$A = \log(hH_n) - \log(hH_{n-1}) - \log(n), \tag{A.18}$$

then

$$\log(hH_{n+1}) = \log(2xn) + \log(hH_{n-1}) + \log(e^A - \frac{1}{x}). \tag{A.19}$$

Again, $\log(hH_{0:n})$ will have to be renormalised as before. Now, as the exponential is of the ratio of hH_n to $n \times hH_{n-1}$ it will never be very large for any realistic order number, n. Though this allows the calculation of the logarithm of the normalised polynomial, it is still of no immediate use because to carry out GHQ the actual value of the Hermite polynomial must be calculated. The solution is found by noting that the weighting factor used in GHQ, given by:

$$w_i = \frac{2^{m-1}m!\sqrt{\pi}}{m^2[H_{m-1}(x_i)]^2} = \frac{1}{m[hH_{m-1}(x_i)]^2}, \tag{A.20}$$

(where m is the order of GHQ), must get proportionately smaller as $h_nH_n(x_i)$ gets larger because:

$$\sum_i^m w_i[h_nH_n(x_i)]^2 = 1. \tag{A.21}$$

Therefore, the value of $w_ihH_n(x_i)$ must never get prohibitively large. Using the simpler identity for the weight function, it is trivial to show that:

$$\log(w_i) = -\log(m) - 2\log(hH_{m-1}(x_i)). \tag{A.22}$$

This means that $\log(w_i)$ can be found in logarithm form because $\log(hH_{m-1}(x_i))$ can be calculated. Therefore:

$$Q_n(x_i) = w_ihH_n(x_i) = e^{(\log(w_i)+\log(hH_n(x_i)))}. \tag{A.23}$$

However, this is not a terrifically useful function because to carry out any GHQ in the PGPE, $hH_n(x_i)$ alone would still need to be calculated. Instead, the following function is more useful:

148

$$Q_n^{(2)}(x_i) = w_i^{\frac{1}{2}} h H_n(x_i) = e^{(\frac{1}{2}\log(w_i)+\log(hH_n(x_i)))}, \tag{A.24}$$

where the (2) represents how many times Q_n is used in the GHQ integration. Then:

$$\sum_i^m [Q(x_i)_n^{(2)}]^2 = 1. \tag{A.25}$$

For the integration required in the calculation of the effective potential in the PGPE the following function is required:

$$Q_n^{(4)}(x_i) = w_i^{\frac{1}{4}} h H_n = e^{(\frac{1}{4}\log(w_i)+\log(hH_n))}. \tag{A.26}$$

Then the overlap matrix (in 1D for simplicity) is given by:

$$G_n = \sum_i^m Q_n(x_i) \sum_\alpha^n C_\alpha Q_\alpha(x_i) |\sum_{\alpha'}^n C_{\alpha'} Q_{\alpha'}(x_i)|^2, \tag{A.27}$$

where C_α is the αth order expansion co-efficient, the maximum mode of which is n, and, again, m is the GHQ order, which is $\sim 2n$. Remembering that for this integral, $x_i \to x_i/\sqrt{2}$.

However, there are two issues that need to be addressed before this technique will work. Firstly, there are a number of places where the value $\log(x)$ must be calculated. This is usually trivial except for the fact that a GHQ integral of odd order will have $x_i = 0$ as an abscissa and so $\log(x_i = 0) = -\infty$. This is easily remedied by finding any abscissa that equal 0 and replacing it with something of the order of 10^{-308}. Making it essentially 0 but allowing the logarithm to produce usable values.

The next issue is the careful calculation of $w_i^{1/2}$ or $w_i^{1/4}$. As shown in equation (A.20), w_i is entirely positive and so $w_i^{1/2}$ and $w_i^{1/4}$ will be entirely real. However, $hH_{m-1}(x_i)$ can be negative, so:

$$w_i^{\frac{1}{2}} \neq e^{(-\frac{1}{2}\log(n)-\log(hH_{m-1}))}. \tag{A.28}$$

Instead, the following step must be used:

$$\log(hH_{m-1}) \to \frac{1}{2}\mathbb{R}[2\log(hH_{m-1})] = \mathbb{R}[\log(hH_{m-1})], \tag{A.29}$$

which is the logarithmic equivalent of:

$$|hH_{m-1}| = \sqrt{hH_{m-1}^2}. \qquad \text{(A.30)}$$

With the functions $Q_n(\sqrt{2}x_i)$, $Q_n^{(2)}(x_i)$ and $Q_n^{(4)}(x_i/\sqrt{2})$ it is then possible to carry out GHQ integrals to near limitless order.

A.1.2 Finding the roots of $H_n(x)$

If $hH_n(x_i)$ is too large to calculate then even finding the roots to begin with is an issue. The solution is to use a more drastic normalisation, whereby inside the recursion relation the latest term is divided by its absolute value to produce $hH_n(x) \pm 1$. The first two terms are then:

$$hH_o = 1; \quad hH_1(x) = \frac{2x}{|2x|}, \qquad \text{(A.31)}$$

and as before:

$$hH_o \rightarrow \frac{hH_o}{|2x|}. \qquad \text{(A.32)}$$

Higher order polynomials are found by using the usual relation:

$$H_{n+1}(x) = 2xH_n(x) - 2nH_{n-1}(x), \qquad \text{(A.33)}$$

except now:

$$hH_{0:n+1}(x) \rightarrow \frac{hH_{0:n+1}(x)}{|hH_{n+1}(x)|}, \qquad \text{(A.34)}$$

noting that all terms (including $n+1$) have been divided by $|hH_{n+1}(x)|$. Again, the trick in equation (A.34) lies in similarly re-normalising all previous terms so that the $n+1$ term can be calculated ensuring that it can never get larger than 1 in magnitude.

A convenient way of finding the position of the roots is to look at where the polynomial changes sign. This is done most easily by finding where the absolute difference between two points is equal to 2:

$$dH_n(x) = |hH_n(1 : n_x - 1) - hH_n(2 : n_x)|, \qquad \text{(A.35)}$$

where n_x is the length of the x array used. Note that a slight correction must be used as the actual point of the root will be somewhere between two points, and so:

$$x_i \rightarrow x_i - \frac{dx}{2} \tag{A.36}$$

where dx is the resolution in the x array used.

A technique often used for efficiency in the finding of roots is to proportionately 'home - in' on the root by linearly extracting the difference of $H_n(x)$ from 0 in order to calculate a series of exponentially closer values for the root. However, this technique isn't so efficient here as the procedure would have to be carried out for each order separately. However, the technique described above can be used to find the roots of all orders simultaneously, using a matrix method.

Appendix B

Genetic Optimisation Routine

B.1 Simple Genetic Algorithm

In order to solve complex, multi-variate, equations genetic algorithms have had much success [121, 122]. They work by utilising a similar method to biological evolution, in that by selecting out successful genomes to merge and create new genomes under the constant influence of stochastic mutation, some time later a maximally successful genome will be found. If we consider a list of variables to be used in a non-linear equation as an analogy of a genome that contains a list of 'instructions', then we can evolve the variables by setting some level of success for each set of variables (or 'genome') and evolving them in a numerical analogue of the biological evolution mechanism. Though there are many variations of the implementation of genetic algorithms (GA), they all hinge on three main steps, as discussed above:

- Selection of genomes based on some criteria.

- Crossover between surviving solutions.

- Addition of 'mutations'.

Each of these steps has a randomized element as explained later, therefore the algorithm is stochastic and can be thought of as quasi-ergodic in nature. This is because although the evolution of the genome evolves around solutions that are most 'survivable', which would destroy ergodicity (as after some time has passed the GA would have evolved the genome to some limited set of solutions). The stochastic element of the evolution will ensure that no one

set of solutions dominates (i.e. the system won't get infinitely stuck on one set of genomes). Instead, the GA will always be able to evolve around all of the available parameter space. Its ability to find solutions in a stochastic, probabilistic, way ensures that after an infinite length of time the GA will find the globally optimum genome.

The following is largely taken from the description in [123] where a simple example will be used to explain the method. A more detailed analysis can be found in [124].

Consider a relatively simple, multi-variate equation:

$$f(x) = a + 2b + 3c + 4d - 30 = 0 \qquad (B.1)$$

where we require all variables to be integers. We can find the solution by minimizing the absolute value of the function $f(x)$. The genome in this case is $x = a, b, c, d$ where a, b, c and d are known as chromosomes. We will then evolve a set of genomes in order to find a solution to $f(x) = 0$.

Initialization

Firstly, we start by initializing the algorithm. To do this a random selection of chromosomes are used to create an initial generation of genomes. However, care must be taken as the possible values of the selection will limit the 'search space' of the algorithm (as will the possible values allowed for mutations, explained later). For this case we will limit our 'search space' to integer values between 0 and 30 this satisfies our requirement that all variables be integers. As they all add positively to one-another, we know that 30 is a sensible upper limit to the possible solutions.

Selection

So, once we have a family of N genomes created, we can begin the series of three steps given above. Firstly, we calculate some objective function to measure the 'fitness' of each genome. In this example the fitness will simply be the value of $1/|f(x)|$, so the genomes that give the smallest value of $f(x)$ will be considered the 'fittest'.

Then we use a cumulative distribution of the fitness values, normalised to 1, i.e.:

$$C_i = \frac{\sum_{j=1}^{i} 1/|f(x_i)|}{\sum_{j=1}^{N} 1/|f(x_i)|}, \tag{B.2}$$

where $i = 1 : N$ and x_i are the set of N genomes. Then we use the cumulative probability function to probabilistically select the 'surviving' genomes. To do this, we pick a set of N random numbers, R_i, between 0 and 1 and the surviving genes are then the genes, i, that first satisfy $C_i > R_i$. This may lead to the same genome x_i being chosen multiple times or, due to the random nature of the selection, a completely unfit gene being selected. This is all part of the quasi-ergodic nature of the evolution.

Crossover

If selection were the only step in the algorithm then we would simply end by choosing the best genome resulting from the initial generation. Therefore we need to create new genomes that will ideally be as good or better solutions to the fitness function than the previous generation. The easiest method of doing so is to merge some of the selected genomes together. This process is known as the 'crossover' as we simply swap parts of the genome between two randomly selected genomes.

To do this, we first choose how many crossover genes we want every generation, typically given as a rate so that the total number of new genomes is $N_c = \rho_c N$. For the function given above, $\rho_c = 0.25$ is a reasonable value. Then we create a set of N_c randomly chosen integers R_i between 1 and N that will select which genomes will be the 'parents' of the new 'child' genomes.

The point at which the two parent genomes exchange genes is found by choosing a second random point, r_i, between the first two chromosomes and the last two chromosomes (i.e. 1 and length(x)-1) and creating a new chromosome from the first two chosen parent genomes. This is repeated with a new, randomly chosen, crossover point for the second and third parent genomes, and third and fourth parents, and so on until the last child genome is created from the first and last genomes.

In pseudo-code:

- for $i = 1 : N_c - 1$

  choose random cross over point, r_i

  new genome$_i$ = genome$_i(1 : r_i)$ +genome$_{i+1}(r_i + 1 :$length[genome])

154

- endfor

$$\text{new genome}_{N_c} = \text{genome}_1(1 : r_{N_c}) + \text{genome}_{N_c}(r_{N_c}+1 : \text{length[genome]})$$

where the '+' symbol signifies the creation of the new array and not the mathematical addition of the two segments of genomes. The N_c number of new genomes will then replace the parental genes in the new generation.

Mutation

Whilst crossover is useful in creating new genomes, no new chromosomes will be added by the process and so the evolution will be limited to a 'search space' of just the randomly chosen initial chromosomes. In order to cover all of our initial search space, and find a globally maximal solution, we must add in new chromosomes. This is done by a process analogous to biological mutation.

To do this, we first choose how many mutations we want in our system every generation, again typically given as a rate such that $N_m = \rho_m N \times \text{length}[x_i]$. For the example given above, $\rho_m = 0.1$ is reasonable. Secondly, we choose what value the mutation takes. This is typically done in a similar manner as the initialization. So, continuing the example given above, we will choose N_m random integers between 0 and 30 for our mutations.

Then we must choose their placement in the family of genomes. Therefore we select N_m integers between 1 and N as the number genome that will be mutated and for each mutation we choose a random integer between 1 and length$[x]$ for the chromosome in the genome that will be replaced by the mutation.

Termination

This process of evolution can be carried on indefinitely, although for any practical purpose it is useful to set a mechanism that stops the evolution should $f(x_i) = 0$ and the fitness value reach ∞. However, if this is not a realistic goal, or many solutions are required, then a maximum number of generations could be imposed.

Choosing Evolution Parameters

The nature of the evolution will be dictated by the complicated interaction of the fitness function, the rate of crossover, the rate of mutation, the number of

genomes and the search space used. The following is a list of general points on each value found by the author running many GA simulations:

The number of genomes, N, is not always particularly important as the total number of genomes evaluated will also be dictated by the number of generations that they are evolved for. However, if the search space is large and the rate of mutation and crossover relatively low then a large number of genomes is preferable as it is useful to consider many points in the search space each generation. Unless we do this, the selection step will limit the evolution to very confined areas that will take a long time to cover the entire search space.

The most efficient rates of crossover and mutation are complicated to define and often have to be altered *a posteriori*. As an example, if the evolution is getting stuck in particular areas of the search space then a larger mutation rate will aid in allowing the system to move around more freely and investigate a larger area of search space. However, if the rate of mutation is large then it is useful to have a relatively large crossover rate to aid in mixing the mutations between genomes and selecting out which mutations are most useful in each genome. A small crossover rate, combined with a large amount of mutation, will turn the GA into a random number generator that just evaluates a new set of random genomes each generation, which will not be efficient in finding maximal solutions.

A suitable search space can be chosen *a priori* by considering the likely values of successful solutions as discussed in the example above. Similarly, the GA used to find the excitation times required to create cat states used a search space limited by 0 and 1 times the complete excitation time for each mode. Therefore, in theory, each mode had a chance of being completely occupied or not all.

B.2 Coupling GA to Nelder-Mead Algorithm

It was found that the GA was very slow at finding 'good' solutions for the excitation times required to create cat states. This was because the interaction between the chromosomes in any reasonable genome were so strong that any mutation or crossover would greatly decrease the fitness of any ensuing genomes. This was further complicated by the fact that the mutation and crossover rates would ideally need to be large, as the GA would often get stuck on values of reasonably large fitness ($\lesssim 0.8$), that were unfortunately

still too small to be useful.

Therefore, an additional optimisation step was included before the selection step every generation. This was done so that mutations and crossovers would allow new genomes to be created that would be useful for the evolution and simultaneously avoid getting stuck on the same solution by having constantly evolving solutions that would have reasonable fitness values.

B.2.1   The Nelder-Mead Algoritm

The following is a simple explanation of the symplectic, heuristic algorithm used to maximise the fitness function for each genome before selection. The Nelder-Mead algorithm (NMA) is designed to minimise the function of interest, which we will take to be the function $f(x_i)$ described earlier, as opposed to the fitness function $1/|f(x_i)|$. As the details of this method aren't particularly useful in understanding the optimisation process only the flowchart will be given here. This flowchart is taken from [125]

The NMA works by choosing, evaluating, and evolving three points in search space. The three points are simply rated as the best point, B, the second to best or good point, G and the worst point, W, which means that $f(B) < f(G) < f(W)$. Then, using a series of trigonometry arguments, this 'triangle' (or rather simplex) of points is expanded and contracted and moved through search space by evaluating a series of neighbouring points given by:

$$\underline{M} = \frac{B + G}{2}, \tag{B.3}$$

$$\underline{R} = 2\underline{M} - \underline{W}, \tag{B.4}$$

$$\underline{E} = 2\underline{R} - \underline{M}, \tag{B.5}$$

$$\underline{C} = \frac{W + M}{2}, \tag{B.6}$$

$$\underline{S} = \frac{W + B}{2}, \tag{B.7}$$

where the list of parameters considered as genomes in the GA are now used as vectors.

The following list of logic steps is then carried out until two of the three points converge:

1. Evaluate and reassign the three points, B, G and W.

2. if $f(R) < f(G)$ then carry out Case 1, else carry out Case 2

   Case 1

   - if $f(B) < f(R)$
     replace W with R
   - else
     - if $f(E) < f(B)$
       replace W with E
     - else
       replace W with R
     - endif
   - endif

   end Case 1

   Case 2

   - if $f(B) < f(R)$
     replace W with R
   - endif
   - if $f(C) < f(W)$
     replace W with C
   - else
     replace W with S and G with M
   - endif

   end Case 2

3. Repeat until $f(B) = f(G)$

This technique is not simply used by itself instead of the GA as it is limited in its ability to find minima in very fluctuating search spaces and will thus often converge on some local minimum that is not guaranteed to be the global minimum that we require.

Appendix C

Integrating the Bose-Einstein Distribution

To obtain the line density of the thermal cloud, we must integrate over the momentum and extraneous spatial dimensions (y and z). To do this, we begin by simplifying the momentum integration using first cylindrical symmetry: $r^2 = y^2 + z^2$ followed by spherical symmetry $k^2 = k_x^2 + k_r^2$, then:

$$
\begin{aligned}
n_{th}(x,r) &= \frac{4\pi}{(2\pi)^3} \int_0^\infty \frac{k^2 dk}{e^{\frac{\epsilon - \mu}{k_B T}} - 1} \\
&= \frac{2}{\sqrt{\pi}} A_k \int_0^\infty \frac{X^{1/2} dX}{e^X / Z - 1} \\
&= A_k \sum_{l=1}^\infty \frac{Z^l}{l^{3/2}}, && \text{(C.1)}
\end{aligned}
$$

where:

$$
A_k = \left(\frac{m k_B T}{2\pi \hbar^2} \right)^{3/2} \tag{C.2}
$$

$$
X = \frac{\hbar^2 k^2}{2 m k_B T}, \tag{C.3}
$$

$$
Z = \exp\left[-\left(\frac{m}{2} \left(\omega_r^2 r^2 + \omega_x^2 x^2 \right) + 2 g n_o(x,r) - \mu \right) / k_B T \right], \tag{C.4}
$$

and the factor of $1/(2\pi)^3$ in (C.1) comes from using wavevectors instead of inverse wavelengths.

We can then obtain the line density by integrating through by the radius, r. However, this is complicated by the discontinuous nature of the condensate density:

$$n_{th}(|x| < x_{TF}) = 2\pi A_k \sum_{l=1}^{\infty} l^{-3/2} \left[\int_0^{r_{TF}(x)} r Z^l_{inside} dr + \int_{r_{TF}(x)}^{\infty} r Z^l_{outside} dr \right],$$

$$n_{th}(|x| > x_{TF}) = 2\pi A_k \sum_{l=1}^{\infty} l^{-3/2} \int_0^{\infty} r Z^l_{outside} dr, \tag{C.5}$$

where:

$$Z_{inside} = \exp\left[\left(\frac{m}{2} \left(\omega_r^2 r^2 + \omega_x^2 x^2 \right) - \mu \right) / k_B T \right], \tag{C.6}$$

$$Z_{outside} = \exp\left[- \left(\frac{m}{2} \left(\omega_r^2 r^2 + \omega_x^2 x^2 \right) - \mu \right) / k_B T \right]$$
$$= 1/Z_{outside}, \tag{C.7}$$

and:

$$r_{TF} = \sqrt{ \frac{2\mu}{m\omega_r^2} - \frac{\omega_x^2}{\omega_r^2} x^2 }. \tag{C.8}$$

Evaluating this integral, we obtain:

$$n_{th}(x) = A_n \begin{cases} \sum_{l=1}^{\infty} \left[2 - e^{\frac{l}{k_B T} \left(\frac{m\omega_x^2}{2} x^2 - \mu \right)} \right] l^{-5/2} & |x| < x_{TF} \\ \sum_{l=1}^{\infty} e^{\frac{l}{k_B T} \left(\mu - \frac{m\omega_x^2}{2} x^2 \right)} l^{-5/2} & |x| > x_{TF}, \end{cases}$$

where:

$$A_n = \frac{2\pi k_B T}{m\omega_y \omega_z} A_k. \tag{C.9}$$

C.0.2 Finding the Phase-Space Distribution of the Thermal Cloud

In order to find $n_{th}(x,k)$, we must first integrate over the radial momentum: $k_r^2 = k_y^2 + k_z^2$:

$$n_{th}(x,r,k) = \frac{1}{2\pi} \int_0^\infty \frac{k_r}{e^{\frac{\epsilon-\mu}{k_B T}} - 1} dk_r$$

$$= B_k \int_0^\infty \frac{dX}{e^X/Z - 1}$$

$$= B_k \sum_{l=1}^\infty \frac{Z^l}{l}, \tag{C.10}$$

where:

$$Z = \exp\left[-\left(\frac{m}{2}\left(\omega_r^2 r^2 + \omega_x^2 x^2\right) + \frac{\hbar^2 k^2}{2m} + 2gn_o(x,r) - \mu\right)/k_B T\right] \tag{C.11}$$

and

$$B_k = \frac{k_B T}{\hbar^2}. \tag{C.12}$$

Again we have included a factor of $1/(2\pi)^2$, as we're essentially integrating over 2 wavevector dimensions, not two inverse-space dimensions.

The integration over the radial dimension is almost identical to that done above, except with a different prefactor and an additional exponential term, resulting in:

$$n_{th}(x,k) = B_n \begin{cases} \sum_{l=1}^\infty e^{\frac{-l\hbar^2 k^2}{2mk_B T}} \left[2 - e^{\frac{l}{k_B T}\left(\frac{m\omega_x^2}{2}x^2 - \mu\right)}\right] l^{-2} & |x| < x_{TF} \\ \sum_{l=1}^\infty e^{\frac{l}{k_B T}\left(\mu - \frac{m\omega_x^2}{2}x^2 - \frac{\hbar^2 k^2}{2mk_B T}\right)} l^{-2} & |x| > x_{TF}, \end{cases}$$

where:

$$B_n = \frac{1}{\omega_y \omega_z} \left(\frac{k_B T}{2\pi\hbar}\right)^2. \tag{C.13}$$

Bibliography

[1] E. Fermi, Sulla quantizzazione del gas perfetto monoatomico. *Rend. Lincei*, **3**, 145, (1926).

[2] P. A. M. Dirac, On the theory of quantum mechanics. *Proceed- ings of the Royal Society of London. Series A*, **112**, 661, (1926).

[3] W. Pauli, *Exclusion principle and quantum mechanics*, Éds. du Griffon, (1947).

[4] C. J. Pethick and H. Smith, *Bose-Einstein Condensation in Dilute Gases*, Cambridge University Press, (2008).

[5] A. Einstein, *Quantentheorie des einatomigen idealen Gases II*, Sitz. Preess. Akad. Wiss., **1**, 3, (1925).

[6] M. H. Anderson, et al., Science, 269, **198**, (1995).

[7] K. B. Davis, et al., Phys. Rev. Lett., **22**, 75, (1995).

[8] W. H. Wing, Progress in Quantum Electronics, 8, **3**, (1984).

[9] J. Reichel, Applied Physics B: Lasers and Optics, 74, **6**, (2002).

[10] T. Weber, *Bose-Einstein Condensation of Optically Trapped Cesium*, PhD Thesis, Leopold- Franzens- University of Innsbruck, (2003).

[11] J.G. Lee & W.T. Hill III, Rev. Sci. Instrum., **85**, 103106, (2014).

[12] A. Einstein, Physikalis-che Zeitschrift, 121, **18**, (1917).

[13] T. W. H́ansch and A. L. Schawlow, Optics Communications, 68, **13**, (1975).

[14] M.C. Garrett, *Formation Dynamics and Phase Coherence of Bose-Einstein Condensates*, PhD thesis, University of Queensland, (2012).

[15] A. Bezett & P.B. Blakie, Phys. Rev. A, **79**, 23602, (2009).

[16] P.B. Blakie et al., Advances in Physics, **57**, 363, (2008).

[17] A. Polkovnikov, Phys. Rev. A **68**, 053604 (2003).

[18] A. Polkovnikov and V. Gritsev, Nature Physics **4**, 477 (2008).

[19] J. Denschlag, et al., Science **287**, 97, (2000).

[20] T.P. Simula et al., Phys. Rev. Lett., **94**, 80404, (2005).

[21] E. A. Burt et al., Phys. Rev. Lett. **79**, 337 (1997).

[22] R.G. Scott et al., Phys. Rev. Lett. **90**, 110404, (2003).

[23] S.P. Cockburn & N.P. Proukakis, Phys. Rev. A, **86**, 33610, (2012).

[24] S.J. Rooney, A.S. Bradley & P.B. Blakie, Phys. Rev. A, **81**, 23630, (2010).

[25] S. Schmid, G. Thalhammer, K. Winkler, F. Lang, and J.H. Denschlag, New J. Phys. **8**, 159 (2006).

[26] A. Browaeys, H. Haffner, C. McKenzie, S.L. Rolston, K. Helmerson, and W.D. Phillips, Phys. Rev. A **72**, 053605 (2005).

[27] E. Arahata and T. Nikuni, Phys. Rev. A **79**, 063606 (2009).

[28] J. Mun, P. Medley, G.K. Campbell, L.G. Marcassa, D.E. Pritchard, and W. Ketterle, Phys. Rev. Lett. **99**, 150604 (2007).

[29] M. Ben Dahan, E. Peik, J. Reichel, Y. Castin, and C. Salomon, Phys. Rev. Lett. 76, 4508 (1996).

[30] O. Morsch, J.H. M'uller, M. Cristiani, D. Ciampini and E. Arimondo, Phys. Rev. Lett. **87**, 140402 (2001).

[31] M. Salerno, V.V. Konotop, and Y.V. Bludov, Phys. Rev. Lett. **101**, 030405 (2008).

[32] M. Gustavsson, E. Haller, M.J. Mark, J.G. Danzl, G. Rojas-Kopeinig, H.-C. N´agerl, Phys. Rev. Lett. **100**, 080404 (2008).

[33] T. Salger, G. Ritt, C. Geckeler, S. Kling, and M. Weitz, Phys. Rev. A **79**, 011605 (2009).

[34] F. Nogrette, H. Labuhn, S. Ravets, D. Barredo, L. Béguin, A. Vernier, T. Lahaye, and A. Browaeys Phys. Rev. X **4**, 021034 (2014).

[35] Jan Willem Abraham et al. New J. Phys. **16** 013001 (2014).

[36] M. T. Greenaway, A. G. Balanov, and T. M. Fromhold, Phys. Rev. A **87**, 013411 (2013).

[37] L. Fallani et al.,Phys. Rev. Lett. **93**, 140406 (2004).

[38] R. Chacón, D. Bote, and R. Carretero-González, Phys. Rev. E **78**, 036215 (2008).

[39] V. Lebedev and F. Renzoni, Phys. Rev. A **80**, 023422 (2009).

[40] D. Cubero and F. Renzoni, Phys. Rev. E **86**, 056201 (2012).

[41] S. Denisov et al., Phys. Rev. Lett. **100**, 224102 (2008).

[42] A. O. Selskii et al., Phys. Rev. B **84**, 235311 (2011).

[43] C.F.F. Karney & A. Bers, Phys. Rev. Lett. **39**, 550 (1977).

[44] P. A. Knott, W. J. Munro, and J. A. Dunningham, Phys. Rev. A **89**, 053812 (2014).

[45] D. Leibfried et al., Nature **438**, 7068, 639 (2005)

[46] H.W. Lau et al., Phys. Rev. Lett. **113**, 090401 (2014).

[47] G. M. Zaslavsky et al., *Weak Chaos and Quasi-Regular Patterns*, Cambridge University Press, 1991.

[48] D. P. A. Hardwick, PhD thesis, University of Nottingham (2007).

[49] G. M. Zaslavsky, *Chaos in Dynamic Systems*, Harwood Academic Publishers (1987).

[50] G. M. Zaslavsky, *Physics of Chaos in Hamiltonian Systems*, Imperial College Press (1998).

[51] J. B. Marion & S. T. Thornton, *Classical Dynamics of Particles and Systems*, Saunders College Publishing (1995).

[52] H. G. Schuster & W Just, *Deterministic Chaos: An Introduction*, Wiley-VCH, 4th edition (2005).

[53] E. Wigner, Phys. Rev. **40**, 749 (1932).

[54] B. Liebchen et al., EPL **94**, 40001 (2011).

[55] I. Brouzos & P. Schmelcher, Phys. Rev. A **85** 033635 (2012).

[56] T. M. Fromhold et al., J. Opt. B: Quantum Semiclass. Opt. **2**, 628 (2000).

[57] S. M. Soskin, Contemp. Phys. **51**, 233 (2010).

[58] A. Amann, J. Schlesner, A. Wacker, and E. Schöll, Phys. Rev. B **65**, 193313 (2002).

[59] Hur et al., Phys. Rev. A, **72**, 013403 (2005).

[60] R. Bücker et al., J. Phys. B: At. Mol. Opt. Phys., **46**, 104012 (2013).

[61] I. S. Gradshteyn and I. M. Ryzhik, *Table of Integrals, Series and Products, 7th Ed.*, Associated Press (2007).

[62] D. J. Griffiths, *Introduction to Quantum Mechanics, 2nd Ed.*, Prentice Hall (2004).

[63] W. Mandel, *Optical coherence and quantum optics*, Cambridge University Press (1995).

[64] C. C. Gerry, J. Mimih, Contemp. Phys. **51**, 497 (2010).

[65] Q.S. Tan et al., Phys. Rev. A, **89**, 053822 (2014).

[66] V.V. Dodonov, I.A. Malkin, V.I. Man'ko, Physica, **72**, 597 (1974).

[67] B. Vlastakis et al., Science **342**, 607 (2013).

[68] M. Tsubotaa, M. Kobayashib & H. Takeuchic, Physics Reports, **522**, 191 (2013)

[69] M. Brachet, Comptes Rendus Physique, **13**, 954 (2012)

[70] D. Hunger, et al., Comptes Rendus Physique, **12**, 871 (2011)

[71] M.K. Ivory, et al., Rev. Sci. Inst., **85**, 043102 (2014)

[72] D. Hunger, et al., Phys. Rev. Lett., **104**, 143002 (2010)

[73] M. de Angelis, et al., Procedia Computer Science **7**, 334 (2011)

[74] Y.J Lin, et al., Phys. Rev. Lett., **92**, 050404 (2004)

[75] S. Dutta and E. J. Mueller, Phys. Rev. A **91**, 013601 (2015).

[76] S. Y. Buhmann et al., The Euro. Phys. Jour. D, **35**, 15 (2012).

[77] G. Bimonte, G. L. Klimchitskaya, and V. M. Mostepanenko, Phys. Rev. A **79**, 042906 (2009).

[78] K. A. Milton, P. Parashar, N. Pourtolami, and Iver Brevik, Phys. Rev. D **85**, 025008 (2012).

[79] V.A. Parsegian, *Van der Waals Forces: A Handbook for Biologists, Chemists, Engineers, and Physicists*, Cambridge (2006)

[80] H.B.G. Casimir & D. Polder, Phys. Rev., **73**, 360 (1948)

[81] A.M.C.Reyes & C. Eberlein, Phys. Rev. A, **80**, 032901 (2009)

[82] Widely commercially available - e.g. TEMwindows, NY, USA.

[83] T.E. Judd, et al., New J. Phys., **13**, 083020 (2011).

[84] A.J. Moerdijk, H.M.J.M. Boesten, and B.J. Verhaar, Phys. Rev. A, **53**, 916 (1996).

[85] J. Söding, et al., Appl. Phys. B, **69**, 257 (1999).

[86] P. Kruger, *Coherent Matter Waves Near Surfaces*, PhD Thesis, University of Heidelberg, Germany (2004).

[87] Nuclear Physics, B.B. Srivastava (2006)

[88] Y.E. Kim & A.L. Zubarev, Int. Jour. Theor. Phys., **33**, 9 (1994).

[89] D.F. Wang, Micro & Nano Lett., **7**, 713 (2012).

[90] A. Dario, Nature Comms., **3**, 806 (2012).

[91] K. Borkje, Phys. Rev. Lett., **107**, 123601 (2011).

[92] J.M. Obrecht, R.J. Wild, and E.A. Cornell, Phys. Rev. A, **75**, 062903 (2007).

[93] B. Jetter, et al., New J. Phys., **15**, 073009 (2013).

[94] J.D. Teufel, et al., Nature, **475**, 359 (2011).

[95] Y. Han, et al., Int. Jour. Quant. Inf., **12**, 1450005, (2014).

[96] C. Genes, et al., Phys. Rev. A, **80**, 061803, (2009).

[97] P.W. Atkins, *Physical Chemistry, 5th Ed.*, W.H. Freeman and Company, (1994).

[98] J.M. Gere & S.P. Timoshenko, *Mechanics of Materials, 4th Ed.*, PWS Publishing Company, (1997).

[99] E. Voltera & E.C. Zachmanoglou, *Dynamics of Vibrations*, Charles E. Merrill Books, (1965).

[100] T.R. Albrecht, et al., J. Appl. Phys., **69**, 2 (1991).

[101] T.P. Meyrath, et al., Optics Express, **13**, 2843 (2005).

[102] S. Huang, H. Tao, I. Lin & X. Zhang, Sensors and Actuators A, **145**, 231 (2008).

[103] H. Colder, et al., Jour. Appl. Phys., **5**, 115 (2014).

[104] Auxiliary Material of [70].

[105] R. Tabrizian, et al., IEEE Trans. Elect. Devs., **60**, 2656 (2013).

[106] C.H. Lin, et al., Advanced Materials, **24**, 2722 (2012).

[107] J. Bak, et al., Nature Materials, **7**, 459 (2008).

[108] N.P. Proukakis & B. Jackson, J. Phys. B: At. Mol. Opt. Phys., **41**, 203002, (2008).

[109] C. Pethick & H. Smith, *Bose-Einstein Condensation in Dilute Gases*, Cambridge University Press, (2002).

[110] I.G. Hughes & T.P.A. Hase, *Measurements and their Uncertainties*, Oxford, (2010).

[111] M. Naraschewski & D.M. Stamper-Kurn, Phys. Rev. A, **58**, 2423, (1998).

[112] B. Yuen, *Production and Oscillations of a Bose Einstein Condensate on an Atom Chip*, PhD Thesis, Imperial College London, (2014).

[113] D.Montgomery & D. Gorman, Phys. Rev. **124**, 1309 (1961).

[114] F. Gerbier et al., Phys. Rev. A, **70**, 013607, (2004).

[115] S. Kouidri & M Benarous, J. Phys. B: At. Mol. Opt. Phys., **44**, 205301, (2011).

[116] R. Sewell, *Matter Wave Interference on an Atom Chip*, PhD thesis, Imperial College London, (2009).

[117] L.P. Pitaevskii & S. Stringari, Physics Letters A, **235**, 398, (1997).

[118] P Szepfalusy & I Kondor, Annals of Physics, **82**, 1, (1974).

[119] P.C Hohenberg & P.C Martin, Annals of Physics, **34**, 291, (1965).

[120] M. Abramowitz & I.A. Stegun, *Handbook of Mathematical Functions, 10th printing with corrections*, Dover, (1972).

[121] H.J.W. Zandvliet, Surface Science, **577**, 93, (2003).

[122] L. Gragnaniello et al., Surface Science, **611**, 86, (2013).

[123] D. Hermawanto, arXiv:1308.4675

[124] M. Gen & R. Cheng, *Genetic Algorithms And Engineering Design*, John Wiley & Sons, (1997).

[125] J.H. Mathews & K.K. Fink, *Numerical Methods Using Matlab, 4th Ed.*, Prentice-Hall Inc., (2004).

[126] A. del Campo et al., Phys. Rev. Lett., **110**, 050403 (2013).

[127] G. De Chiara et al., Phys. Rev. A, **77**, 052333 (2008).

[128] F. Platzer et al., Phys. Rev. Lett., **105**, 020501 (2010).

[129] T. Caneva et al., New J. Phys., **14**, 093041 (2012).

[130] A. Rahmani et al., Phys. Rev. A, **87**, 043607 (2013).

[131] A. Assion et al., Science **282**, 919 (1998).